

Advances in Civil Engineering

Advanced Cementitious Building Materials with Applications in Civil Engineering

Lead Guest Editor: Peng Zhang

Guest Editors: Song Han, Serina Ng, and Xuhao Wang





**Advanced Cementitious Building Materials
with Applications in Civil Engineering**

Advances in Civil Engineering

**Advanced Cementitious Building Materials
with Applications in Civil Engineering**

Lead Guest Editor: Peng Zhang

Guest Editors: Song Han, Serina Ng, and Xuhao Wang



Copyright © 2017 Hindawi. All rights reserved.

This is a special issue published in “Advances in Civil Engineering.” All articles are open access articles distributed under the Creative Commons Attribution License, which permits unrestricted use, distribution, and reproduction in any medium, provided the original work is properly cited.

Editorial Board

M. Cruz Alonso, Spain
Serji N. Amirkhanian, USA
P. Ch. Anastasopoulos, USA
Pedro Arias-Sánchez, Spain
Rafik Belarbi, France
Andrea Benedetto, Italy
Alberto Campisano, Italy
Francesco Canestrari, Italy
D. C. Castro-Fresno, Spain
Noel Challamel, France
Ghassan Chehab, Lebanon
F. Colangelo, Italy
Ottavia Corbi, Italy
Gianmarco de Felice, Italy
Luigi Di Sarno, Italy

Slobodan Djordjevic, UK
Ahmed Elghazouli, UK
Giovanni Garcea, Italy
Kirk Hatfield, USA
John Mander, USA
G. Carlo Marano, Italy
Hossein Moayedi, Iran
Fabrizio Mollaioli, Italy
Ayman S. Mosallam, USA
Giuseppe Oliveto, Italy
Alejandro Orfila, Spain
T. Ozbakkaloglu, Australia
Alessandro Palmeri, UK
Ram M. Pendyala, USA
Arnaud Perrot, France

C. Petit, France
Sertong Quek, Singapore
Dimitris Rizos, USA
Hamid Ronagh, Australia
Pier Paolo Rossi, Italy
Anna Saetta, Italy
Halil Sezen, USA
Alexandru Sheremet, USA
S. Kumar Shukla, Australia
Claudio Tamagnini, Italy
Yaya Tan, China
C. Vipulanandan, USA
Wei-Chau Xie, Canada

Contents

Advanced Cementitious Building Materials with Applications in Civil Engineering

Peng Zhang, Song Han, Serina Ng, and Xu-Hao Wang

Volume 2017, Article ID 9654910, 3 pages

Experimental Research and Finite Element Analysis on Mechanical Property of SFRC T-Beam

Min Sun, Jiapeng Zhu, Ning Li, and C. C. Fu

Volume 2017, Article ID 2721356, 8 pages

Numerical Simulations of Restrained Shrinkage Cracking in Glass Fibre Reinforced Shotcrete Slabs

Andreas Sjölander and Anders Ansell

Volume 2017, Article ID 8987626, 11 pages

Influence of Crumb-Rubber in the Mechanical Response of Modified Portland Cement Concrete

J. Retama and A. G. Ayala

Volume 2017, Article ID 3040818, 9 pages

Bond Effects between Concrete and Steel Bar Using Different Diameter Bars and Different Initial Crack Width

Papa Niane Faye, Yinghua Ye, and Bo Diao

Volume 2017, Article ID 8205081, 11 pages

Experimental Studies on Punching Shear and Impact Resistance of Steel Fibre Reinforced Slag Based Geopolymer Concrete

Srinivasan Karunanithi

Volume 2017, Article ID 9210968, 9 pages

Effect of Modified Rubber Particles Mixing Amount on Properties of Cement Mortar

Gang Xue and Mei-ling Cao

Volume 2017, Article ID 8643839, 6 pages

Editorial

Advanced Cementitious Building Materials with Applications in Civil Engineering

Peng Zhang,¹ Song Han,² Serina Ng,³ and Xu-Hao Wang⁴

¹*School of Water Conservancy and Environment Engineering, Zhengzhou University, Zhengzhou 450001, China*

²*School of Civil Engineering, Beijing Jiaotong University, Beijing 100044, China*

³*Department of Materials and Structures, SINTEF Building and Infrastructure, 7465 Trondheim, Norway*

⁴*National Concrete Pavement Technology Center, Iowa State University, Ames, IA 50011, USA*

Correspondence should be addressed to Peng Zhang; zhangpeng@zzu.edu.cn

Received 13 June 2017; Accepted 13 June 2017; Published 11 July 2017

Copyright © 2017 Peng Zhang et al. This is an open access article distributed under the Creative Commons Attribution License, which permits unrestricted use, distribution, and reproduction in any medium, provided the original work is properly cited.

Cementitious building material is most extensively used as a kind of architectural materials in latter day and is the largest artificial material at present. With the high development of construction industry, many building structures with long span, high strength, and great height are being constructed or used under harsh conditions, which has higher requirements on cementitious building materials. Advanced cementitious building materials can be defined as the cementitious building materials that can meet special combinations of properties and uniformity requirements, which cannot always be achieved routinely using traditional raw materials and conventional mixing, placing, and curing methods. The factors which justify the popularity of advanced cementitious building materials are high strength, high workability, and high durability for various structural purposes [1]. Compressive strength of the cementitious material which is usually applied to evaluate the quality of cementitious material and its applicability for purpose is a major component in rational structure design. Today, the durability is also a major aspect to be considered in civil engineering structure design as the importance of durability of cementitious materials is being more and more accepted and emphasized [2]. A large number of investigators are devoting themselves to developments of advanced cementitious building materials and also studying on the mechanism research for peculiar performance, manufacturing technique, experiment methods, modeling, and applications of various advanced cementitious building materials. Generally, there are a lot of approaches to obtain advanced cementitious materials. In general, specific binding materials, aggregates, and additives can be incorporated into

the conventional cementitious materials to obtain advanced cementitious materials. For example, some extraordinary aggregates [3], chemical additives [4], various fibers [5, 6], and mineral admixtures [7, 8] can be added to fabricate advanced cementitious building materials.

Cementitious building materials have significant new progresses in recent years. The advanced cementitious building materials will provide better materials for specific projects in civil engineering. This special issue aims to bring investigators from industry and academia together to report and explore the new investigations techniques, new preparation methods and basic material properties, testing methods, and standardization in civil engineering, fresh properties and constructability, shrinkage and creep, structural performance and modeling, functional coatings for buildings, durability and sustainability, and field applications in advanced cementitious building materials and review the latest progress in this field. The advanced cementitious building materials include common cementitious composites building materials, cementitious pavement materials, high-performance concrete and ultrahigh-performance concrete, high-ductility and fibre-reinforced materials, and self-sensing/self-healing concrete. Out of about twenty-five submitted manuscripts, six research manuscripts have been selected and published in this special issue because of their good quality and relevance to the theme of this special issue. The selected articles address various aspects, including bond performance between the concrete matrix with different initial crack width and the steel bars with different diameters, mechanical properties of different contents of rubber particles modified cement mortar,

and experiments and finite element analysis of mechanical properties of steel fiber-reinforced concrete T-beams, punching shear and impact resistance of steel fiber-reinforced slag-based geopolymer concrete, mechanical response of modified Portland cement concrete containing crumb-rubber, and numerical simulations of restrained shrinkage cracking in glass fiber-reinforced shotcrete slabs.

The paper titled “Bond Effects between Concrete and Steel Bar Using Different Diameter Bars and Different Initial Crack Width” is authored by P.N. Faye et al. They conducted the standard pull-out test and distribution of chloride ion test for the bond specimens and measured the bond strength to evaluate the combined effect of different diameter bars embedded in cracked concrete and different initial crack width on the bond properties between concrete and steel bars. In the study, they artificially made four widths of initial crack of 0, 80, 150, and 210 microns by inserting slice into bond specimens during the casting of concrete. Besides, they adopted three bar diameters of 10 mm, 14 mm, and 18 mm. After being cured for 28 days, the bond specimens were exposed to the environment of wet-dry cycles of seawater and atmosphere for another 90 days. Their results indicate that the cracks with width less than 80 microns for the specimens with 10 mm diameter embedded bar rapidly disappeared during the course of wet-dry cycles, and the crack width below 150 microns decreased slightly. However, the crack width over 200 microns will increase gradually. The chloride content of the specimens increased with the increase of initial crack width or the diameter of the embedded bar. Furthermore, the chloride content decreased with the increase of concrete depth.

G. Xue and M. Cao conducted a study on the influence of modified rubber particles mixing content on properties of cement mortar. They prepared the cement mortar containing crumb-rubber using the crumb-rubber aggregates in 60 mesh, which have been modified by 1% polyvinyl alcohol solution. The properties of the cement mortar include compressive strength, impact resistance, flexural strength, the ratio of compressive strength to flexural strength, and dry contraction percentage. In their study, five rubber dosages of 7.5%, 15%, 19%, 22.5%, and 30% were selected. The optimal content of crumb-rubber was determined by three measured parameters: dry contraction percentage, impact resistance, and the ratio of compressive strength to flexural strength. Their results showed that the ratio of compressive strength to flexural strength has the minimum value when the content of modified rubber particles is 19%. At the same time, the modified mortar exhibits high rational drying shrinkage and high impact resistance with the rubber content of 19%. Therefore, the authors considered 19% as the optimal used amount of the modified rubber particles in their study.

The paper titled “Experimental Research and Finite Element Analysis on Mechanical Property of SFRC T-Beam” is authored by M. Sun et al. Through a series of experiments of one common concrete T-beam and two steel fiber-reinforced concrete T-beams using two-point loading method, they investigate the effect of different steel fiber volume contents on the ultimate shear capacity, integral rigidity, and the crack distribution characteristics, and the relevant influencing

mechanism was analyzed. They also simulated the experiment results obtained using ANSYS software and found that the simulation results of ANSYS were well accordant with the test results. Both of the results of experiments and ANSYS software simulation indicated that the addition of steel fibers greatly increased the ultimate shear capacity and integral rigidity of the concrete, and the propagation of cracks can be partially reduced effectively by the addition of steel fibers. The results also indicate that ANSYS software can be applied to accurately simulate the mechanical properties of steel fiber-reinforced T-beam.

S. Karunanithi in the paper titled “Experimental Studies on Punching Shear and Impact Resistance of Steel Fibre Reinforced Slag Based Geopolymer Concrete” carried out a series of punching shear tests and impact tests to evaluate the punching shear and impact resistance of steel fiber-reinforced slag-based geopolymer concrete. The related response of the slag-based geopolymer concrete under shear load and sudden impact load was determined. Besides, the author took the scanning electron microscope (SEM) images for the slag-based geopolymer samples with alkali activators and accelerators and carried out the Energy-Dispersive X-ray Spectroscopy (EDX) analysis on the hardened samples of slag-based geopolymer paste. The various dosages of steel fiber added to the slag-based geopolymer concrete in that study include 0.5%, 1.0%, and 1.5%. From the results, it can be found that the slag-based geopolymer concrete with the binder to aggregate ratio of 0.22 and fine to coarse aggregate ratio of 0.6, reinforced by 1.0% volume dosage of steel fibers, exhibited higher punching shear force, better energy absorption, and higher first crack toughness and ultimate failure toughness. Within the scope of the fiber dosages in this study, 1% of steel fiber is the optimal volume content for the slag-based geopolymer concrete to obtain better punching shear and impact resistance.

The paper titled “Influence of Crumb-Rubber in the Mechanical Response of Modified Portland Cement Concrete” is authored by J. Retama and A.G. Ayala. They conducted a series of experiments to study the influence of crumb-rubber on the mechanical properties of Portland cement concrete. In their study, three different contents of crumb-rubber and the Disk-Shaped Compact Tension specimen geometry, normed by the D7313-13 of the ASTM, were used to prepare the concrete. Based on the hypothesis that the stone aggregate replaced with crumb-rubber in the concrete mixture can modify the energy dissipation during the course of cracking process and can affect the concrete properties under monotonically increasing loads, they also carried out the numerical simulations to simulate the damage evolution of the concrete, applying the numerical model of Embedded Discontinuity Method (EDM). Their experiment results indicated that the rubber fineness used in their study has great influence on the fracture energy and other properties of concrete. The numerical simulation results showed that good approximation of the experimental curve in the elastic and softening branches can be provided by using the numerical methods in their study.

A. Sjölander and A. Ansell in the paper titled “Numerical Simulations of Restrained Shrinkage Cracking in Glass Fibre

Reinforced Shotcrete Slabs” demonstrated a method for non-linear numerical simulations to study the differences in stress build-up and cracking behavior of restrained shotcrete slabs subjected to shrinkage. Through the numerical simulation, they obtained the influence of the irregular shape and varying thickness on the cracking properties of the shotcrete. By varying the fracture energy in bending and in the interaction between shotcrete and the substrate, the influences of glass fiber reinforcement and bond were obtained in their study. Their results indicated that an end-restrained shotcrete slab was prone to shrinkage-induced cracking, and it is important for the continuous bond to avoid wide shrinkage cracks when shotcrete is sprayed directly onto the rock.

Acknowledgments

We would like to thank the authors who have submitted manuscripts to this special issue. We would also like to acknowledge the referees who have put in the hard work and their valuable time to review each paper in a timely and professional way. The lead editor thanks all the editors for their contribution in reviewing and assigning reviews for the submitted manuscripts.

Peng Zhang
Song Han
Serina Ng
Xu-Hao Wang

References

- [1] B. J. Olawuyi and W. P. Boshoff, “Influence of SAP content and curing age on air void distribution of high performance concrete using 3D volume analysis,” *Construction and Building Materials*, vol. 135, pp. 580–589, 2017.
- [2] H.-S. Shi, B.-W. Xu, and X.-C. Zhou, “Influence of mineral admixtures on compressive strength, gas permeability and carbonation of high performance concrete,” *Construction and Building Materials*, vol. 23, no. 5, pp. 1980–1985, 2009.
- [3] A. Remadnia, R. M. Dheilily, B. Laidoudi, and M. Quéneudec, “Use of animal proteins as foaming agent in cementitious concrete composites manufactured with recycled PET aggregates,” *Construction and Building Materials*, vol. 23, no. 10, pp. 3118–3123, 2009.
- [4] J. Y. Wang, N. Banthia, and M. H. Zhang, “Effect of shrinkage reducing admixture on flexural behaviors of fiber reinforced cementitious composites,” *Cement and Concrete Composites*, vol. 34, no. 4, pp. 443–450, 2012.
- [5] P. Zhang and Q.-F. Li, “Effect of polypropylene fiber on durability of concrete composite containing fly ash and silica fume,” *Composites Part B: Engineering*, vol. 45, no. 1, pp. 1587–1594, 2013.
- [6] P. Zhang, Y.-N. Zhao, C.-H. Liu, P. Wang, and T.-H. Zhang, “Combined effect of nano-SiO₂ particles and steel fibers on flexural properties of concrete composite containing fly ash,” *Science and Engineering of Composite Materials*, vol. 21, no. 4, pp. 597–605, 2014.
- [7] P. Zhang and Q.-F. Li, “Effect of silica fume on durability of concrete composites containing fly ash,” *Science and Engineering of Composite Materials*, vol. 20, no. 1, pp. 57–65, 2013.
- [8] P. Zhang, X.-B. Dai, J. X. Gao, and P. Wang, “Effect of nano-SiO₂ particles on fracture properties of concrete composite containing fly ash,” *CurrentScience*, vol. 108, no. 11, pp. 2035–2043, 2015.

Research Article

Experimental Research and Finite Element Analysis on Mechanical Property of SFRC T-Beam

Min Sun,¹ Jiapeng Zhu,¹ Ning Li,¹ and C. C. Fu²

¹Department of Civil Engineering, Suzhou University of Science and Technology, Suzhou, Jiangsu 215011, China

²University of Maryland at College Park, College Park, MD 20742, USA

Correspondence should be addressed to Min Sun; sunmin@mail.usts.edu.cn

Received 23 January 2017; Accepted 14 March 2017; Published 4 May 2017

Academic Editor: Peng Zhang

Copyright © 2017 Min Sun et al. This is an open access article distributed under the Creative Commons Attribution License, which permits unrestricted use, distribution, and reproduction in any medium, provided the original work is properly cited.

Research on mechanical property of SFRC was done through experiments of two SFRC T-beams and one concrete T-beam, while the influences of different volume fractions of steel fibers on integral rigidity, ultimate shear capacity, and the crack distribution characteristics were analyzed. ANSYS finite element software was used to simulate the tests and it was found that there was good conformation between the results of ANSYS simulation and tests. The test results and finite element software simulation both showed that the incorporation of steel fibers in the concrete can increase the integral rigidity and ultimate shear capacity, while partially reducing the propagation of cracks effectively. It was also proved that it is reliable to simulate SFRC T-beam by ANSYS software.

1. Introduction

T-beam is very commonly used in the Chinese highway bridges, where the crackle status is very serious in T-beams. With the wide usage of the traditional concrete, some obvious shortcomings are exposed gradually, such as low strength, poor ductility, and the brittle failure under the impact load. These shortcomings will limit the application of concrete in the future structure. If some steel fibers are added in concrete, fiber can not only prevent the development of concrete cracks but also improve the flexural, shear, and tensile properties of concrete [1–4]. At the same time, steel fibers can improve the antifatigue, anti-impact, durability, and crack toughness of concrete [5, 6] and make concrete sustain certain plastic properties.

Steel fiber reinforced concrete (SFRC) has a good crack resistance, so it is widely used in the fields of airport pavement, bridge deck, and waterproof roof. But now there are not a lot of researches on the shear performance and crack resistance effect of SFRC T-beam. In this paper, a concrete T-beam and two SFRC T-beam specimens were designed to investigate the effect of steel fiber content on the bearing capacity of concrete T-beam to understand the characteristics of SFRC in shear and crack resistance.

2. Preparation of Test

2.1. Description of Specimens. In this test, three test T-beams were prepared, one three-meter (length) ordinary concrete T-beam and two three-meter (length) SFRC T-beams. The parameters of specimen are shown in Table 1. HRB335 steel bar was used as the tension longitudinal reinforcement, while HPB235 steel bar was used as the compression longitudinal reinforcement, the flange plate main bars, and the stirrups. The section size and reinforcement layout are shown in Figure 1.

2.2. Materials Properties. In this experiment, a tape of waved steel fibers produced by Suzhou Longyu Co., Ltd., with 792 MPa tensile strength, 30.18 mm fiber length, 0.91 mm equivalent diameter, and 33-aspect ratio, was used. The mechanical properties of concrete and the reinforced bar are shown in Tables 2 and 3.

2.3. Test Method. In the test, the method of two-point loading was used by the distributive beam. The shear span ratio was 2. The support of the beam was 225 mm far from the beam end, and the loading device was a separate type of hydraulic

TABLE 1: Test T-beam parameters.

Material	Beam node	Stirrup spacing (mm)	Stirrup ratio	Volume fraction of steel fiber
Concrete	1	150	0.48%	0
SFRC	2	150	0.48%	$\rho = 1.5\%$
SFRC	3	150	0.48%	$\rho = 2.0\%$

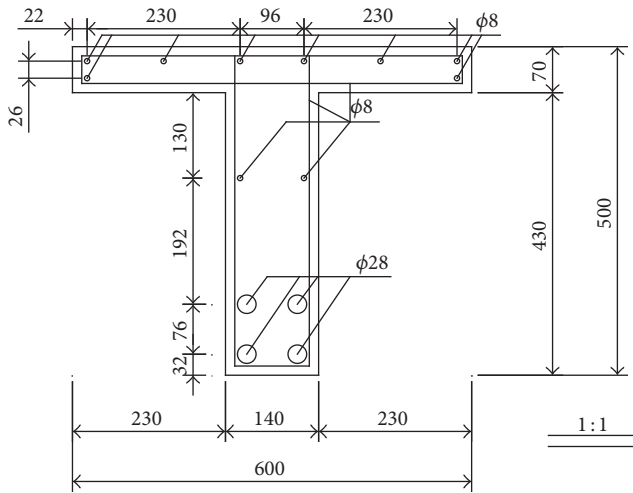


FIGURE 1: Section size and reinforcement layout (unit: mm).

TABLE 2: Mechanical properties of concrete.

Beam node	Crushing compressive strength	Concrete compressive strength	Young's modulus
1	37.1	28.2	31.9
2	40.3	30.6	32.7
3	40.5	30.8	32.7

TABLE 3: Mechanical properties of reinforced bar.

Steel grade	Bar diameter	Yield stress	Ultimate stress	Young's modulus
HPB235	8	342	500	210
HRB235	28	389	574	200

Note. In Tables 2 and 3, length unit is mm, the strength unit is Mpa, and Young's modulus unit is Gpa.

jack that used a high-precision static servo-hydraulic-control system. Gradation loading was acted on the beam, and the holding time was 15 minutes. In the process of loading, the crack occurrence and development should be carefully observed.

TABLE 4: Summary of shear resistance of beams.

Beam node	V_{cr} (KN)	V_u (KN)	U_{max} (mm)
1	200	830	10.77
2	400	1150	18.9
3	300	>1200	7.6

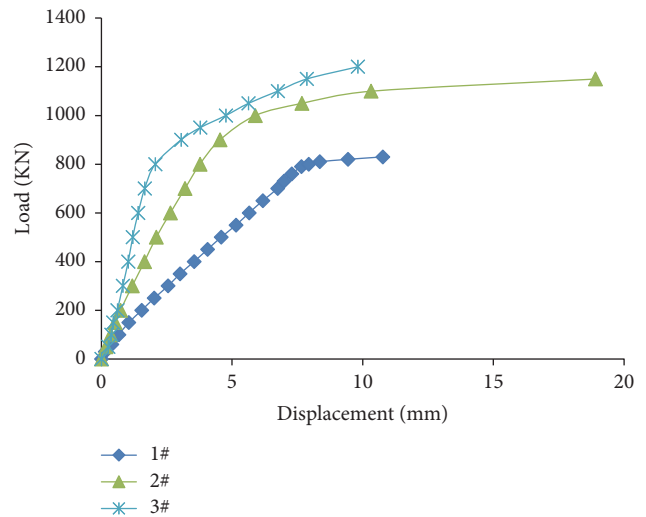


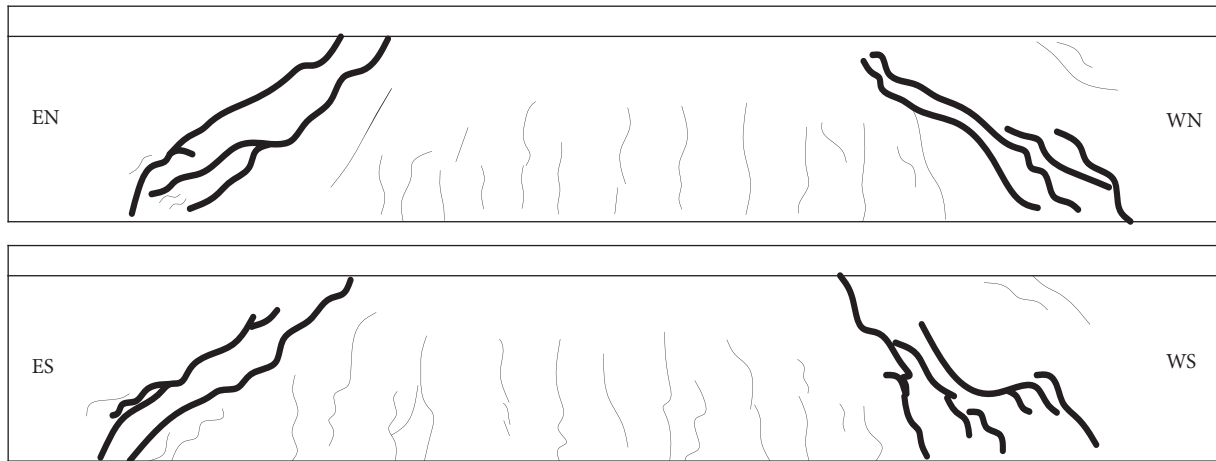
FIGURE 2: Load-displacement curve of the beams.

Displacement gauges were arranged in the support, 1/4 points, and the mid-span. In each loading process, the corresponding load and displacement values were recorded synchronously.

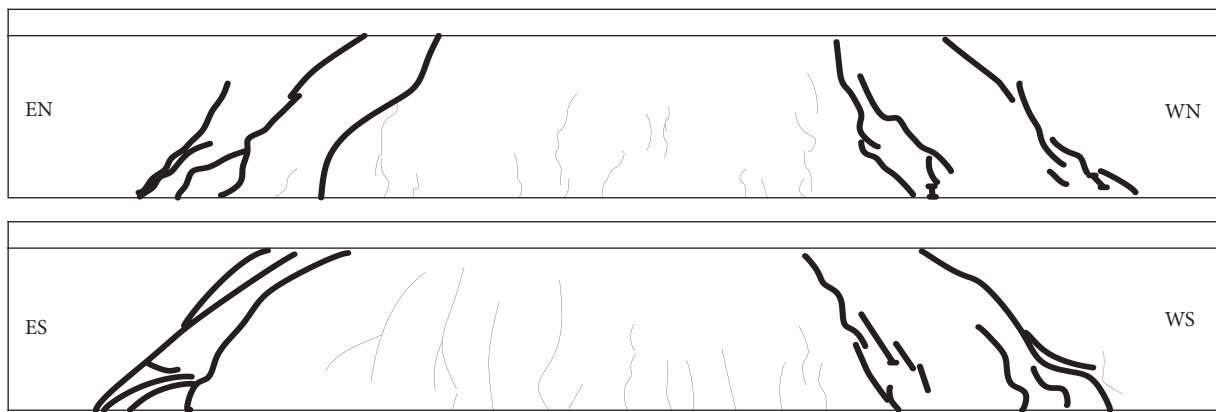
3. Test Results

3.1. Summary of Load Capacity. The crack load (V_{cr}), ultimate load (V_u), and the mid-span displacement (U_{max}) corresponding to the ultimate load of these three beams are shown in Table 4. The load-displacement curve is shown in Figure 2.

3.2. Summary of Crack Development Status. Three test T-beams were carried out under 200 KN, 500 KN, 800 KN, 1000 KN, 1100 KN, and 1200 KN. The results are shown in Table 5. The crack diagram of each beam is shown in Figure 3.



(a) Crack diagram of 1# beam



(b) Crack diagram of 2# beam



(c) Crack diagram of 3# beam

FIGURE 3: Crack diagram of each beam.

TABLE 5: The development status of the maximum crack width (unit: mm).

Node	Load					
	200 KN	500 KN	800 KN	1000 KN	1100 KN	1200 KN
1	0	1.6	2.5	—	—	—
2	—	0.2	1.5	3.31	>4	—
3	—	0.1	0.5	0.63	1.5	—

4. Finite Element Simulation

4.1. *Element Selection and Finite Element Model.* When ANSYS was used for finite element analysis of reinforced concrete, a separate model was adopted. The concrete was simulated by Solid 65 element and steel bar was simulated by Pipe 59 element. The bond slip between the steel fiber and concrete was neglected.

This paper established the 1/2 T-beam model, which can not only reduce the calculation time but also avoid

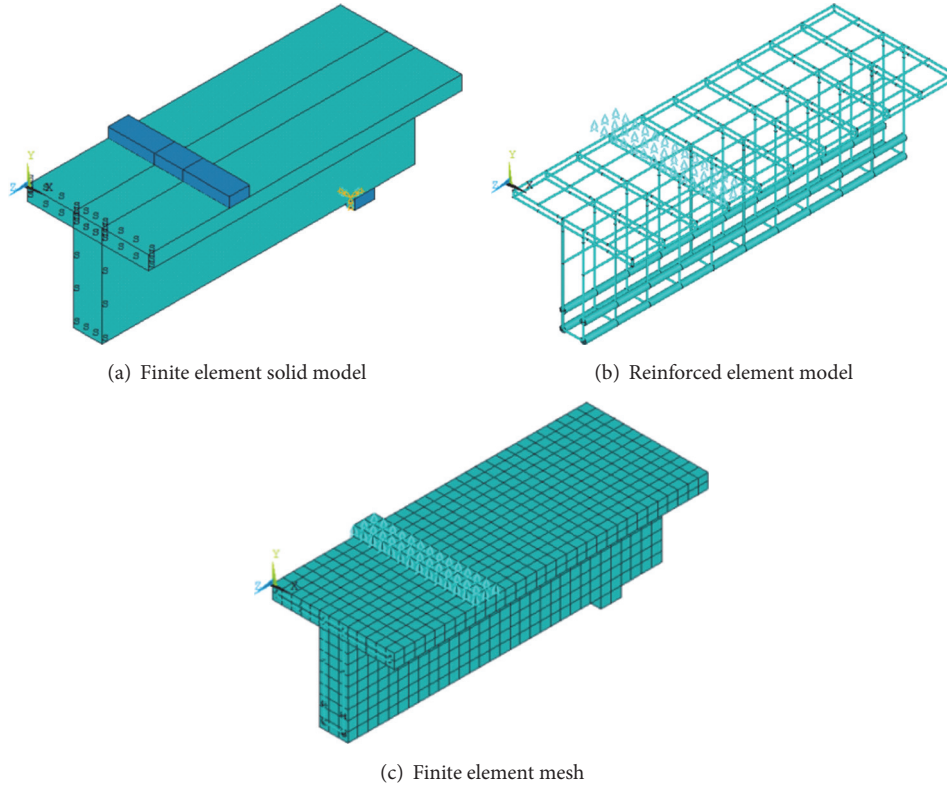


FIGURE 4: ANSYS model.

terminating the calculation during calculation process due to too many warnings. In the finite element simulation, the stress concentration was avoided at the support and the loading point by adding an elastic pad. The ANSYS model is shown in Figure 4.

4.2. Selection of Constitutive Model of Materials. The double-line strong hardening model (BISO) was used in the constitutive relation of the steel bar, and the formula about uniaxial compressive stress-strain curve of concrete [7] is (1) and (2). The constitutive relation of SFRC is modified on the basis of concrete [8–10], and the following formula (4) is used.

Constitutive relation of concrete is as follows:

Ascending stage is

$$y = \frac{Nx - x^2}{1 + (N - 2)x}. \quad (1)$$

Descending stage is

$$y = \frac{x}{\alpha(x - 1)^2 + x}. \quad (2)$$

In the formula,

$$\begin{aligned} x &= \frac{\varepsilon}{\varepsilon_c}, \\ y &= \frac{\sigma}{f_c}, \\ N &= \frac{E_0}{E_s}, \end{aligned} \quad (3)$$

where f_c is compressive strength of concrete; ε_c is peak strain associated with f_c ; E_0 is initial elastic modulus of concrete; E_s is secant modulus at the peak strain.

Constitutive relation of SFRC is

$$\frac{f_c}{f_c^l} = \frac{\beta(\varepsilon/\varepsilon_0)}{\beta - 1 + (\varepsilon/\varepsilon_0)^\beta}. \quad (4)$$

In the formula,

$$\begin{aligned} \beta &= 0.5811 + 1.93\lambda_f^{-0.7406} \\ \lambda_f &= \frac{\rho_f l_f}{d_f}, \end{aligned} \quad (5)$$

where ρ_f is volume fraction of steel fiber, l_f is steel fiber length, and d_f is steel fiber diameter.

TABLE 6: Cracking load and ultimate load of three test T-beams.

Beam note	$V_{cr,exp}$ (KN)	$V_{cr,cal}$ (KN)	$V_{cr,cal}/V_{cr,exp}$	$V_{u,exp}$ (KN)	$V_{u,cal}$ (KN)	$V_{u,cal}/V_{u,exp}$
1	200	213	1.065	830	810	0.976
2	400	364	0.91	1150	1270	1.104
3	300	411	1.37	>1200	1420	<1.183

Note. $V_{cr,exp}$ and $V_{cr,cal}$, respectively, represent the cracking load of the test and the finite element simulation; $V_{u,exp}$ and $V_{u,cal}$, respectively, represent the ultimate failure load of the test and the finite element simulation.

4.3. Comparative Analysis of Finite Element Results and Test Results

4.3.1. *Comparative Analysis of Load-Displacement Curve and Load Carrying Capacity.* The comparisons of test data with ANSYS simulations are shown in Figure 5.

The cracking load and ultimate load of three test T-beams are shown in Table 6.

According to the 1–3# beam, it can be seen that the load-displacement curve of the finite element is basically consistent with that of the test, and the gap of the failure load is not big. But the slope of the curve obtained by finite element method is slightly larger than that of the test chamber. The stiffness of the SFRC beam simulated by the finite element is slightly more than that of the test result. The main reason for this situation is the simulation of concrete inner and SFRC inner was ideal and with no flaw. In addition, due to the compacting process of beams in the actual process, the stiffness of the beam simulated by ANSYS is greater than that of test T-beam.

ANSYS simulation results showed that the test T-beam in the process of loading had experienced two stages, elastic and inelastic, along with the increase of load. The slope of the load-displacement curve was gradually reduced. The load-displacement curve obtained from the test also reflected the process of the stiffness degradation.

The volume fraction of steel fiber of 1#, 2#, 3# test T-beam, respectively, was 0, 1.5%, and 2%. From Figure 5(d), it can be seen that the slope of the 2# beam and 3# beam in the elastic stage and the nonelastic stage is significantly greater than that of the 1# beam, which proves the adding of steel fiber can improve the stiffness and ductility of the concrete beam. In the nonelastic stage, the higher volume fraction of steel fiber is, the slower stiffness degradation of the concrete is. Figure 5(e) curves obtained from the test also reflect this characteristic.

From Table 6, it can be seen that the results of the cracking load and the ultimate failure load simulated by finite element analysis are not quite different from the tests result, and the ratio is close to 1. With the incorporation of steel fiber, the ultimate bearing capacity has been significantly improved. And the higher the volume fraction of steel fiber, the higher the ultimate bearing capacity.

4.4. Crack Distribution and Comparative Analysis of Damage.

From Table 6, the finite element simulation results showed that, in the aspect of cracking loads, the cracking load of the test T-beam increases with the increase of volume fraction of

steel fiber, which reflected that the initial cracking of the steel fiber can be suppressed by the addition of steel fiber. However, the cracking load of 3# beam is smaller than that of 2# beam, which could be caused by the uneven mixing of steel fiber.

The smeared crack model was used in ANSYS to simulate the distribution and development of cracks, with the lack of ability to simulate single fracture of crack width and crack development. From the crack distribution, it can be seen that the ordinary concrete beam cracks and SFRC beam cracks almost distributed in the whole beam section, and the results gained from half length of the beams were compared in Figure 6. Shown by the comparison, the fracture distributions simulated by finite element are in a good conformation with the fracture distributions during actual test.

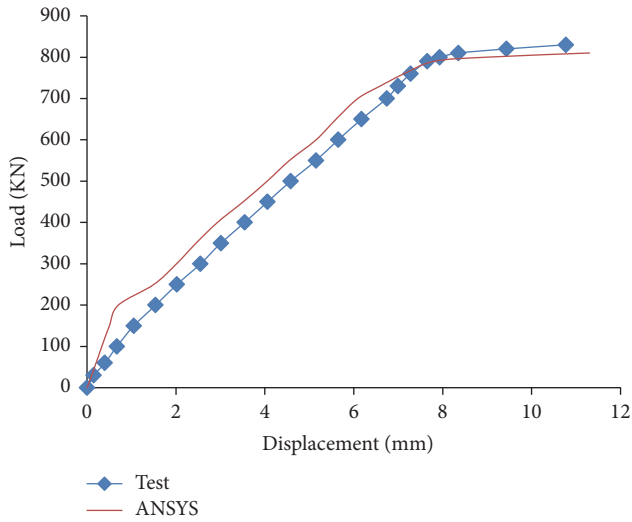
From the crack distribution, it can be seen that the main crack spacing of beam 1 is smaller than that of beam 2 and beam 3. In Figure 6, θ_i ($i = 1, 2, 3$) represents the main crack development angle of each beam; h_i ($i = 1, 2, 3$) represents the cross crack length produced by each beam. Since main crack development angle θ_1 of beam 1 is less than θ_2 and θ_3 , it shows that the incorporation of steel fiber can cause the crack to be dispersed and avoid the damage caused by the stress concentration. In cross crack area, the crack length h_1 produced by beam 1 is smaller than h_2 and h_3 , besides $h_3 < h_2$, which reflects that the addition of the steel fiber can increase the bending crack resistance.

The crack width of beam 1, beam 2, and beam 3 is compared in Table 5. The occurrence of cracking of beam 1 was the earliest, and the crack development speed was the fastest. Beam 2 and beam 3 almost simultaneously cracked, but, in the same load conditions, the crack width of beam 3 was smaller and the crack development speed was slower than beam 2. In the elastic stage of beam 2, the crack developed slowly, but, after the elastic stage, the crack developed quickly, which showed that the increase of volume fraction of steel fiber can improve the crack resistance of the concrete and delay the development of cracks. Because when volume fraction was greater than 2%, it is difficult to blend steel fiber in concrete, so the study was not done.

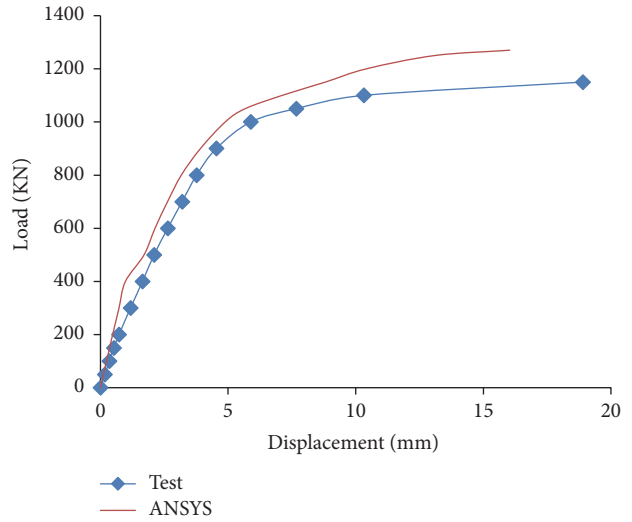
5. Conclusions

Through the above test and finite element simulation analysis, the following conclusions can be drawn:

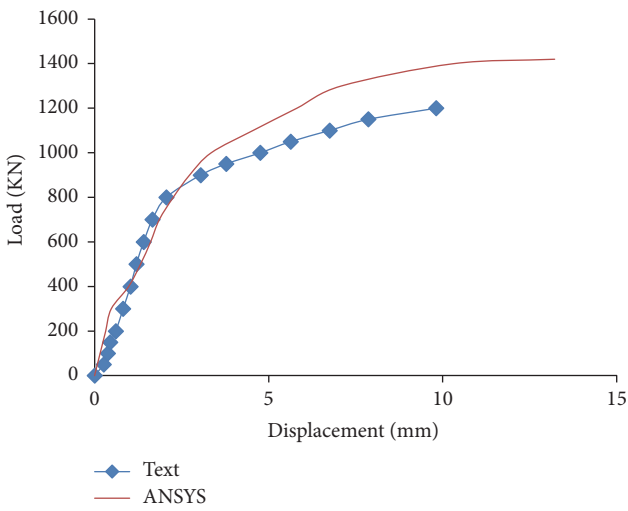
- (1) The incorporation of steel fiber can improve the integral rigidity and ductility of concrete T-beam. In a certain range, the higher the volume fraction of steel



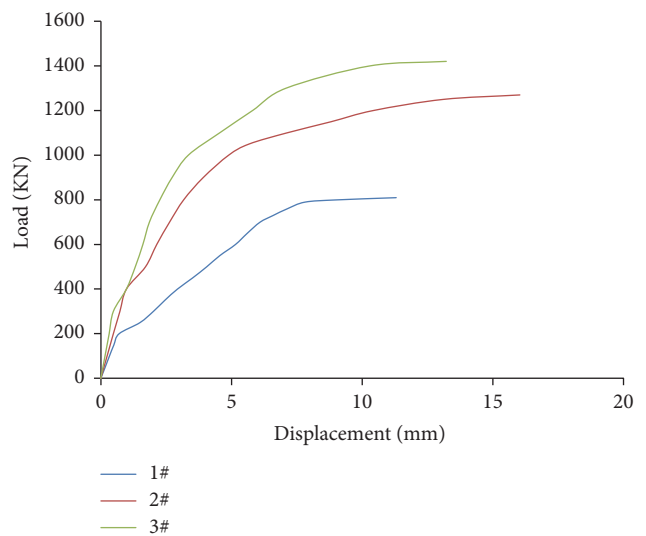
(a) 1# beam comparison diagram



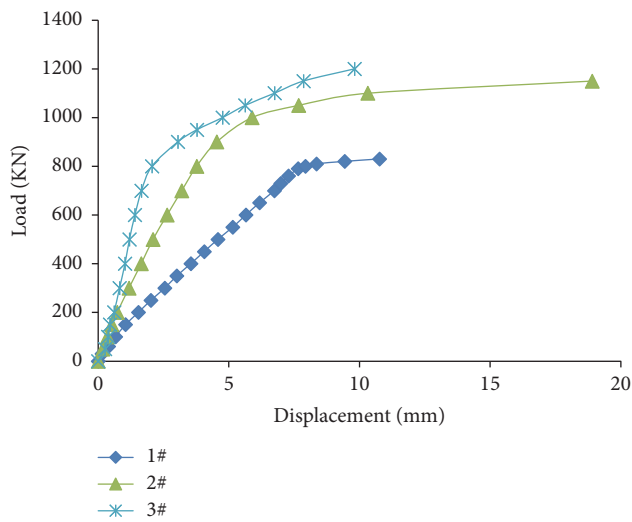
(b) 2# beam comparison diagram



(c) 3# beam comparison diagram



(d) Test results



(e) ANSYS results

FIGURE 5: Comparison of the results of test with ANSYS simulation.

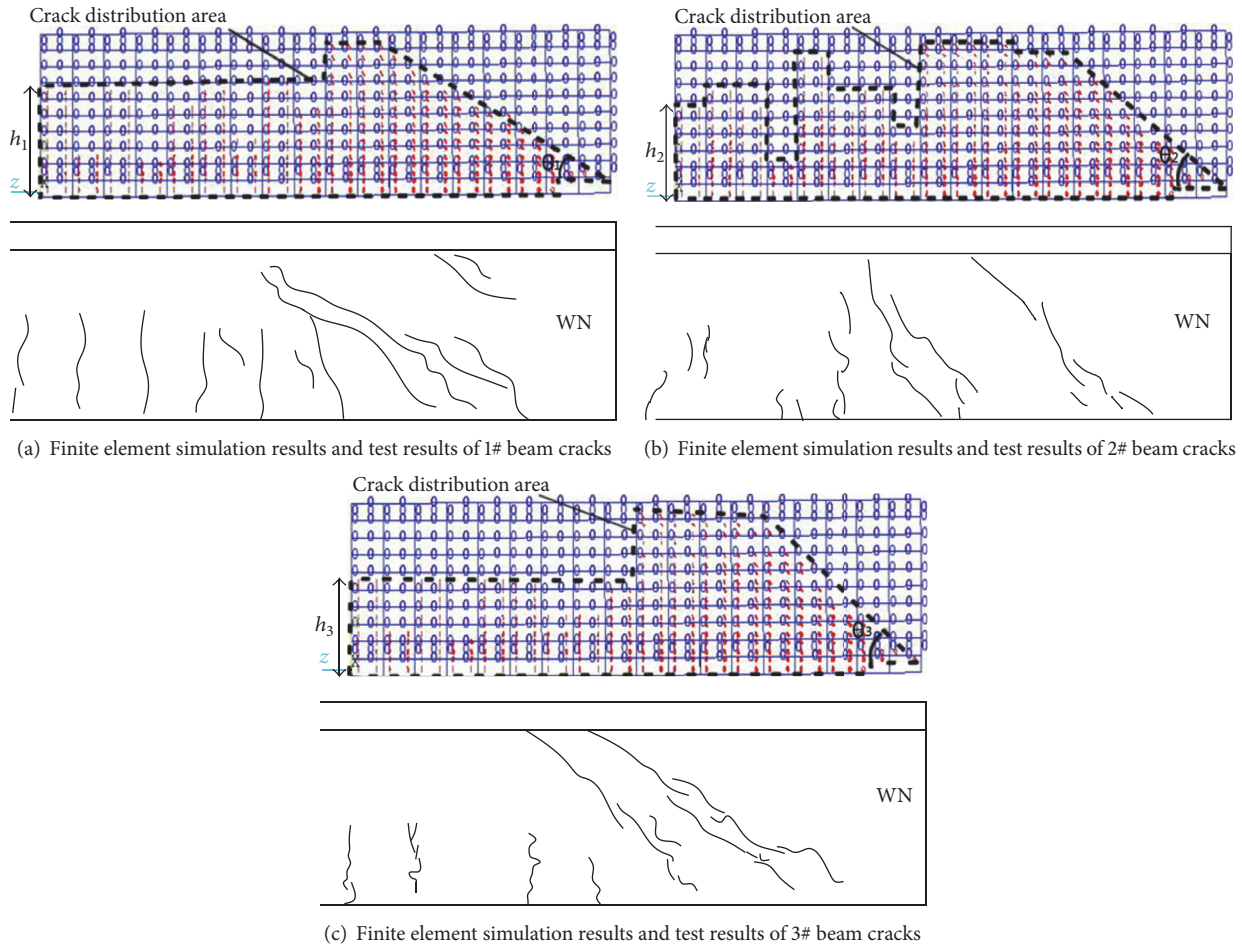


FIGURE 6: Finite element simulation and test results of the cracks of each beam.

fiber is, the higher the integral rigidity is and the slower the stiffness degradation of T-beam is.

- (2) With the same reinforcement ratio and shear span ratio, the higher volume fraction of steel fiber is, the higher the ultimate shear bearing capacity of the concrete T-beam is.
- (3) The increase of volume fraction of steel fiber can delay the development of cracks and make the distribution of cracks more uniform and also improve crack resistance of the concrete T-beam when volume fraction was less than 2%.
- (4) Finite element analysis of SFRCT-beams by ANSYS is feasible, and the results obtained by ANSYS are in good agreement with test results. ANSYS can simulate the general trend of the crack and the crack distribution area of the T-beam by using the smeared crack model.

Conflicts of Interest

The authors declare that they have no conflicts of interest.

Acknowledgments

The research described in this paper was financially supported by the Jiangsu Province Key Laboratory of Structure Engineering, located in Suzhou University of Science and Technology.

References

- [1] X. Sun, B. Diao, and Y. Ye, "Flexural behavior experiments of ultra-high performance concrete beams reinforced with steel bar and hybrid-fiber," *Industrial Architecture*, vol. 42, no. 11, pp. 16–21, 2012.
- [2] Z. Y. Sun, Y. Yang, W. H. Qin, S. T. Ren, and G. Wu, "Experimental study on flexural behavior of concrete beams reinforced by steel-fiber reinforced polymer composite bars," *Journal of Reinforced Plastics and Composites*, vol. 31, no. 24, pp. 1737–1745, 2012.
- [3] H.-Z. Zhang, C.-K. Huang, and R.-J. Zhang, "Experimental study on shear resistance of steel fiber reinforced high strength concrete beams," *Journal of Harbin Institute of Technology*, vol. 38, no. 10, pp. 1781–1785, 2006.
- [4] J.-S. Cho, *The Shear Behavior of Steel Fiber Reinforced Prestressed Concrete Beams without Shear Reinforcement*, The University of Texas at Arlington, Arlington, Tex, USA, 2011.

- [5] B.-X. Shi, "Experiment study on fatigue characteristic of steel fiber reinforced concrete," *Journal of Hebei University of Engineering (Natural Science Edition)*, vol. 25, no. 2, pp. 9–12, 2008.
- [6] L. Wang, *Study on the Properties of Ultra-Short Ultra-Fine Steel Fiber Reinforced Concrete*, Chongqing Jiaotong University, Chongqing, China, 2011.
- [7] Y. Li, X. Wang, and S. Chen, "Comparison of stress-strain curves of concrete under uniaxial compression," *Highway Traffic Department*, vol. 10, pp. 75–78, 2005.
- [8] J. Qiu, "Study on nonlinear finite element analysis of steel fiber concrete structure," *Concrete*, no. 3, pp. 17–20, 2011.
- [9] D. A. Fanella and A. E. Naaman, "Stress-strain properties of fiber reinforced mortar in compression," *Journal of the American Concrete Institute*, vol. 82, no. 4, pp. 475–483, 1985.
- [10] B. Luccioni, G. Ruano, F. Isla, R. Zerbino, and G. Giaccio, "A simple approach to model SFRC," *Construction and Building Materials*, vol. 37, pp. 111–124, 2012.

Research Article

Numerical Simulations of Restrained Shrinkage Cracking in Glass Fibre Reinforced Shotcrete Slabs

Andreas Sjölander and Anders Ansell

KTH Royal Institute of Technology, Division of Concrete Structures, 100 44 Stockholm, Sweden

Correspondence should be addressed to Anders Ansell; anders.ansell@byv.kth.se

Received 9 February 2017; Accepted 9 April 2017; Published 3 May 2017

Academic Editor: Peng Zhang

Copyright © 2017 Andreas Sjölander and Anders Ansell. This is an open access article distributed under the Creative Commons Attribution License, which permits unrestricted use, distribution, and reproduction in any medium, provided the original work is properly cited.

Modern tunnels in hard rock are usually constructed by drill and blast with the rock reinforced by shotcrete (sprayed concrete) in combination with rock bolts. The irregular rock surface and the projection method of shotcrete lead to a tunnel lining of varying thickness with unevenly distributed stresses that affect the risk of cracking during shrinkage of the young and hardening material. Depending on water conditions, shotcrete is sprayed directly either onto the rock surface or over a drainage system, creating a fully restrained or an end-restrained structural system. In this paper, a method for nonlinear numerical simulations has been demonstrated, for the study of differences in stress build-up and cracking behaviour of restrained shotcrete slabs subjected to shrinkage. Special focus was given to the effects of the irregular shape and varying thickness of the shotcrete. The effects of glass fibre reinforcement and bond were implemented in the study by changing the fracture energy in bending and in the interaction between shotcrete and the substrate. The study verifies that an end-restrained shotcrete slab is prone to shrinkage induced cracking and shows the importance of a continuous bond to avoid wide shrinkage cracks when shotcrete is sprayed directly onto the rock.

1. Introduction

A common construction method of tunnels in hard and good quality rock is by drill and blast. One way to reinforce the rock is to use wet-sprayed, fibre reinforced shotcrete (FRS) in combination with rock bolts. The shotcrete keeps loose blocks together and ensures the arch shape of the tunnel which enables the rock to carry its own deadweight. Rock bolts are used to secure individual blocks and to provide structural connection between rock and shotcrete where and if the bond strength is insufficient. The thickness of the applied shotcrete will mainly depend on rock surface geometry, the shotcreting process, and the skill of the operator. In the process of spraying, problems with rebound and difficulties in performing accurate measurements lead to variations in thickness of the applied shotcrete. In tunnels and underground caverns, shotcreted linings usually have an outer harmonic shape but, due to the irregular shape of the rock surface, the shotcrete thickness will also become highly irregular. This introduces local stress concentrations, that is, possible locations for crack initiation, as well as variations in temperature and

shrinkage. Cracks might be initiated in local thin sections [1], while thicker sections lead to an excessive use of material and higher construction costs. Effects of irregular geometry are usually neglected in the design of shotcrete linings, but research regarding stresses in such tunnel linings shows the importance of considering these effects; see, for example, [2–4].

Depending on water conditions in the tunnel, the shotcrete can be sprayed either directly on the rock surface or, for example, partly over a system of soft drain mats. For sections with good water conditions, with no large water leading cracks, shotcrete is sprayed directly onto the rock. The bond between shotcrete and rock will restrain movements due to shrinkage and thermal effects. With complete bond between the sections, formations of several small cracks can be expected due to the restrained movement. This was, for example, showed in a test series performed by Malmgren et al. [5] where cracks due to shrinkage were mapped for shotcrete sprayed against a sandblasted concrete wall. Similar results were presented by Carlswärd [6], but here the shrinkage induced cracking of regular cast concrete was studied.

Groth [7] showed that the distribution and width of the cracks will depend on the bonding and that local debonding leads to severe cracking in that section. However, in none of the experiments above the effects of varying, irregular thickness was considered. For tunnels through sections of infiltrating groundwater, or with high demands on durability, a drainage system must be installed. One solution is to use a system of soft synthetic drain mats which are placed to collect and transport the water to a drainage system. Rock bolts are used to keep the mats in place and the whole system is then covered with shotcrete which will bond to the rock at the end of each section, called bonding zones in this paper. However, the much lower stiffness of the drain mat compared to the shotcrete enables the shotcrete to deform freely between the bonding zones, thus creating an end-restrained slab. In situ mapping and evaluation of a motorway tunnel in Stockholm, Sweden, by Ansell [8] showed extensive shrinkage cracking in shotcrete sprayed on soft drains. Typically, one wide crack appeared in each section, partly due to the strain-softening behaviour of the FRS. Similar behaviour was also found in a test series by Bryne et al. [9] where the end-restrained shrinkage cracking of shotcrete sprayed on soft drains was simulated in laboratory tests. This investigation also involved testing of shotcrete reinforced with glass fibres and evaluation of their effect on delaying and reducing shrinkage cracking. Glass fibres will not be long-term active due to degradation in the alkaline environment inside shotcrete but will be fully effective during the early age, when the risk of shrinkage cracking is at its highest [10]. Addition of many small fibres will distribute stresses within the shotcrete in a way that is not possible with structurally active, fewer, and larger steel fibres. A possible future solution is to combine glass microfibres with steel or synthetic, macrofibres in the shotcrete. The sprayability of such material has also been tested [9].

The aim of this paper is to find a numerical analysis strategy based on the finite element (FE) method, suitable for evaluation of this type of results and for future use in the design process. The model will capture the shrinkage properties of shotcrete and describe the difference in structural behaviour between the two structural systems described, that is, shotcrete fully bonded to rock and with end restraints only. The stress build-up and resulting crack patterns from the analysis model are studied and compared with the in situ results, also including results from testing on shrinking ordinary cast concrete. Special attention is given to the effects from irregular geometry, but the importance of bond strength and partial debonding is also covered but, however, not in the main focus. More studies regarding the influence a varying thickness are presented by Sjölander et al. [10–12].

2. Materials

Due to the difficulties in finding accurate material data for shotcrete in the literature, a common but not correct approach is to use material properties of ordinary, cast concrete. The use of different set accelerators and larger cement ratio in shotcrete will affect material parameters such as shrinkage and strength development [13]. Over the last years, the focus on research of material properties and behaviour of

young shotcrete has increased; see, for example, Bernard [14], Bryne et al. [15], and Ahmed [16]. The material properties used for the numerical models in this paper were based on the experimental work on young and hardened shotcrete presented by Bryne et al. [15]. For the cast concrete slabs and granite blocks used as substrate in the numerical models, typical material parameters were used. Elastic conditions were assumed, with Young's modulus and Poisson's ratio set to 70 GPa and 0.2 for granite and 35 GPa and 0.2 for concrete, respectively.

2.1. Fibre Reinforced Shotcrete. Typically, FRS shows a strain-softening behaviour and the type of fibres added to the shotcrete is divided into two categories: macrofibres, sometimes called structural fibres, and microfibres. Macrofibres are used to increase the ductility of shotcrete, while microfibres can be added to, for example, decrease the risk of fire spalling of shotcrete [18] and shrinkage cracking [13]. Microfibres are usually made of glass or synthetic material and an increase of the fracture energy with a factor of 1.1–2.0 could here be expected [19–21]. Macrofibres are of steel or synthetic/plastic material and can increase the fracture energy significantly; see, for example, [22]. The fracture energy obviously depends on amount, type, distribution, and orientation of the fibres in the specimen. A scatter in the results of fracture energy from experiments can therefore be expected. The bond strength between shotcrete and rock mainly depends on the cleanness of the surface and type of rock. Results for normal bond strength are, compared to shear bond strength, commonly found in the literature. However, results for both normal and shear directions, as well as interaction between the two, are rare. A test series presented by Bryne et al. [17] shows that a normal bond strength up to 1.0 MPa can be achieved within 24 hours of curing. This can, for example, be compared with the study by Bernard [14] which shows that a bond strength of only 0.2 MPa was achieved within the first 24 hours. This exemplifies the scatter in results found in the literature and the importance of also considering the type of substrate, curing environment, and material composition. Further examples are given for comparison in Table 1. As a basis for the following numerical examples, material properties from the tests performed by Bryne et al. [15] were used. The development of tensile strength of plain and glass fibre reinforced shotcrete was investigated, with standard four-point bending tests according to EN 14488-3 [23] performed at different time intervals. However, no measurements of the fracture energy were done for the test series that each consisted of three beams sawn out from one sprayed shotcrete slab.

2.2. Material Models. The ductility of the shotcrete material studied here was previously investigated through laboratory testing [15], with four-point loading of standard concrete beams $500 \times 75 \times 125 \text{ mm}^3$ (length \times height \times width) [23]. Due to the absence of structural reinforcement, the measured postcracking behaviour is captured by a few data points, with the first postcracking point usually found at a displacement of 0.6–0.8 mm with a corresponding force of 0.4–0.6 kN. Due to the few data points from each test, the postcracking softening

TABLE 1: Compilation of test result for normal and shear bond strength at early age, with σ and τ as the normal and shear bond strengths, respectively.

Reference	Surface	Material	Test conditions	σ (MPa)	τ (MPa)
Bernard [14]	Various	Shotcrete	In situ	0.2	—
Hahn [29]	Granite	Shotcrete	Laboratory	0.3–1.7	—
Silfwerbrand [28]	Concrete	Shotcrete	In situ	0.38	2.85
Saiang et al. [30]	Magnetite and trachyte	Shotcrete	Laboratory	0.56	0.50
Ellison [31]	Granite	Shotcrete	In situ	1.37	—
Bryne et al. [17] ²	Granite	Shotcrete	Laboratory	1.50	—
Silfwerbrand [28]	Concrete	Shotcrete	Laboratory	1.72	3.35
Moradian et al. [32] ¹	Barre granite	Concrete	Laboratory	—	4.79

¹Results are mean values from presented results with a bonding of 100%.

²Results are mean values after three days of curing.

TABLE 2: Material parameters for the damage plasticity model. See Figure 1 for explanation of material parameters.

Shotcrete	Slab	F_{cr} (kN)	δ_{cr} (mm)	E (GPa)	σ_t (MPa)	G_f (Nm)	σ_1 (MPa)	σ_2 (MPa)	w_1 (mm)	w_2 (mm)
Plain, 7 days	1* -2	8.75	0.14	31	3.64	125	0.036	—	0.08	—
5 kg/m ³ , 7 days	3	7.55	0.15	29	2.64	139	0.317	0.0264	0.06	0.32
5 kg/m ³ , 14 days	4*	6.31	0.14	29	2.00	139	0.240	0.0200	0.09	0.40
10 kg/m ³ , 7 days	5* -6	9.00	0.15	29	3.48	147	0.522	0.0348	0.05	0.21

*Analysed using FE modelling.

behaviours for plain and glass fibre reinforced shotcrete were therefore assumed here as linear and bilinear, respectively. These basic strain-softening curves, as proposed by, for example, [24, 25] and shown in Figure 1, have been used here as input to a finite element (FE) model of the test beams, in order to verify the material model behaviour for the following numerical studies. A beam model with fully integrated 2D plain strain elements, C3PS in the analysis program Abaqus [26], was used, with the mesh size set to 5 mm and with a prescribed displacement used as load. The results are shown in Figure 2, plotted together with the corresponding load-displacement curves from the laboratory tests. The material parameters used for modelling this tensile behaviour with the damage plasticity material model in Abaqus are given in Table 2. The relation between fracture energy G_f , crack width w , and tensile stress σ_t is for the linear case given by

$$G_f = \frac{(\sigma_t - \sigma_1) w_1}{2}, \quad (1)$$

and in the case of the bilinear softening given by

$$G_f = \frac{\sigma_1 w_1 + \sigma_2 w_2 - \sigma_2 (w_1 + w_2)}{2}. \quad (2)$$

The minimum stress in each case above, that is, σ_1 and σ_2 for (1) and (2), respectively, was limited to $\sigma_t/100$ to avoid numerical problems. Values for plain, unreinforced shotcrete and versions with a different amount of glass fibres added are given. For each of the four types included, the material parameters are valid for 7 or 14 days of age, corresponding to times of failure for tested shotcrete slabs; see [15] and the presentation in the following sections.

An important part of the modelling of the shotcrete behaviour is to find an accurate model for the material interaction at the interface between shotcrete and substrate. For each model, the interaction between the structural elements at the interface was modelled in four different ways (A–D), to investigate the influence and importance of debonding. The interaction was modelled using a master-slave surface interaction and, for model A, an elastic criterion was used which enforces all movements from the master surface to the slave surface during the analyses. A damage-based behaviour was implemented for models B–D, based on a stiff elastic behaviour between the two surfaces up to a critical stress level [26]. The stiffness of the surfaces is calculated based on a maximum slip between the master and slave nodes of 0.5% before damage is initiated. The critical normal and shear bond stresses were set to 1.5 and 3.0 MPa, respectively, which is in agreement with results presented in Table 1. The failure criterion was defined based on a single stress parameter; that is, the interaction between normal and shear stress with respect of failure was not considered. The damage evolution was based on fracture energy with linear softening, as described in Figure 1. The critical nodal displacement w_b , at which full debonding occurs, is based on the relation between fracture energy G_b and critical tensile stress σ_b , according to

$$G_b = \frac{\sigma_b w_b}{2}, \quad (3)$$

following the same formulation as in (1). The fracture energy for debonding in the normal direction according to models B–D was set to 125, 40, and 10 Nm, which corresponds to a nodal displacement in the normal direction of 0.167, 0.05, and 0.01 mm, respectively.

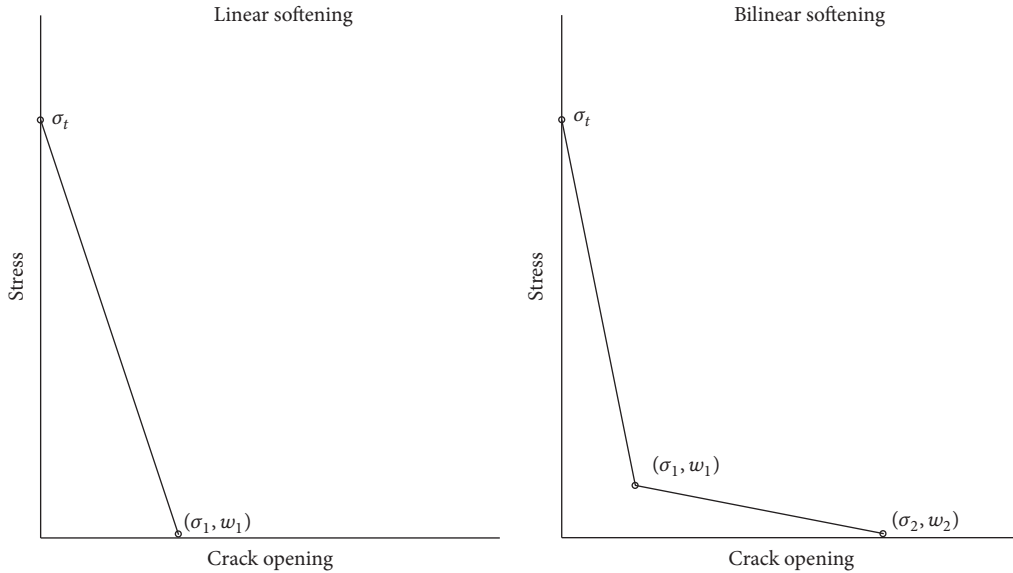


FIGURE 1: Schematic view of linear and bilinear strain softening.

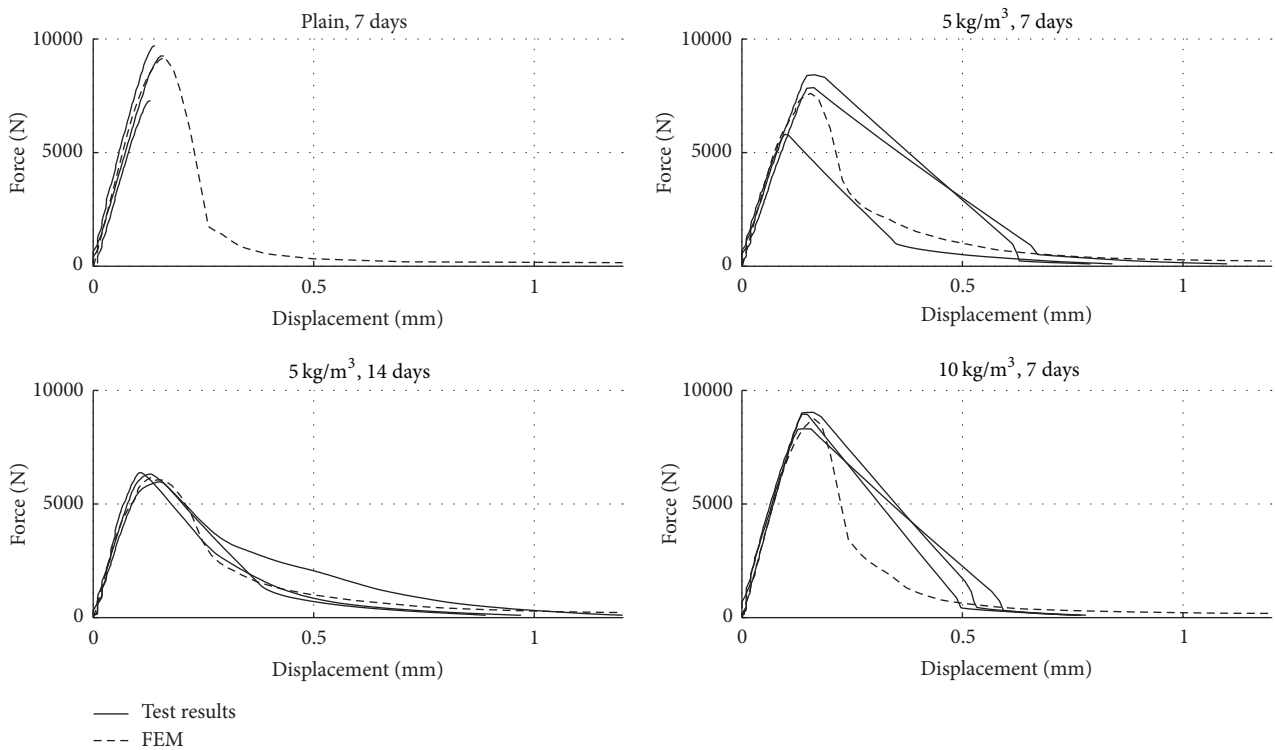


FIGURE 2: Force-displacement curves from experimental tests [15] and numerical analyses.

3. Methods

Two cases are studied in the following, the first with the aim to verify the behaviour of the material model used for shrinking concrete and shotcrete and the second to assess previously conducted laboratory tests with shrinking shotcrete slabs. For the numerical simulations, the FE software Abaqus [26] was used also in this case, with the nonlinear behaviour of

plain and fibre reinforced shotcrete governed by a concrete damage plasticity model. The material parameters given in Table 2 were used, describing the same materials as was tested by the previously presented 2D beam model. The effects of the fibre reinforcement were here accounted for through an increase of the fracture energy. The bond between the shrinking overlay and the substrate, which, for the two cases, are concrete and granite, is modelled as described in the

previous section, using four different approaches that will be compared in the following examples. The deformation properties of the substrates are assumed to correspond to a linear material behaviour. For the analyses, 3D models were created using brick elements of type C3D8R, with linear and reduced integration. An implicit solver was used and the error tolerance for equilibrium was set to 5%. For the substrate materials, coarser meshes could be used and all translations of the lower surfaces were restricted. The analyses of the effects due to differences in restrained movement and irregular thickness focus on the crack distribution and the shrinkage over the shotcrete cross section was therefore considered as a uniformly distributed field. The aim was not to fully reproduce the experimental results but to compare results from the evaluation of the structural behaviour. The development of material properties with shotcrete age has not been incorporated into the model and instead the material properties are chosen as valid at the age of cracking, as observed during testing and here given in Table 2.

3.1. Shrinkage Cracking of Concrete Beams. The first case studied is based on experiments performed with concrete beams cast on a concrete substrate. The aim is here to verify the model behaviour through comparison with detailed results demonstrating cracking and debonding for fully and partially restrained test specimens. Since such laboratory results for shotcrete are missing, the test series by Carlswärd [6] were here used, although performed with cast concrete. The concrete used has properties that are slightly different from the description given in the previous sections, but here the focus is on the principal behaviour of the FE model and location of the shrinkage cracks that appear. The thickness of the concrete overlays is representative for the required shotcrete thickness for tunnels in rock with good quality. In the test series, a number of plain, fibre reinforced and steel bar reinforced concrete beams was cast on concrete slabs with different surface treatment, of which results for four plain unreinforced beams are used here. The dimensions of the test beams were $2500 \times 150 \times 50 \text{ mm}^3$ (length \times width \times height), as shown in Figure 3. Here are also indicated areas with no bond between beams and substrate, which was incorporated for some of the test beams to simulate the effect of partial loss of bond. Shrinkage strains in the beams were measured and crack patterns and debonded areas were mapped during a period of over 100 days of concrete shrinkage. The strains and stresses measured during testing corresponded to a free shrinkage of around $600 \mu\epsilon$, but large variations in strain between upper and lower surface due to the one-sided drying condition were observed. For further details on the experimental setup, see [6]. For the FE analysis of shrinkage cracking of the fully restrained and partially debonded beams, the material model corresponding to plain shotcrete in Table 2 was used. The FE mesh was generated with a global mesh size of 15 mm and the shrinkage was applied as an equivalent, linearly increasing and uniformly distributed temperature field, here up to $500 \mu\epsilon$. The expansion bolts used in the experimental setup were considered by using a tie command for one row of elements between the beam and slab. The different cases of partial debonding indicated in

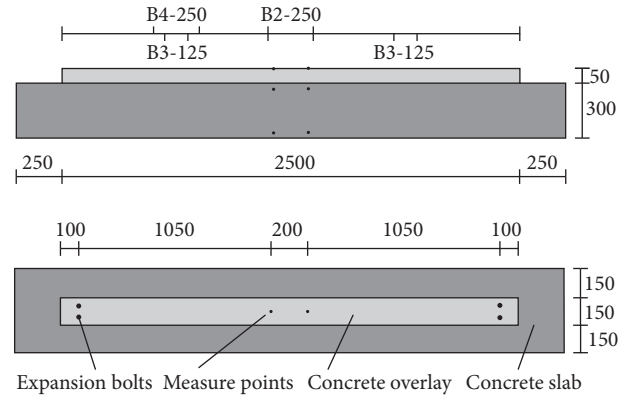


FIGURE 3: Vertical and horizontal view of test setup for shrinkage cracking testing for plain concrete beams [6]. For beams B2, B3, and B4, positions and length of initial debonding are shown. Measurements are in mm.

TABLE 3: Amount of glass fibre reinforcement, time at failure due to shrinkage, and measured thickness for slabs 1–6 tested by Bryne et al. [17]. Slabs S1, S4, and S5 are here analysed using FE modelling.

Slab	Fibre content (kg/m^3)	Failure (days)	Thickness (mm)		
			Min	Max	Mean
S1*	0	6	12	38	25
S2	0	7	21	45	33
S3	5	6	19	48	32
S4*	5	14	25	45	37
S5*	10	7	20	58	37
S6	10	6	17	57	41

* Analysed using FE modelling.

Figure 3 were set at the start of analysis, depending on which test beam was studied.

3.2. Shotcrete Slab Shrinkage. The second case consists of a test series of shotcrete slabs sprayed on simply supported granite blocks [17] $1100 \times 400 \times 100 \text{ mm}^3$ (length \times width \times height), instrumented with strain gauges to record bending strains. The aim with this setup was to represent an in situ case in which synthetic mats are used to drain infiltrating water. The drainage system and the corresponding experimental setup are shown in Figure 4. The thickness of the slabs was considered to be uniform and the granite to be crack-free and without other imperfections. Two layers of plastic sheet were placed over a $700 \times 400 \text{ mm}^2$ centre area of the slabs prior to shotcreting, to simulate the effect of shotcrete sprayed on soft drain mats. This created an area of free horizontal movement for the shotcrete sprayed over the plastic film and granite slab, only bonding to the granite block over an area of $200 \times 400 \text{ mm}^2$ at each end. Six slabs, S1–S6, were sprayed and monitored in a laboratory environment. The slab thickness, glass fibre content, and time at first shrinkage crack appearance are shown in Table 3. The thickness of the shotcrete slabs between the bonding zones was measured using a mechanical profile measuring device over a basic grid pattern of $50 \times 10 \text{ mm}^2$. In the vicinity of the cracks, a denser grid pattern

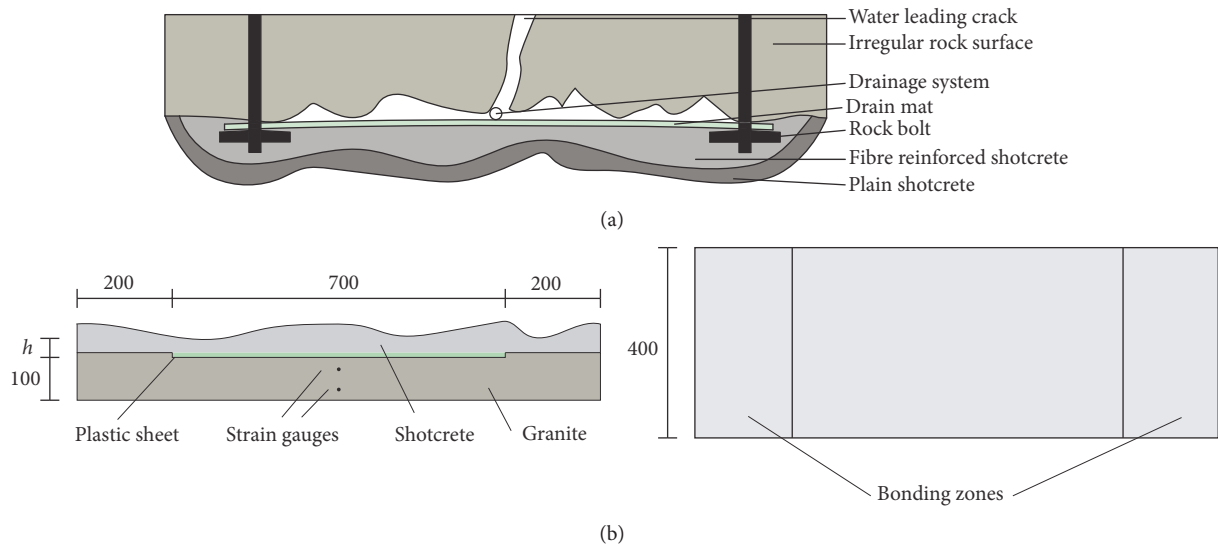


FIGURE 4: (a) shows the in situ principle of a drainage system with synthetic drain mats. (b) shows test setup for shrinkage cracking testing [17] of shotcrete slabs with varying thickness. Vertical and horizontal view. Measurements in (mm).

of $10 \times 10 \text{ mm}^2$ was used. The measured strain in this case corresponded to a free shrinkage of approximately $200 \mu\epsilon$. For further details on the testing procedure and results, see [9, 15, 17]. To capture the measured irregularities, that is, the topography, of the slabs in the FE model, a global mesh size of 5 mm was used. A point cloud for the upper surface of each slab was created from the measured thickness and linear interpolation between measured points was used to make this cloud denser. The lower surface of the shotcrete slab which was in contact with the plastic sheet was however considered to be perfectly flat. With the use of the software HyperMesh [27], the two point clouds were merged into a solid element mesh. Numerical analyses of three of the six end-restrained slabs are presented here, with full bond between shotcrete and granite assumed at the end areas only. For comparison was also a case with fully restrained shrinkage performed with this setup, simulating the absence of the plastic sheet before spraying and thus full bond to the granite. Here, also the four formulations A–D for the bond interface interaction were tested. Also for these FE models, the shrinkage was applied as an equivalent, uniformly distributed temperature field, here up to $200 \mu\epsilon$ for the end-restrained case and to $2000 \mu\epsilon$ for the fully bonded case.

4. Results and Discussion

The following two sections present the FE results from the analyses of the shrinking concrete beams and shotcrete slabs. When discussing the results, the term “damage initiation” will be used when plastic strains have formed and “crack” is used for crack widths over 0.05 mm.

4.1. Shrinkage Cracking of Concrete Beams. Experimental and numerical results based on the concrete beam model and laboratory tests are presented and compared in Figure 5. Because different material properties were used in the numerical

simulations compared with the ones in the experiments, a detailed comparison with respect to crack widths will not be fully accurate. The overall structural behaviour of the experiments was however captured by the numerical simulations, with respect to debonding and crack patterns. It should be noted that, in the simulations, debonding was set at the start of the analysis while it, in the experiments, occurred during the monitoring. It can be seen that the numerical simulations resulted in only thin cracks in the fully restrained beam in Figure 5(a) and that narrow cracks appeared for the beams with partial debonding in Figures 5(b)–5(d). The experimentally obtained crack widths were thus larger than those obtained in the numerical simulations, indicating a stiffer behaviour in the numerical analyses. Possibly, one cause of the stiffer behaviour can be the differences between the shotcrete material properties used in the simulations and that of the concrete used in the experiments [6]. Another possible explanation is the use of the concrete damage plasticity model implemented in Abaqus [26]. This model is based on damage localization in one element, with a subsequent stiffness-degradation, which implies that the fracture process zone of the shotcrete becomes equal to the mesh size in the numerical model. In reality, the fracture process zone and hence the softening will be localized to a larger area which is neglected in the model. It is also possible that the tensile stresses were underestimated since the effects of nonlinear shrinkage, that is, the effects of one-sided drying, here were approximated with a uniform shrinkage. This will cause a strain gradient over the thickness [6] and therefore possibly introduce a bending moment in the beams. However, the results from this model verify in general the structural behaviour of the fully restrained and partially debonded beams. Comparison with the results from [6] clearly shows a correlation between debonding and formation of wide cracks, which thus can be captured by the model.

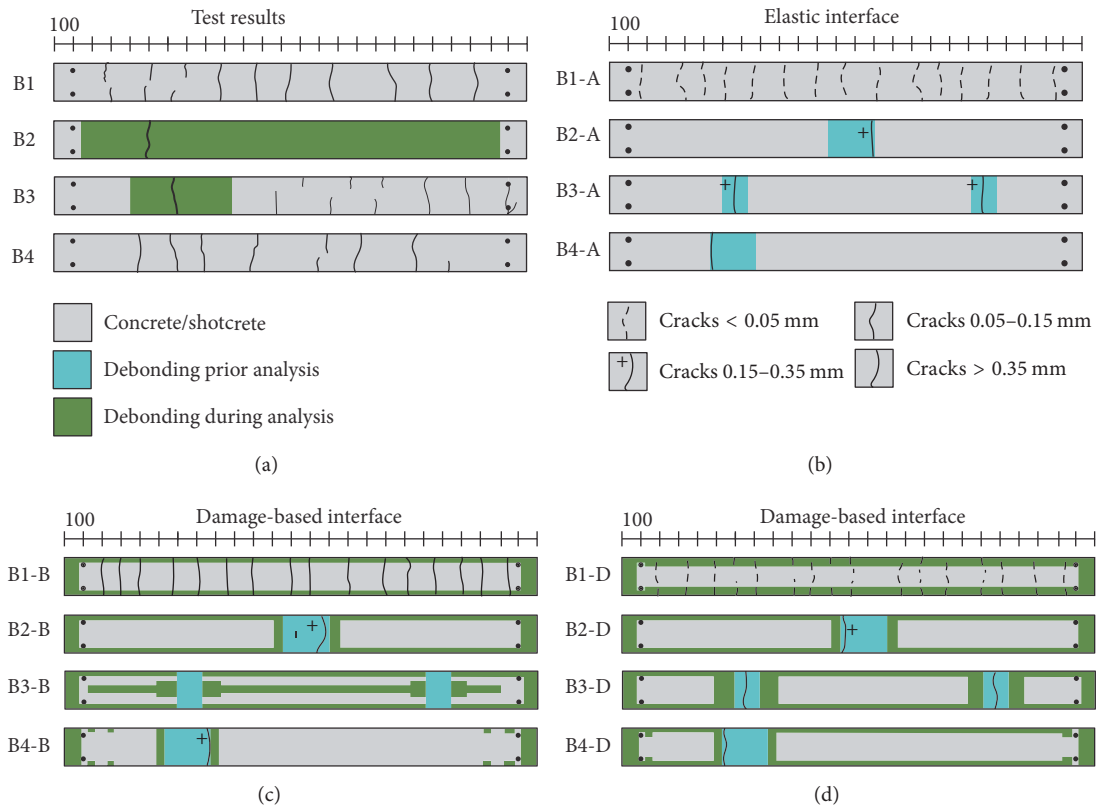


FIGURE 5: Crack patterns for thin beams B1–B4 cast on concrete slabs, (a) experimental results from [6], (b) numerical simulations with elastic interaction, (c) numerical simulations with $G_f = 125 \text{ Nm}$, and (d) numerical simulations with $G_f = 10 \text{ Nm}$. Measurements in (mm).

4.2. Shotcrete Slab Shrinkage. The results from analysis of the shotcrete slabs with varying, irregular thickness are presented in Figure 6, showing results for three of the six slabs tested: S1, S4, and S5. The parts of the slabs shown are the middle parts that are unrestrained from the substrate; that is, the outer areas bonded to and providing anchorage with the granite are not shown. As a comparison, the numerically obtained cracks are shown together with the results from the laboratory tests by Bryne et al. [15]. The cracks are marked with solid and dashed lines for the experimental and numerical results, respectively. As can be seen from the topographical plots (left side), each of the presented slabs only shows one shrinkage crack across the width. During testing, these cracks appeared close to the centre section of the slabs, as theoretically would be the case for a perfect shotcrete slab with even thickness. However, it can be seen here that the cracks adapt to the surrounding topography.

This is also the case for the theoretically obtained cracks, but these tend to be positioned along paths with thinner slab dimensions, which is most striking in slab S4. The sectional plots (right side) show the slab thickness along the cracks, in comparison with the maximum and minimum thickness in all sections across the width of the slabs. For all three slabs, the theoretically obtained (FEM) curves are slightly closer to the minimum curve than are the test curves. However, for slab S4, the difference is greater, indicating that effects, such as variation in ballast and fibre distribution, or spraying defects,

may have influenced the initiation of the crack during testing. It should be noted that, for shotcrete slabs with end restraints only, all the shrinkage deformation will occur at the first opened macrocrack, leading to a full separation of the two parts of the slab, but possibly with some fibres bridging the crack. The numerical analysis and the tests showed that this happened for an average shrinkage strain of around $200 \mu\epsilon$ for all slabs. When comparing the results from slab S4 with that for S1 and S5, it should be noted that the former was older at time of cracking during testing, 14 days compared with 6 and 7 days, respectively. Slab S4 also had slightly different material properties compared with the others, as can be seen from Tables 2 and 3. No other effect from the glass fibre reinforcement could be concluded from this comparison.

Numerical analysis (FEM) results for slabs S1, S4, and S5 with assumed full bond to the subsurface granite are also presented as a comparison. The results in Figure 7 are organized as in Figure 6, with topographical and sectional plots. To simplify comparison, only the 700 mm long centre parts are shown also for this case. It should here be noted that all four models (A–D) for the shotcrete bond were tested during modelling, but all variations for each slab resulted in close to identical results. A comparison with Figure 6 shows that the major difference is that multiple cracks appear in this case, with only a few of the cracks crossing the entire widths of the slabs. There are relatively many edge-cracks with a length of 100 mm or less. It should be noted that most

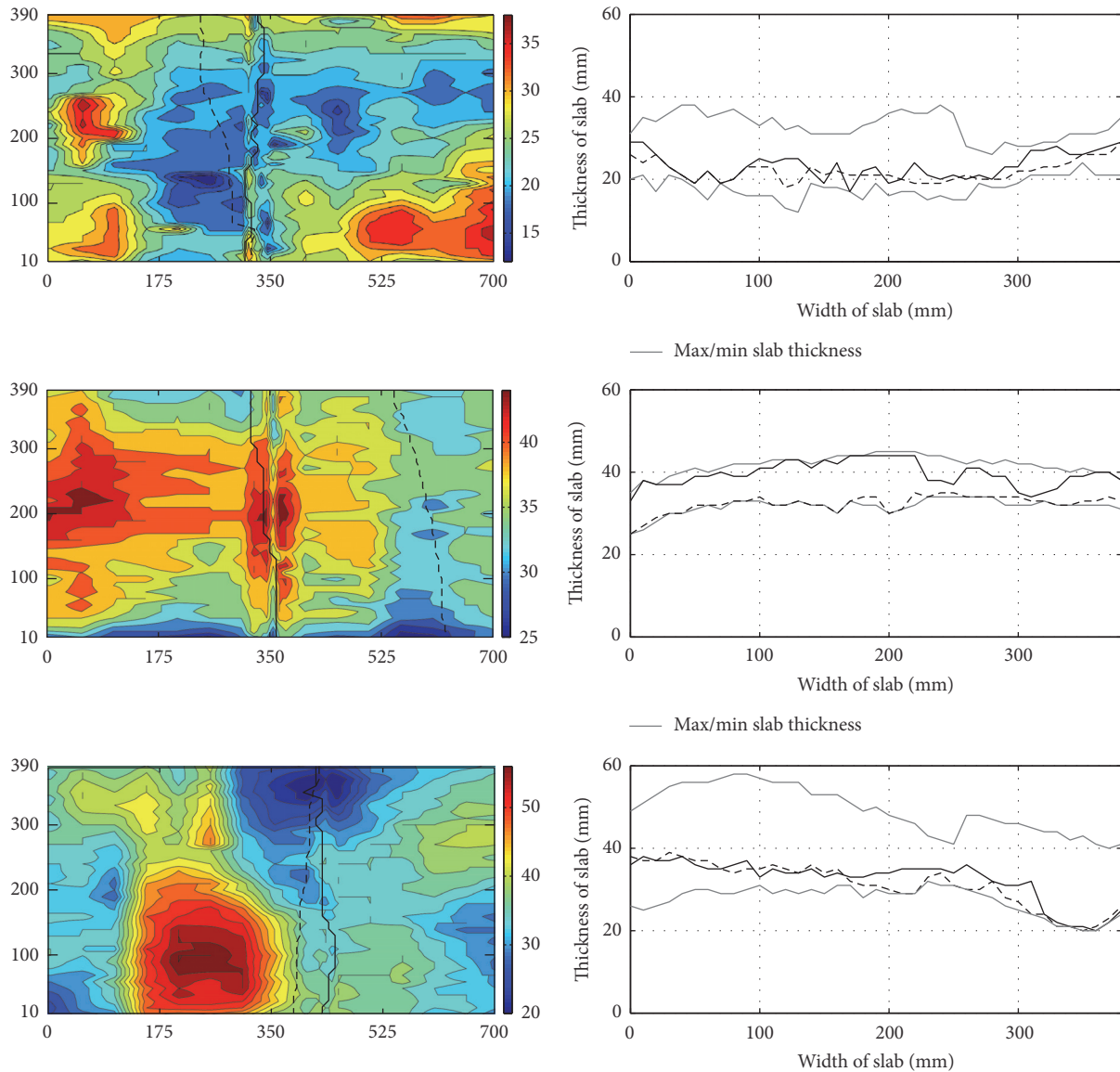


FIGURE 6: Topographical and sectional plots with crack patterns for end-restrained slabs S1, S4, and S5 (top to bottom). Solid lines show experimental results from [15] and dashed lines numerical result. All measurements in (mm).

of the cracks here are surface cracks, due to the bond to the subsurface. This means that the sections of the slabs did not separate as in the end-restrained slabs in the previous case. Also, the development of a macrocrack is here not as distinct as in the previous case, with a more gradual crack opening. Due to this, shrinkage strains up to $2000 \mu\epsilon$ were applied during this analysis in order to find all major cracks that will develop into macrocracks. For the thinnest slab S1, there are multiple edge-cracks that only extend some 50 mm into the slab, as can be clearly seen in the sectional plot (right side) in Figure 7. It is evident that these distributed cracks in an effective way contribute to stress relaxation and prevention of further major cracking. This crack pattern is in good correspondence with observations in situ, as shown in, for example, [8], and during laboratory testing, as shown in [6] and [28]. The shear stresses for a fully restrained slab, or

beam, will be at its maximum around the slab perimeter and the debonding will therefore start from the outer edges of the bonded area and move towards the centre. The slab S4 also shows edge-cracks, which are, however, longer and only at the centre section. A comparison with the results in Figure 6 shows a crack from testing in the same position but with the crack from the corresponding numerical analysis further to the right and over a thinner section of the slab. As previously discussed, the different behaviour of slab S4 may be due to differences in material properties. The best example of crack distribution is here demonstrated by the relatively thick slab S5, with edge-cracks, one crack crossing over the entire width, and also with cracks along the length of the slab. Indications of the latter can also be seen on slab S1, but not on S4. For slab S5, it should specially be noted how the crack pattern distributes around areas with larger thickness.

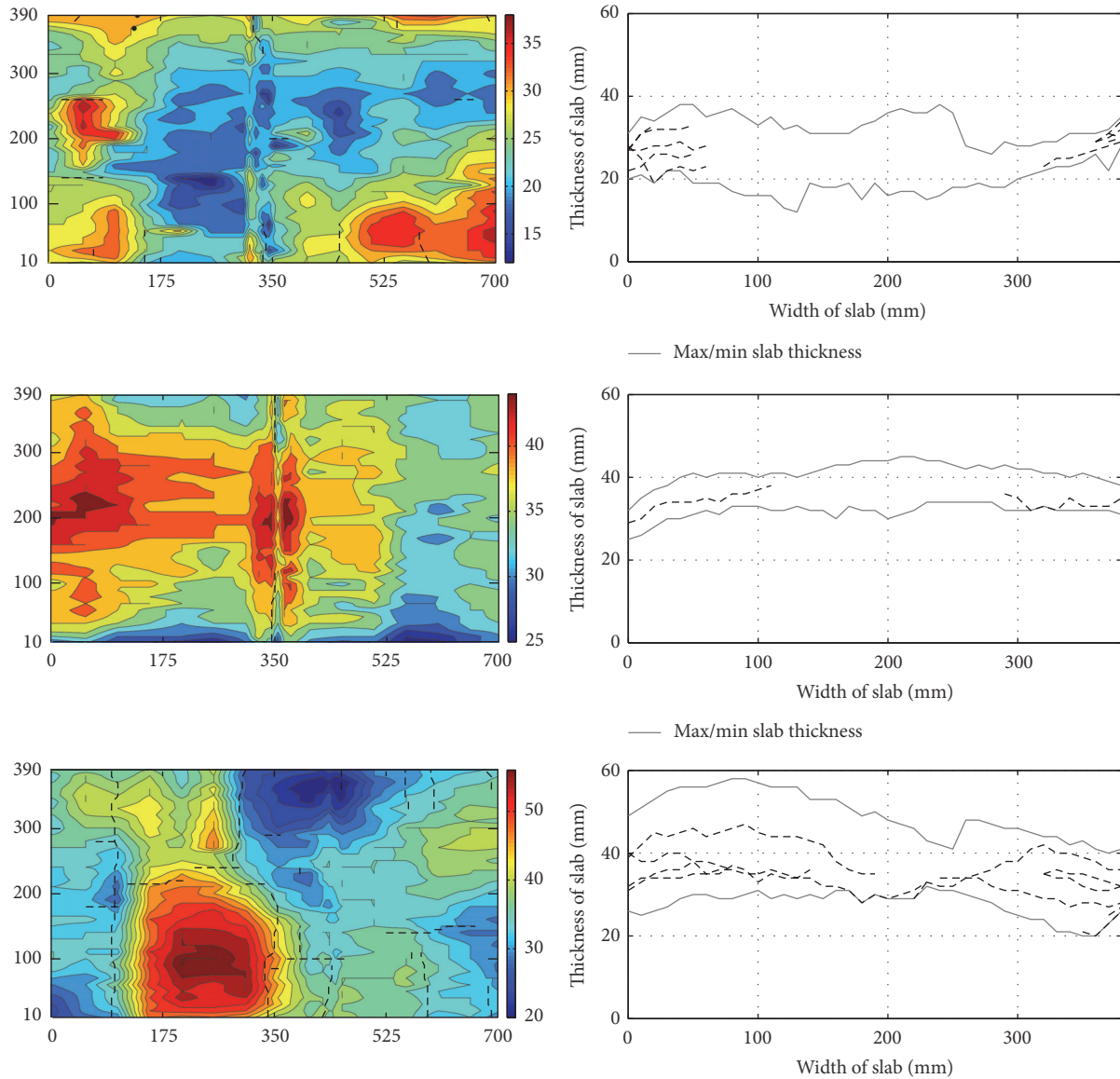


FIGURE 7: Topographical and sectional plots with crack patterns from numerical analysis of fully bond-restrained slabs S1, S4, and S5 (top to bottom). All measurements in (mm).

5. Conclusions

A numerical analysis strategy based on the finite element (FE) method has been presented and demonstrated through examples and comparisons to be suitable for describing restrained shrinkage cracking in shotcrete slabs. The analytical model can describe the difference in structural behaviour between the two structural systems constituted by shotcrete fully bonded to rock and with end restraints only, the latter being represented by shotcrete covered soft drains. Of importance is that the irregular shape and varying thickness of a shotcrete lining can be accurately described, so a small mesh size must therefore be used in the FE analyses.

The stress build-up and resulting crack patterns from the analysis model have been compared with laboratory results from testing of shrinking shotcrete. For the evaluation of the

model behaviour, also results from tests with smaller scale cast concrete beams were used. Primarily, the appearance of shrinkage crack and crack patterns were studied and compared. The presented examples demonstrated that an end-restrained slab is prone to shrinkage induced cracking and will show one large crack due to absence of other restraints, while a fully restrained slab, bonding to the subsurface, will show multiple thinner cracks. This confirms previous experimental results and shows that the model therefore can be used in the design process of shotcrete linings to find critical sections with respect to thickness variations. It was here demonstrated that the topography and distribution of shotcrete thickness are the most important parameters for the formation of shrinkage cracks. Variation in bond strength and the appearance of sections with partial debonding also influence the result, which here also was demonstrated

through comparison with results from shrinking concrete beams. A small local area of debonding, in an otherwise fully restrained shrinking beam or slab, can lead to formation of large cracks. This highlights the importance of a careful preparation of the rock surface prior to shotcreting to ensure good bond strength and no partial debonding. From a theoretical point of view, this also shows the importance of accurately describing the normal and shear bond strength between shotcrete and rock and how interaction between the two will affect the risk for bond failure.

The comparison between numerical analysis results and test results did not clearly show any evidence of positive effects on shrinkage reduction from glass fibre reinforcement. The previously presented test results did, however, indicate a delay in cracking in some cases which here was accounted for in the comparisons. It is possible that the fibres interact with the effect from the subsurface bond in distributing the cracking over many thinner cracks, which here was the case for a thicker slab with a relatively high amount of glass fibres added. For such a case, shrinkage cracks are to be expected in both main-axis directions over a rectangular shotcrete surface. However, the examples demonstrated that, also for fully restrained slabs, there can be cases with only few and wide cracks, as for slabs with end restraints only.

An interesting topic for further studies is to compare the accuracy in describing crack propagation between different material models. This should also include the variations in material properties as the young shotcrete hardens. Different growth rates for, for example, bond strength and stiffness may redistribute stresses that occur during shrinkage and thus affect possible shrinkage crack initiation. Using a damage criterion that considers interaction between normal and shear stresses will also increase the modelling accuracy, especially in the case of partial debonding. The precision of the modelling technique should be further tested and developed through further comparisons with laboratory and test results.

Conflicts of Interest

The authors declare that they have no conflicts of interest.

Acknowledgments

The work presented in this paper is part of a larger research project focusing on numerical simulations of irregular shotcrete and the interaction between shotcrete and hard rock. The project is sponsored by BeFo, the Rock Engineering Research Foundation, and their support is hereby greatly acknowledged. The authors are also grateful for the collaboration with Dr. Lars Eloff Bryne, who carried out the experimental work addressed in this paper.

References

- [1] J. Holmgren, "Shotcrete research and practice in Sweden a development over 35 years," in *Shotcrete: Elements of a System*, pp. 135–142, CRC Press/Balkema, Sydney, Australia, 2010.
- [2] U. Nilsson, *Structural behaviour of fibre reinforced sprayed concrete anchored in rock [Ph.D. thesis]*, KTH Royal Institute of Technology, Stockholm, Sweden, 2003.
- [3] L. Malmgren and E. Nordlund, "Interaction of shotcrete with rock and rock bolts—A numerical study," *International Journal of Rock Mechanics and Mining Sciences*, vol. 45, no. 4, pp. 538–553, 2008.
- [4] F. Barpi and D. Peila, "Influence of the tunnel shape on shotcrete lining stresses," *Computer-Aided Civil and Infrastructure Engineering*, vol. 27, no. 4, pp. 260–275, 2012.
- [5] L. Malmgren, E. Nordlund, and S. Rolund, "Adhesion strength and shrinkage of shotcrete," *Tunnelling and Underground Space Technology*, vol. 20, no. 1, pp. 33–48, 2005.
- [6] J. Carlswård, *Shrinkage cracking of steel fibre reinforced self compacting concrete overlays: test methods and theoretical modelling [Ph.D. thesis]*, Luleå University of Technology, Luleå, Sweden, 2006.
- [7] P. Groth, *Fibre reinforced concrete [Ph.D. thesis]*, Luleå University of Technology, Luleå, Sweden, 2010.
- [8] A. Ansell, "Investigation of shrinkage cracking in shotcrete on tunnel drains," *Tunnelling and Underground Space Technology*, vol. 25, no. 5, pp. 607–613, 2010.
- [9] L. E. Bryne, *Time dependent material properties of shotcrete for hard rock tunneling [Ph.D. thesis]*, KTH Royal Institute of Technology, Stockholm, Sweden, 2014.
- [10] A. Sjölander, T. Gasch, A. Ansell, and R. Malm, "Shrinkage cracking of thin irregular shotcrete shells using multiphysics models," in *Proceedings of the 9th International Conference on Fracture Mechanics of Concrete and Concrete Structures*, Berkeley, Calif, USA, 2016.
- [11] A. Sjölander, W. Bjureland, and A. Ansell, "On failure probability of thin irregular shotcrete shells," in *Proceedings of ITA-AITES World Tunnel Conference*, Bergen, Norway, June 2017.
- [12] A. Sjölander and A. Ansell, "Analysis of the interaction between rock and shotcrete for tunnel support," in *Proceedings of 23th Nordic Concrete Research Symposium*, Aalborg, Denmark, August 2017.
- [13] B. Lagerblad, L. Fjällberg, and C. Vogt, "Shrinkage and durability of shotcrete," in *Shotcrete: Elements of a System*, pp. 173–180, CRC Press/Balkema, Sydney, Australia, 2010.
- [14] E. S. Bernard, "Early-age load resistance of fibre reinforced shotcrete linings," *Tunnelling and Underground Space Technology*, vol. 23, no. 4, pp. 451–460, 2008.
- [15] L. E. Bryne, A. Ansell, and J. Holmgren, "Shrinkage testing of end-restrained shotcrete on granite slabs," *Magazine of Concrete Research*, vol. 66, no. 17, pp. 859–869, 2014.
- [16] L. Ahmed, *Models for analysis of young cast and sprayed concrete subjected to impact-type loads [Ph.D. thesis]*, KTH Royal Institute of Technology, Stockholm, Sweden, 2015.
- [17] L. E. Bryne, A. Ansell, and J. Holmgren, "Laboratory testing of early age bond strength of shotcrete on hard rock," *Tunnelling and Underground Space Technology*, vol. 41, no. 1, pp. 113–119, 2014.
- [18] R. Jansson, *Fire spalling of concrete: theoretical and experimental studies [Ph.D. thesis]*, KTH Royal Institute of Technology, Stockholm, Sweden, 2013.
- [19] J. M. L. Reis and A. J. M. Ferreira, "Assessment of fracture properties of epoxy polymer concrete reinforced with short carbon and glass fibers," *Construction and Building Materials*, vol. 18, no. 7, pp. 523–528, 2004.

- [20] J. M. L. Reis, "Fracture and flexural characterization of natural fiber-reinforced polymer concrete," *Construction and Building Materials*, vol. 20, no. 9, pp. 673–678, 2006.
- [21] I. Merta and E. K. Tschegg, "Fracture energy of natural fibre reinforced concrete," *Construction and Building Materials*, vol. 40, pp. 991–997, 2013.
- [22] M. T. Kazemi, F. Fazileh, and M. A. Ebrahimezhad, "Cohesive crack model and fracture energy of steel-fiber-reinforced-concrete notched cylindrical specimens," *Journal of Materials in Civil Engineering*, vol. 19, no. 10, pp. 884–890, 2007.
- [23] CEN, *En 1488-3: Testing Sprayed Concrete Part 3: Flexural Strengths (First Peak, Ultimate and Residual) of Fibre Reinforced Beam Specimens*, European Committee for Standardization, Brussels, Belgium, 2015.
- [24] A. Hillerborg, M. Modéer, and P.-E. Petersson, "Analysis of crack formation and crack growth in concrete by means of fracture mechanics and finite elements," *Cement and Concrete Research*, vol. 6, no. 6, pp. 773–781, 1976.
- [25] Fib, *Fib Model Code for Concrete Structures 2010*, Wiley-VCH, Weinheim, Germany, 2013.
- [26] Simulia, *Abaqus 6.14 Online Documentation*, Dassault Systeme, 2014.
- [27] Altair, *Hyper Works 13.0*, Altair, 2014.
- [28] J. Silfwerbrand, "Shear bond strength in repaired concrete structures," *Materials and Structures*, vol. 36, no. 260, pp. 419–424, 2003.
- [29] T. Hahn, "Bond strength of shotcrete against various rock surfaces," Tech. Rep. 55:1/83, BeFo, Stockholm, Sweden, 1983.
- [30] D. Saiang, L. Malmgren, and E. Nordlund, "Laboratory tests on shotcrete-rock joints in direct shear, tension and compression," *Rock Mechanics and Rock Engineering*, vol. 38, no. 4, pp. 275–297, 2005.
- [31] T. Ellison, "Bond strength testing at Södra länken Stockholm," Tech. Rep., Besab, Gothenburg, Sweden, 2010.
- [32] Z. A. Moradian, G. Ballivy, and P. Rivard, "Application of acoustic emission for monitoring shear behavior of bonded concrete-rock joints under direct shear test," *Canadian Journal of Civil Engineering*, vol. 39, no. 8, pp. 887–896, 2012.

Research Article

Influence of Crumb-Rubber in the Mechanical Response of Modified Portland Cement Concrete

J. Retama¹ and A. G. Ayala²

¹Department of Civil Engineering, FES Aragón, National Autonomous University of Mexico, 57130 Nezahualcoyotl, MEX, Mexico

²Department of Structural Engineering, Institute of Engineering, National Autonomous University of Mexico, Coyoacán, 04510 Mexico City, Mexico

Correspondence should be addressed to J. Retama; jretamav@comunidad.unam.mx

Received 10 February 2017; Accepted 3 April 2017; Published 2 May 2017

Academic Editor: Peng Zhang

Copyright © 2017 J. Retama and A. G. Ayala. This is an open access article distributed under the Creative Commons Attribution License, which permits unrestricted use, distribution, and reproduction in any medium, provided the original work is properly cited.

The influence of crumb-rubber on the mechanical properties of Portland cement concrete (PCC) is studied by experimental tests and numerical simulations. The main hypothesis of the study is that replacing part of the stone aggregate with crumb-rubber in the mix modifies the energy dissipation during the cracking process and affects the concrete behaviour under monotonically increasing loads. The experimental research program characterizes the mechanical properties of PCC for three different types of concrete with a variable content of crumb-rubber. The experimental results showed that fracture energy and other properties are directly related to the rubber fineness used in the mixture. The material properties derived for these laboratory tests are used to study, by numerical models, its response through its damage evolution. The numerical model used to simulate the damage evolution of the concrete is the Embedded Discontinuity Method (EDM). One characteristic of the EDM is that it does not need to modify the mesh topology to propagate the damage through the continuum solid. For this study, the Disk-Shaped Compact Tension specimen geometry, normed by the D7313-13 of the ASTM, is used. Results showed that the numerical methods provide good approximation of the experimental curve in the elastic and softening branches.

1. Introduction

Even though concrete is the most common material used in infrastructure construction, like roads, it does not always fulfil requirements like low weight, high strength, and ductility, under working-load conditions. Numerous studies have been conducted to improve the mechanical properties of concrete by replacing part of the aggregate with rubber obtained from discarded tires [1].

1.1. Experimental Studies. Compared with the use of crumb-rubber in asphalt paving mixtures, its use in PCC material is limited [2, 3].

During the last two decades, studies have investigated possible uses of crumb-rubber from scrap tires [4–6]. One of the most promising applications is the use of such waste, in creating PCC roads [4, 7, 8]. To conduct this process, the tires must be crushed in the form of chips or powder to be incorporated into the concrete.

Khatib and Bayomy [9] performed experimental tests using fine and coarse rubber as stone aggregate replacement in a concrete mix and reported that the rubberized PCC mixes can be fabricated and exhibit workability up to a certain degree, where the maximum rubber replacement content tested was 57% of the total aggregate volume. Following the same idea, Huang et al. [2] subjected rubberized concrete specimens to uniaxial compression loads; their results showed that this type of concrete exhibits a high toughness. However, the strength decreases significantly when the rubber content increases. With the intention of analysing this phenomenon, Ghaly and Cahill [10] replaced 5%, 10%, and 15% of tire rubber per concrete volume and showed that there is a reduction in the compressive strength in the concrete with a higher rubber content and that, in all cases, the strength of the conventional concrete was superior.

To attenuate the effects of this issue, Papakonstantinou and Tobolski [11] added tire rubber, including the steel cords,

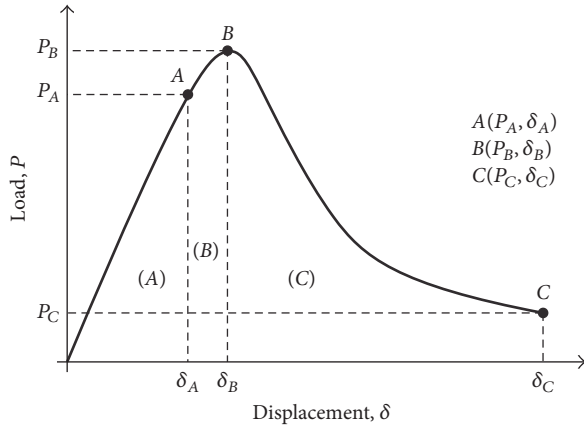


FIGURE 1: Typical load-displacement curve [17].

to the preparation of concrete mixes. Their experimental results showed that, despite a reduction in compressive strength, the toughness increased when the steel reinforcement was included. Using the same approach and greater rubber volumes, Khaloo et al. [12] fabricated rubberized concrete test specimens at percentages of 12.5%, 25%, 37.5%, and 50% and subjected them to uniaxial compression tests with controlled deformation, which exhibited significant reductions in the strength and elasticity modulus and an important reduction in the concrete brittle behaviour when the rubber content was increased.

These researchers and others [13–15] studied the energy dissipation in concrete by means of the three points' beam geometry. In the present research work the Disk-Shaped Compact Tension test normed by the ASTM D7313-13 standard [16] is adopted to evaluate the fracture energy of concrete mixes.

1.2. Numerical Studies. In addition to the evaluation of the mechanical properties previously described, understanding the fracture process of rubberized concrete is essential. During the fracture evolution in concrete, there is a release of energy [18, 19]. Behaviour like that shown in Figure 1 [17] is typical for quasi-brittle materials like concrete.

Due to the nature of rubber, bonding between this and cement paste is weak, resulting in a reduction of compressive and tensile strength of PCC [1, 2, 20] but an improvement in its ductility in the postyielding behaviour [21].

The idea of modelling the damage process in quasi-brittle materials by lumping strain concentration along a crack has motivated the development of formulations of finite elements with embedded discontinuities and their applications to quasi-static problems. This type of finite elements provides a realistic and direct way to implement constitutive models of cohesive cracks in a continuum setting. Following the pioneering work of Ortiz et al. [22] and Belytschko et al. [23] many related formulations have been published [24–28].

The formulation of these elements implies two requirements in the crack zone which must be satisfied: (1) equilibrium (traction continuity across crack surfaces) and (2)

TABLE 1: Concrete mix design.

Material	Dosage (kg/m ³)		
	CFR	CCR	PCC
Portland cement	350	350	350
River sand	770.2	790	790
Crushed basalt	1000	975	1000
Crushed rubber	19.8	25	0
Water	205	205	205

kinematics (rigid body motions of the two parts in which the element is divided by a crack) [29].

The application of the Embedded Discontinuity Method (EDM) to study the damage in solids covers different types of materials. In the context of asphalt concrete, in 2005, Wagoner et al. [30] used an intrinsic cohesive zone model, in which the bulk of the material was discretized with linear elastic finite elements, whereas the crack zone was modelled with cohesive interface elements. The constitutive behaviour of the material of these interface elements was considered using a bilinear softening law. In 2009 Wu et al. [31] applied the EDM to accurately reproduce the fracture behaviour of a Disk-Shaped Compact Tension test. These authors used the model proposed by Sancho et al. [32] which was implemented through the finite element method (FEM) into the open source software OpenSees [33].

In the present paper, the capabilities of the EDM are shown for modelling the damage process in disk-shaped compact specimens, built of concrete mixtures with different amounts of tire rubber aggregate, based in the EDM formulated by Retama and Ayala [28].

2. Materials and Experimental Program

For this study, three types of concrete were studied: concrete with fine crumb-rubber (CFR), concrete with coarse crumb-rubber (CCR), and, as comparison material, Portland cement concrete (PCC), without crumb-rubber.

2.1. Concrete Mix Design. To fabricate the concrete mix, conventional Portland cement combined with a coarse aggregate (crushed basalt rock) with a maximum size of 20 mm and fine aggregate (river sand) with a maximum diameter of 5 mm was used.

The crumb-rubber was incorporated into the concrete mix to replace the stone aggregate (fine or coarse depending on the case) in a proportion of 2.5% per weight. The mix proportions for the three types of concrete are shown in Table 1.

2.2. Fabrication of Specimens. A total of 30 concrete cylinders with diameters of 15 cm and heights of 15 cm (10 cylinders for each type of concrete) were cut with a saw to obtain the Disk-Compact Tension test (DCT). In Figure 2 the geometry of the specimens standardized by the ASTM D7313-13 standard can be seen [16].

Characteristic dimensions of the specimen are shown in Figure 2, and their numerical values are as follows:

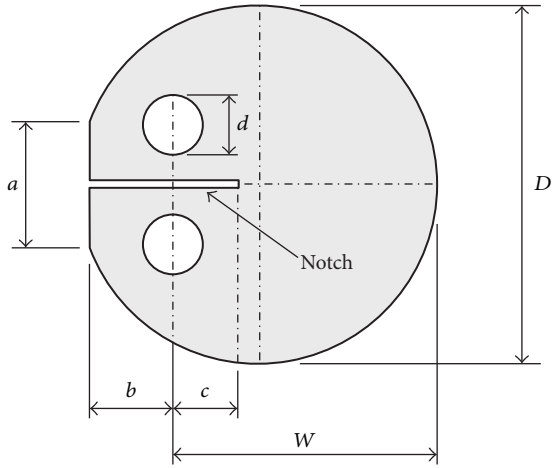


FIGURE 2: DCT specimen geometry.



FIGURE 3: Specimen mounted in the machine test.

- (i) $D = 150$ mm
- (ii) $d = 25$ mm
- (iii) $a = 50$ mm
- (iv) $b = 35$ mm
- (v) $c = 27.50$ mm
- (vi) $W = 110$ mm
- (vii) depth = 5 mm.

A total of 10 specimens were tested for each concrete, that is, concrete with fine crumb-rubber, concrete with coarse crumb-rubber, and concrete without crumb-rubber.

2.3. Test Method. During the DCT test, a servohydraulic press was used to apply the load along with a pair of LVDTs to measure the specimen crack mouth opening displacement (CMOD); see Figure 3. The LVDTs were positioned on both lateral faces of the specimen to obtain an average of the aperture. At the beginning of the test, a preload of 0.2 kN was applied, and subsequently, a controlled displacement of 0.0017 mm/s was applied until failure.

The execution speed of the test was ten times slower than that specified by the ASTM D7313 standard (0.017 mm/s) because, in contrast with an asphalt mix, concrete exhibits a

brittle failure, which makes it difficult to collect information from a load—CMOD curve at a fast speed. Several additional tests were performed at a speed of 0.00017 mm/s (one hundred times slower than that specified in the ASTM D7313 standard). The results obtained were unsatisfactory because an elastic recovery phenomenon occurred in the concrete. All specimens were tested at $10^\circ\text{C} \pm 0.2^\circ\text{C}$.

3. Embedded Discontinuity Method

The EDM addressed in this paper, for modelling the kinematic behaviour of a finite element crossed by a cohesive crack, that is, crack line in which all damage process zone is lumped and characterized in the form of a traction–displacement law which exhibits softening, corresponds to that developed by Retama and Ayala [28].

In this method, the two parts in which a finite element is divided by a cohesive crack, referred to in this paper as a discontinuity, are assumed to undergo rigid body motions with respect to the kinematics of the discontinuity as it is shown in Figure 4.

To illustrate the method, Figure 4 shows a triangular finite element divided into two parts, V^- and V^+ , by the discontinuity S_d , defined by its normal vector \mathbf{n} pointing towards V^+ , and the relative displacements between both subdomains are given by the displacements jump vector $[[\mathbf{u}]] = ([[u]]_n, [[u]]_s)^T$.

The standard kinematics of the finite element is enriched at elemental level, by introducing an internal node where displacements jump $[[\mathbf{u}]]$ is defined as a constant function. According to this, the element displacement field is decomposed into elastic, \mathbf{u}^e , and cracking, \mathbf{u}^c , parts

$$\mathbf{u} = \mathbf{u}^e + \mathbf{u}^c. \quad (1)$$

The elastic displacement part is a smooth function defined in the element domain V as

$$\mathbf{u}^e = \mathbf{N}\mathbf{d}. \quad (2)$$

In (2), matrix \mathbf{N} contains the standard shape functions used to interpolate the element nodal displacements \mathbf{d} [34]. In the same way, cracking displacements are interpolated in the finite element framework by means of

$$\mathbf{u}^c = \mathbf{N}_c [[\mathbf{u}]], \quad (3)$$

with \mathbf{N}_c being a shape functions matrix associated with nodes located in V^+ (see Figure 4) and the already defined displacement jump vector $[[\mathbf{u}]]$, both defined at elemental internal node. For the case of the node numbering of the triangle shown in Figure 4, the matrix \mathbf{N}_c is defined as

$$\mathbf{N}_c = \sum_{i=1}^{n^+} N_i^+ = \mathbf{N}_3, \quad (4)$$

where n^+ denotes the number of nodes belonging to the subdomain V^+ . For a detailed description of the EDM, the reader is referred to the work of Retama [27].

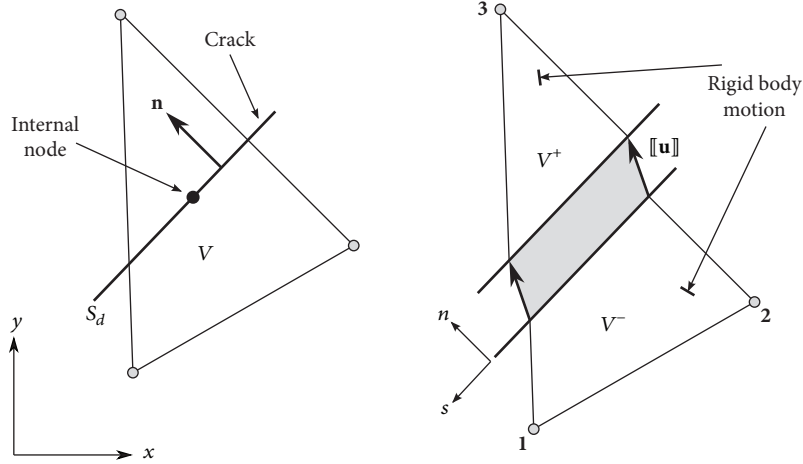


FIGURE 4: Finite element with internal crack.

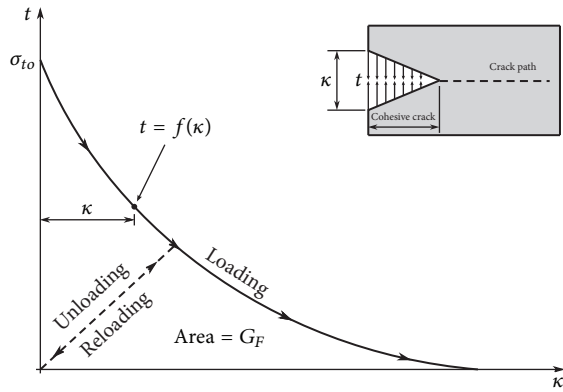


FIGURE 5: Cohesive crack model.

3.1. Cohesive Damage Model. For modelling the evolution of material damage where mode-I type failure is dominant, altogether with the EDM, a cohesive crack type model is used [18, 35, 36]. The effects of microcracks and plastic flow around a macroscopic crack tip are introduced as equivalent tractions along the crack faces, as it is shown in Figure 5. This cohesive crack model was introduced by Barenblatt [37] and Dugdale [38] for modelling cracks in materials such as ceramics, polymers, and metals and extended to concrete by Hillerborg et al. [36].

In this model, the inelastic response is governed by two key material parameters: tensile strength, σ_{to} , and fracture energy, G_F , Figure 5. A discontinuity is introduced when the principal stress σ_I exceeds the tensile strength of the material, like the Rankine criterion in classical plasticity theory, which is a mode-I of failure criterion commonly used for quasi-brittle materials [39, 40].

Following the work of Retama and Ayala [27, 28], the function f which describes the load state in the crack zone, loading/unloading conditions, is given as

$$f = \langle \llbracket u \rrbracket_{eq} - \kappa \leq 0 \rangle, \quad (5)$$

where $\llbracket u \rrbracket_{eq}$ is an equivalent jump obtained from the displacement jump vector $\llbracket u \rrbracket$. The symbol $\langle \cdot \rangle$ represents the Macaulay brackets, denoting that only the positive part of the normal displacement jump is considered, and κ is a scalar internal variable, equal to the largest value of $\langle \llbracket u \rrbracket_{eq} \rangle$, defined as

$$\kappa = \kappa \llbracket u \rrbracket = \max \langle \llbracket u \rrbracket_{eq} \rangle. \quad (6)$$

Tractions on the discontinuity surface are functions of the normal displacement jump, through κ . These are derived from the classical softening curve, Figure 5, by means of the exponential function

$$t_n = \sigma_{to} e^{-(\sigma_{to}/G_F)\kappa}. \quad (7)$$

This equation implies that the residual traction has the same direction as the jump displacement, that is, monotonic loading state. Furthermore, (7) considers that the energy dissipation in the damage process is consistent with the physical phenomena, since

$$G_F = \int_0^{\infty} t_n d\kappa. \quad (8)$$

To complete the constitutive relation for the material in the crack zone, it is necessary to define the tangent constitutive tensor \mathbf{T} . This is derived from (8) as

$$\mathbf{T} = \frac{\partial t}{\partial \kappa} = -\frac{\sigma_{to}^2}{G_F} e^{-(\sigma_{to}/G_F)\kappa}. \quad (9)$$

4. Numerical Simulation

The aim of this section is to show the ability of the EDM to reproduce experimental results under quasi-static loading conditions, showing its numerical and theoretical consistency. Since no shear stresses are allowed along the crack, damage is simulated considering only the mode-I of failure.

The EDM, presented in Section 3, was implemented in the FEAP program. Taking advantage of the enriched element

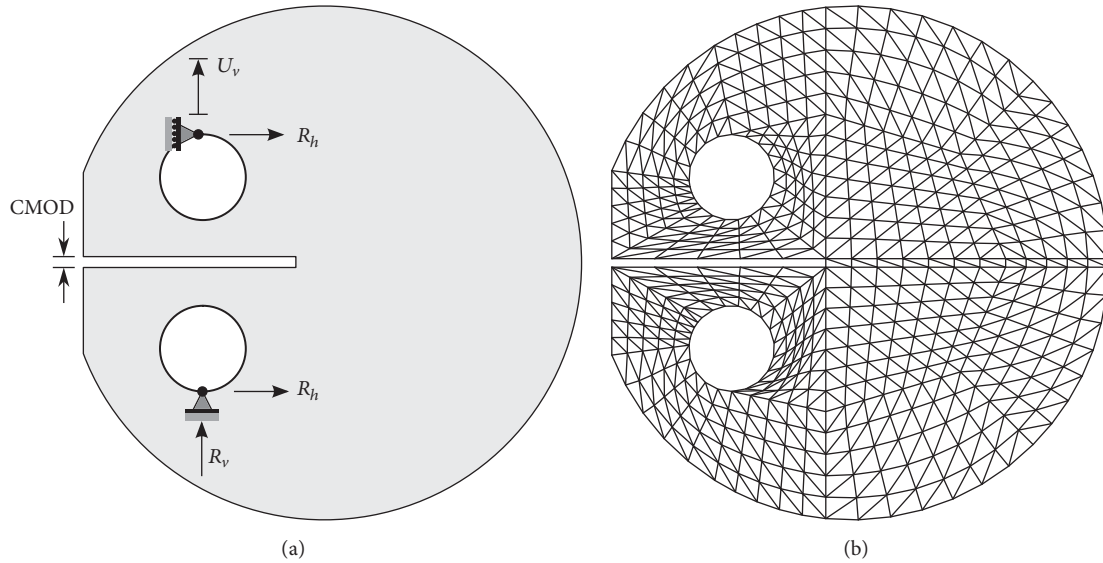


FIGURE 6: Finite element model, (a) supports, and (b) mesh.

used to incorporate the crack into the element domain, static condensation of the additional degrees of freedom (dof) was used to preserve those regular in a standard finite element formulation [27, 41].

4.1. Geometry. The specimen geometry used corresponds to that described in Section 2.2 for the experimental test, following recommendations of the ASTM D7313 standard; see Figure 2.

The geometry of the specimen includes a notch symmetrically located between the two holes where displacements are imposed. This notch is to guarantee that damage initiates at its tip and the plastic zone around is minimum.

4.2. Finite Element Model. To simulate the test conditions of the specimen, a plane stress state was considered. The used supports are shown in Figure 6(a). In the lower support, zero horizontal and vertical displacements were considered, whereas in the upper one, zero horizontal displacement was imposed and in the vertical direction, an incremental displacement control was applied. The finite element mesh used, shown in Figure 6(b), consisted of constant strain triangles with embedded discontinuities.

Elastic and fracture energy properties, used in the numerical simulation, are given in Sections 5.1 and 5.2.

5. Results and Discussions

This section presents results derived from the experimental and numerical studies, for the three concrete mixes, pointing out in the curve load versus CMOD and the energy dissipation in the damage evolution process.

5.1. Elastic Properties. Additional specimen to those used to obtain the fracture energy were tested according to the ASTM standards: for elastic modulus, C469 [42], compressive

strength, C39 [43], and tensile strength, C496 [44]. The results are shown in Table 2.

The average properties taken for the numerical simulation, described in Section 4, are those reports in Table 2, and the Poisson ration is equal to $\nu = 0.20$, for the three types of concrete.

It is observed that the size of crumb-rubber modifies the elastic properties of the concrete. The elastic modulus of concrete CCR is less than those for CFR and PCC; this means that the material undergoes more deformation before the yield strength is reached, that is, increasing the ductility of the material, but its tensile strength is reduced in 16.7% with respect to PCC.

This behaviour of CFR is attributed to the capability of crumb-rubber to deform and its lack of adherence with the cement past.

5.2. Fracture Energy. Results of experimental tests for the three concrete mixes are reported in this section. The measured fracture energy is associated with the mode-I of failure, dominant in this series of tests. Curves of load versus CMOD for CFR, CCR, and PCC concrete are shown in Figures 7, 8, and 9, respectively.

Values of peak load, maximum CMOD, and fracture energy for the ten specimens, for each concrete type, are shown in Tables 3–5.

Comparing results of specimens with the two crumb-rubber sizes, we may observe reductions in the maximum load peak and CMOD for the concrete CFR, which is reflected in a reduced total fracture energy value; that is, the fine rubber creates more imperfections in the concrete that increases its brittleness. In the concrete with coarse rubber, imperfections occur but to a lesser extent because rubber is less dispersed throughout the mix.

5.3. Numerical versus Experimental Results. In this section the results obtained from the numerical simulation are

TABLE 2: Elastic properties.

Specimen	Compressive strength		Tensile strength		Elastic modulus	
	MPa	Std. dev.	MPa	Std. dev.	GPa	Std. dev.
CFR	24.51	4.21	3.23	2.45	20.51	0.50
CCR	24.90	4.89	2.94	3.62	19.99	0.59
PCC	25.06	3.14	3.53	2.58	26.50	0.61

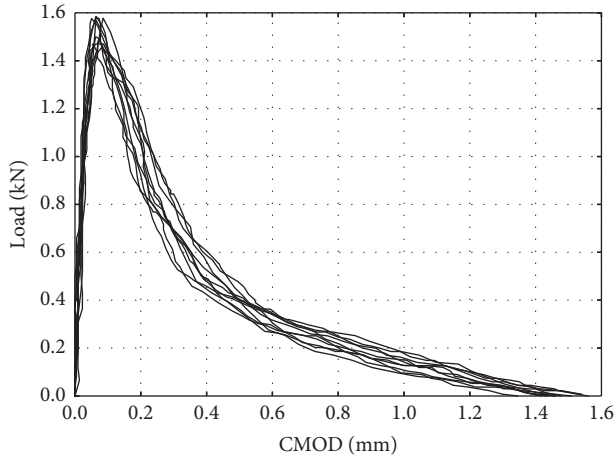


FIGURE 7: Fracture energy for CFR.

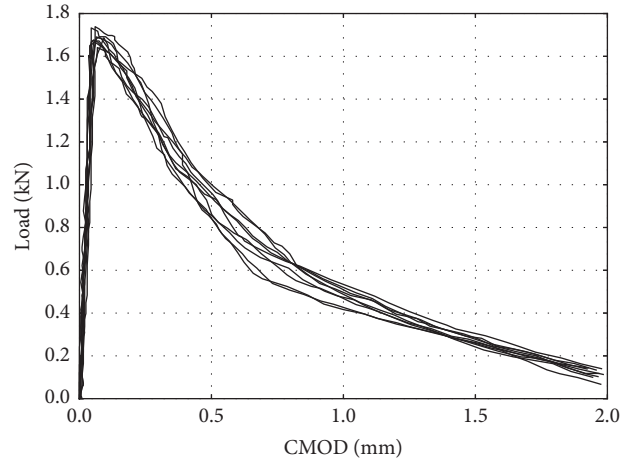


FIGURE 9: Fracture energy for PCC.

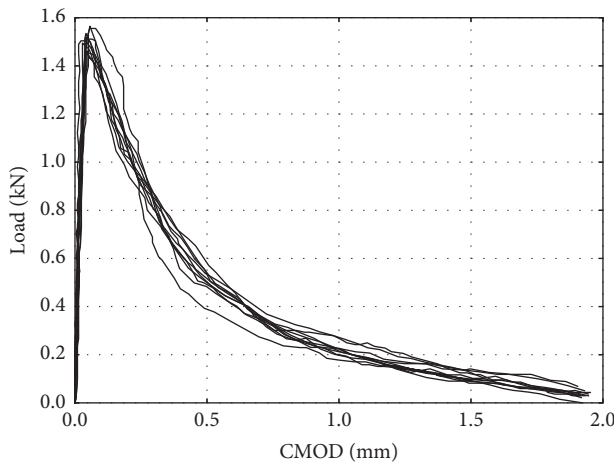


FIGURE 8: Fracture energy for CCR.

TABLE 3: Fracture energy for specimens of CFR.

Specimen	P_L (kN)	$CMOD_{max}$ (mm)	G_F (N/m)
CFR-1	1.470	1.459	151.943
CFR-2	1.455	1.477	143.380
CFR-3	1.576	1.558	153.387
CFR-4	1.585	1.417	135.700
CFR-5	1.470	1.531	124.708
CFR-6	1.577	1.509	133.638
CFR-7	1.555	1.490	136.615
CFR-8	1.577	1.418	130.827
CFR-9	1.500	1.472	129.524
CFR-10	1.492	1.540	142.878
Avg.	1.526	1.487	138.260
Std. dev.	0.052	0.048	9.483

compared with those obtained from experimental tests, pointing out in the characteristics of the softening curve for each concrete mix.

Once the damage propagates, as is shown in Figure 10, the crack divides the solid in two parts. This phenomenon is shown in Figure 10(b) in which both subdomains unload elastically without energy dissipation.

The numerical responses represented by the load versus CMOD curves for the three types of materials, that is, CFR, CCR, and PCC, are shown in Figures 11–13, respectively. In these curves, the experimental data are plotted within the

grey areas, while those obtained with the EDM are plotted as a dark continuous curve.

From these curves, it is observed that the ascending branch, for all three materials, is well reproduced by the numerical simulation, that is, Embedded Discontinuity Method. Regarding the softening branch, the best numerical approximation to the experimental data is for the concrete without crumb-rubber PCC. This was not the case for the concrete with crumb-rubber, a fact that may be explained by the influence of the high heterogeneity, present in these types of concrete, on a numerical formulation assuming homogeneous material. Nevertheless, as it is observed in

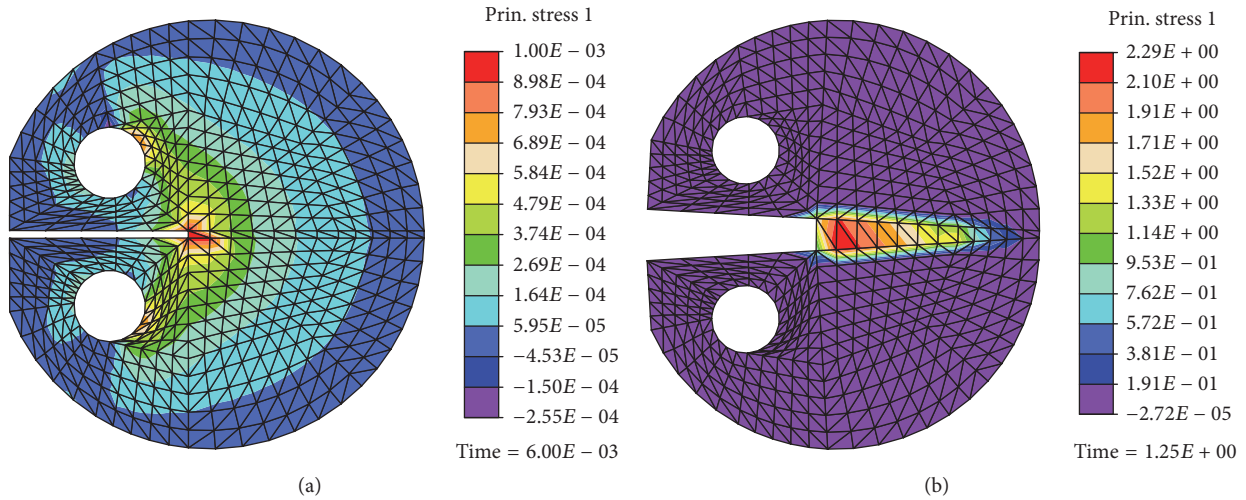


FIGURE 10: Principal stress σ_1 , (a) at the initiation damage, and (b) at a total damage state.

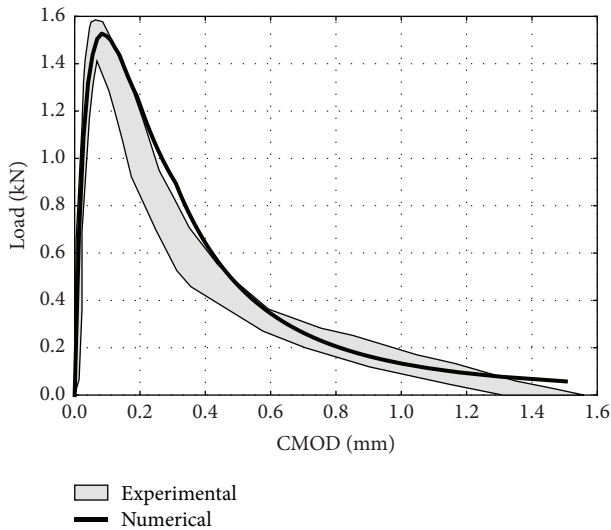


FIGURE 11: CFR concrete.

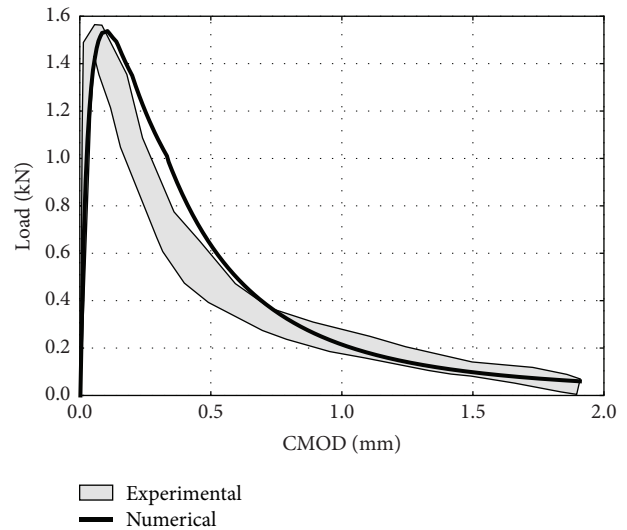


FIGURE 12: CCR concrete.

the softening curve for each modified concrete, the highest difference of the numerical results with the experimental curve corresponds to the concrete CCR, Figure 12.

In general, the difference in numerical and experimental curves may be related to fact that concrete materials, modified or not, are highly heterogeneous and their characterization is difficult.

6. Conclusions

A series of experimental tests for two types of Portland cement concrete, modified with crumb-rubber, and those without crumb-rubber, were conducted to obtain elastic properties and fracture energy for mode-I of failure. Additional numerical studies, based on the Embedded Discontinuity Method, were used to simulate the mechanical behaviour of the material. Some important conclusions may

be addressed in the influence of crumb-rubber and the performance of the presented numerical method.

- (i) The size of the crumb-rubber influences the elastic modulus of the concrete, reducing it for the CFR material and enhancing its ductility.
- (ii) Another effect due to the use of coarse crumb-rubber is that it causes a reduction of 16.7% of the tensile strength.
- (iii) From curves load-CMOD, it may be observed that the concrete with coarse crumb-rubber presents a better behaviour in the softening branch of the curve, since it deforms almost the same as the PCC concrete but with a reduction of the peak load.
- (iv) The difference between results for CFR and CCR may be attributed to the capability of coarse crumb-rubber

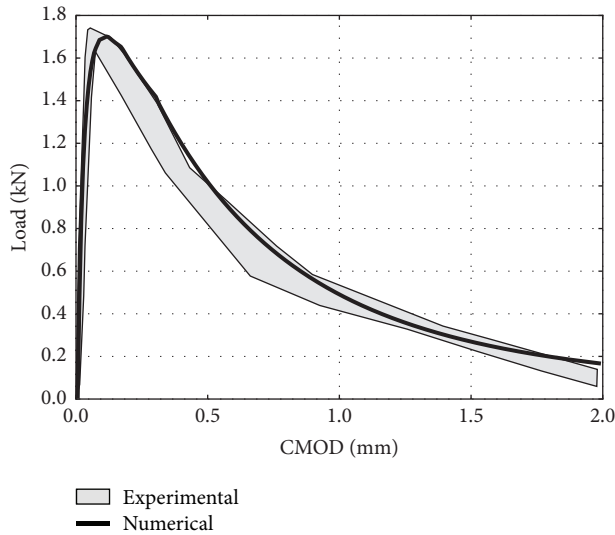


FIGURE 13: PCC concrete.

TABLE 4: Fracture energy for specimens of CCR.

Specimen	P_L (kN)	$CMOD_{max}$ (mm)	G_F (N/m)
CCR-1	1.463	1.923	169.504
CCR-2	1.555	2.045	178.631
CCR-3	1.455	1.991	167.883
CCR-4	1.504	2.050	186.118
CCR-5	1.519	2.032	180.508
CCR-6	1.534	2.077	176.017
CCR-7	1.565	2.072	185.607
CCR-8	1.461	2.067	182.898
CCR-9	1.511	2.063	157.560
CCR-10	1.495	2.007	171.737
Avg.	1.506	2.033	175.646
Std. dev.	0.039	0.048	9.034

TABLE 5: Fracture energy for specimens of PCC.

Specimen	P_L (kN)	$CMOD_{max}$ (mm)	G_F (N/m)
PCC-1	1.641	2.361	299.241
PCC-2	1.861	2.346	291.418
PCC-3	1.691	2.310	299.868
PCC-4	1.666	2.411	305.065
PCC-5	1.672	2.263	303.327
PCC-6	1.687	2.242	289.008
PCC-7	1.677	2.356	316.717
PCC-8	1.733	2.375	282.523
PCC-9	1.738	2.505	292.963
PCC-10	1.687	2.285	290.294
Avg.	1.705	2.345	297.042
Std. dev.	0.062	0.077	9.848

to deform and its lack of adherence with the cement paste.

- (v) With respect to the performance of the numerical method to simulate the damage evolution, it is important to point out that, unlike fracture mechanics, it does not require the medication of the mesh topology to accommodate the crack in the solid, once it propagates.
- (vi) The presented Embedded Discontinuity Method reproduces the experimental curve with a good approximation, as well as the correct dissipation of energy according to the physical phenomena.
- (vii) Other sources of variation of numerical results with those experimental ones may be attributed to the characterization of concrete as a homogenous material.

Conflicts of Interest

The authors of this paper declare that there are no conflicts of interest regarding its publication.

Acknowledgments

This research was developed with the support of the “Dirección de Asuntos del Personal Académico (DGAPA)” of the National Autonomous University of Mexico, through the project Análisis No-Lineal de Vigas con Zonas de Plasticificación y Funciones Spline, PAPIIT TA101317.

References

- [1] I. B. Topçu, “The properties of rubberized concretes,” *Cement and Concrete Research*, vol. 25, no. 2, pp. 304–310, 1995.
- [2] B. Huang, G. Li, S.-S. Pang, and J. Eggers, “Investigation into waste tire rubber-filled concrete,” *Journal of Materials in Civil Engineering*, vol. 16, no. 3, pp. 187–194, 2004.
- [3] X. Shu and B. Huang, “Recycled of waste tire rubber in asphalt and portland cement concrete: an overview,” *Construction and Building Materials*, vol. 67, pp. 217–224, 2014.
- [4] N. N. Eldin and A. B. Senouci, “Use of scrap tires in road construction,” *Journal of Construction Engineering and Management*, vol. 118, no. 3, pp. 561–576, 1992.
- [5] N. N. Eldin and J. A. Piekarski, “Scrap tires: management and economics,” *Journal of Environmental Engineering*, vol. 119, no. 6, pp. 1217–1232, 1993.
- [6] D. H. DeGroot, “Mexico—US cross-border resolution of waste tire disposal,” in *Proceedings of the Worlds Environmental and Water Resources Congress*, 2007.
- [7] M. K. Batayneh, I. Marie, and I. Asi, “Promoting the use of crumb rubber concrete in developing countries,” *Waste Management*, vol. 28, no. 11, pp. 2171–2176, 2008.
- [8] D. Humphrey and M. Blumenthal, “The use of tire-derived aggregated in road construction applications,” in *Proceedings of the Green Streets and Highways Conference*, pp. 299–313, 2010.
- [9] Z. K. Khatib and F. M. Bayomy, “Rubberized Portland cement concrete,” *Journal of Materials in Civil Engineering*, vol. 11, no. 3, pp. 206–213, 1999.

- [10] A. M. Ghaly and J. D. Cahill IV, "Correlation of strength, rubber content, and water to cement ratio in rubberized concrete," *Canadian Journal of Civil Engineering*, vol. 32, no. 6, pp. 1075–1081, 2005.
- [11] C. G. Papakonstantinou and M. J. Tobolski, "Use of waste tire steel beads in Portland cement concrete," *Cement and Concrete Research*, vol. 36, no. 9, pp. 1686–1691, 2006.
- [12] A. R. Khaloo, M. Dehestani, and P. Rahmatabadi, "Mechanical properties of concrete containing a high volume of tire-rubber particles," *Waste Management*, vol. 28, no. 12, pp. 2472–2482, 2008.
- [13] A. Grinys, H. Sivilevičius, D. Pupeikis, and E. Ivanauskas, "Fracture of concrete containing crumb rubber," *Journal of Civil Engineering and Management*, vol. 19, no. 3, pp. 447–455, 2013.
- [14] Y. C. Guo, J. H. Zhang, G. Chen, G. M. Chen, and Z. H. Xie, "Fracture behaviors of a new steel fiber reinforced recycled aggregate concrete with crumb rubber," *Construction and Building Materials*, vol. 53, pp. 32–39, 2014.
- [15] T. Sadowski and D. Pietras, "Description of degradation process of rubberized lean concrete," *Solid State Phenomena*, vol. 216, pp. 67–72, 2014.
- [16] ASTM D7313-13, "Standard test method for determining fracture energy of asphalt aggregate mixtures using the disk-shaped compact tension geometry", American Society for Testing and Materials, 2013.
- [17] S. Ribeiro, E. M. B. Santos, G. C. R. Garcia, and J. A. Rodrigues, "Elastic work and fracture energy of concretes made with crushed stones and pebbles aggregates," *Materials Science Forum*, vol. 636-637, pp. 1215–1221, 2010.
- [18] Z. P. Bazant and J. Planas, *Fracture and size effect in concrete and other quasibrittle materials*, CRC Press, 1997.
- [19] T. L. Anderson, *Fracture mechanics. fundamentals and applications*, CRC Press, 2017.
- [20] D. Lo Presti, "Recycled tyre rubber modified bitumens for road asphalt mixtures: a literature review," *Construction and Building Materials*, vol. 49, pp. 863–881, 2013.
- [21] G. Li, M. A. Stubblefield, G. Garrick, J. Eggers, C. Abadie, and B. Huang, "Development of waste tire modified concrete," *Cement and Concrete Research*, vol. 34, no. 12, pp. 2283–2289, 2004.
- [22] M. Ortiz, Y. Leroy, and A. Needleman, "A finite element method for localized failure analysis," *Computer Methods in Applied Mechanics and Engineering*, vol. 61, no. 2, pp. 189–214, 1987.
- [23] T. Belytschko, J. Fish, and B. E. Engelmann, "A finite element with embedded localization zones," *Computer Methods in Applied Mechanics and Engineering*, vol. 70, no. 1, pp. 59–89, 1988.
- [24] J. C. Simo and M. S. Rifai, "A class of mixed assumed strain methods and the method of incompatible modes," *International Journal for Numerical Methods in Engineering*, vol. 29, no. 8, pp. 1595–1638, 1990.
- [25] J. C. Simo, J. Oliver, and F. Armero, "An analysis of strong discontinuities induced by strain-softening in rate-independent inelastic solids," *Computational Mechanics*, vol. 12, no. 5, pp. 277–296, 1993.
- [26] J. Oliver, "Modelling strong discontinuities in solid mechanics via strain softening constitutive equations. Part I: Fundamentals," *International Journal for Numerical Methods in Engineering*, vol. 39, no. 21, pp. 3575–3600, 1996.
- [27] J. Retama, *Formulation and approximation to problems in solids by embedded discontinuity models*, National Autonomous University of Mexico, Mexico City, Mexico, 2010.
- [28] J. Retama and A. G. Ayala, "Modelado del daño en sólidos mediante formulaciones variacionales y discontinuidades interiores," *Revista Internacional de Métodos Numéricos para Cálculo y Diseño en Ingeniería*, vol. 26, pp. 171–177, 2010.
- [29] M. Jirásek, "Comparative study on finite elements with embedded discontinuities," *Computer Methods in Applied Mechanics and Engineering*, vol. 188, no. 1, pp. 307–330, 2000.
- [30] M. P. Wagoner, W. G. Buttlar, and G. H. Paulino, "Disk-shaped compact tension test for asphalt concrete fracture," *Experimental Mechanics*, vol. 45, no. 3, pp. 270–277, 2005.
- [31] R. Wu, E. Denneman, and J. Harvey, "Evaluation of embedded discontinuity method for finite element analysis of cracking of hot-mix asphalt concrete," *Journal of the Transportation Research Board*, vol. 2127, pp. 82–89, 2009.
- [32] J. M. Sancho, J. Planas, D. A. Cendón, E. Reyes, and J. C. Gálvez, "An embedded crack model for finite element analysis of concrete fracture," *Engineering Fracture Mechanics*, vol. 74, no. 1-2, pp. 75–86, 2007.
- [33] S. Mazzoni, F. McKenna, F. Scott, and G. Fenves, *Open System for Earthquake Engineering Simulation, User Command-Language Manual*, Pacific Earthquake Engineering Research Center, University of California, Berkeley, Calif, USA, 2008.
- [34] O. C. Zienkiewicz, R. L. Taylor, and J. Z. Zhu, "The finite element method. volume I: its basis and fundamentals," *Butterworth—Heinemann*, 2005.
- [35] R. de Borst, M. A. Gutiérrez, G. N. Wells, J. J. C. Remmers, and H. Askes, "Cohesive-zone models, higher-order continuum theories and reliability methods for computational failure analysis," *International Journal for Numerical Methods in Engineering*, vol. 60, no. 1, pp. 289–315, 2004.
- [36] A. Hillerborg, M. Modéer, and P.-E. Petersson, "Analysis of crack formation and crack growth in concrete by means of fracture mechanics and finite elements," *Cement and Concrete Research*, vol. 6, no. 6, pp. 773–781, 1976.
- [37] G. I. Barenblatt, "The Mathematical Theory of Equilibrium Cracks in Brittle Fracture," *Advances in Applied Mechanics*, vol. 7, no. C, pp. 55–129, 1962.
- [38] D. S. Dugdale, "Yielding of steel sheets containing slits," *Journal of the Mechanics and Physics of Solids*, vol. 8, no. 2, pp. 100–104, 1960.
- [39] J. Alfaiate, G. N. Wells, and L. J. Sluys, "On the use of embedded discontinuity elements with crack path continuity for mode-I and mixed-mode fracture," *Engineering Fracture Mechanics*, vol. 69, no. 6, pp. 661–686, 2002.
- [40] G. N. Wells, *Discontinuous modelling of strain localization and failure [Ph.D. thesis]*, Delft University of Technology, Delft, The Netherlands, 2001.
- [41] R. L. Taylor, *FEAP: a finite element analysis program, theory manual*, University of California, Berkeley, Calif, USA, 2008.
- [42] ASTM C469, "Standard test method for static modulus of elasticity and Poisson's ratio of concrete in compression," American Society for Testing and Materials, 2014.
- [43] ASTM C39, "Standard test method for compressive strength of cylindrical concrete specimens," American Society for Testing and Materials, 2014.
- [44] ASTM C496, "Standard test method for splitting tensile strength of cylindrical concrete specimens," American Society for Testing and Materials, 2004.

Research Article

Bond Effects between Concrete and Steel Bar Using Different Diameter Bars and Different Initial Crack Width

Papa Niane Faye,¹ Yinghua Ye,¹ and Bo Diao^{1,2}

¹School of Transportation Science and Engineering, Beihang University, Beijing 100191, China

²State Laboratory of Subtropical Building Science, South China University of Technology, Guangzhou 510640, China

Correspondence should be addressed to Papa Niane Faye; shakurfaye@hotmail.com

Received 4 February 2017; Accepted 16 March 2017; Published 2 April 2017

Academic Editor: Peng Zhang

Copyright © 2017 Papa Niane Faye et al. This is an open access article distributed under the Creative Commons Attribution License, which permits unrestricted use, distribution, and reproduction in any medium, provided the original work is properly cited.

The importance of an accurate simulation of service conditions in the bond performance of reinforced concrete structures in coastal regions is highlighted. Four widths of initial crack of 0, 80, 150, and 210 microns were artificially made by inserting slice into bond specimens during concrete casting. Three bar diameters of 10 mm, 14 mm, and 18 mm were selected. At 28 days, the bond specimens were exposed to the environment of wet-dry cycles of seawater and atmosphere for another 90 days. The pull-out test was then conducted and chloride contents were tested at crack area along 40 mm depth. Results show that, for the specimen with 10 mm bar diameter, cracks width of less than 80 microns vanished rapidly during wet-dry cycles; for other specimens, cracks width of 100–150 microns decreased slightly. However the cracks of width more than 200 microns increased gradually; the chloride content decreased along the depth of concrete, and the chloride content increased as the widths of initial cracks increased or as the bar diameters increased. The ductility of bond specimens decreased as the diameter increased.

1. Introduction

Chloride attack is one of the most severe durability problems for the marine reinforced concrete structures [1]. The chloride penetration of concrete was affected in many ways, including physical, chemical, and mechanical such as permeability, cement binding, and cracking (both internal and external) [2]. The particles penetrate the concrete structures depending on the driving force of the process and the nature of the transported matter, where aggressive medium was transported through concrete by diffusion, absorption, and permeation [3]. It was found that the natural process of chloride ingress in concrete structures takes long time [1]. Under the same service conditions, reinforced concrete flexural members located in marine environments may become unserviceable before becoming unsafe [4]. Corrosion of steel bars embedded in concrete becomes a worldwide problem that affects durability of reinforced concrete structures [5].

In reinforced concrete structures, concrete with fighting against compressive loads plays also the role of protection of the steel bars to the external environment. A good force transfer between the two materials can therefore only be

achieved by an interaction between both materials through bond between the reinforcement bars and the concrete [6]. Such attributes ensure the durability and serviceability of the structure.

The concrete crack can be classified into the following: a crack due to load applied on structures or natural phenomena on its environment. The nonloaded cracks, especially shrinkage cracks, have more important practical significance [7]. Li found that when the crack width is greater than 0.1 mm, the effect of different concrete covers on chloride penetration, and hence the corrosion initiation, is very small [8]. At a crack width of 0.2 mm, the difference between the initiation times as determined by chloride content and inspection is only 6% [9]. Limit of crack width depending on the environment was made by standards and most design codes and standards. However, ACI 318 (ACI Committee 318 1999) and BS 8110 (British Standards 1997) prescribe the maximum permissible crack width to be 0.3 mm for concrete structures [10]. If crack width exceeded 0.3 mm, structures might fail and safety problems might as well start. Failure does not necessarily imply structural collapse but includes loss of serviceability, characterized by cracking, spalling, debonding, and excessive

TABLE 1: Concrete mixture composition (kg/m³).

	Water	Cement	Fly ash	Sand	Aggregate	Water reducer	Air entertainer
Quantity	184	460	53	609	1130	3.94	100.61

deflection [8], so the purpose of design must be fully reflected in the design of specific provisions focused on structural strength and durability [11].

Marine environment contributes to chemical reactions. When carbon dioxide diffuses into concrete in the presence of water, it reacts with calcium hydroxide to form calcium carbonate [3, 12]. Pommersheim and Clifton demonstrated that in seawater degradation mechanisms can be due to the reaction considered involving the replacement of Ca(OH)₂ in concrete by gypsum (CaSO₄·2H₂O), and an expansive process involves the reaction of sulfate ions with calcium aluminates hydrate that gives ettringite (3 CaO · Al₂O₃ · 3 CaSO₄ · 31 H₂O) [13].

A pull-out load was applied to a reinforcement bar embedded in concrete; the resistance which was defined as bond strength between concrete and reinforcement was tested and it was an important factor for RC structures [14]. Using a numerical approach, De Almeida Filho and El Debs explained the load versus slip behavior of the pull-out test [15]. Kabir and Islam affirmed that bond performance of reinforced concrete is important in the study of load transfer mechanism from concrete to inner reinforcing bar and vice versa [16]. On one hand, bond strength was influenced by curing conditions [14], concrete compressive strength [17, 18], concrete cover, embedded length, preflexural crack length, chemical adhesion, and friction [16]. On the other hand, bond strength was influenced by mechanical interlock by ribs and diameter of reinforcement bars [19, 20]. The bond strength was specifically expressed as the function of the applied load, bars diameter, and embedded length [21]. Ductility is the ability of the structure to absorb large energy and produce certain deformation without destroying under a shock or vibration load [22]. The relationship among bonds between concrete and steel bars, durability, and chloride penetration rate are nowadays structural engineering challenges.

The combined effects of initial crack width, diameter of steel bar and environments on the bond strength, and distribution of chloride ion were experimentally investigated. Three diameters of steel bars, four initial crack widths, and two types of environments were selected. The relationship between different diameters embedded in cracked concrete, chloride permeability, and bond strength between different diameter and different crack width of concrete after 90 days of wet-dry cycles of seawater were studied.

2. Specimens and Test Program

Good performances and high quality of concrete mixtures were designed here. All experiments were conducted in structural laboratory of Beihang University.

2.1. Concrete Composition and Properties. This was a concrete mixture with normal Portland cement P.O.42.5, aggregate

of maximum 10 mm, medium sand 2.6, fly ash, and high performance polycarboxylate super plasticizer (standard) HY801 (water-reducer) admixture. The ratio of water/cement was 0.4, and the air content was 5.7%. The compressive strength of concrete prism with sizes of 100 mm * 100 mm * 300 mm was around 39.3 MPa and tested at the age of 28 d. The concrete mixture composition in kilograms per cubic meter is given in Table 1.

2.2. Specimen Design. The bond specimens between concrete and steel bars for pull-out test were designed with different steel bars of diameter 10 mm, 14 mm, or 18 mm. As shown in Figure 1, a reinforcement bar was embedded centrally into concrete block, and the embedded length was 5 times the diameter, that is, 50 mm, 70 mm, and 90 mm. PVC tubes were used here to ensure that only shear stress appeared between concrete and steel bar on pull-out test.

The chloride ingress in concrete with cracks was experimentally studied by [23]. They used to insert 3 sheets of 0.2 mm, 0.3 mm, and 0.5 mm in the specimen for around 4 hours and then fixed the insertion depth of depths 20 mm, 30 mm, and 50 mm. Prisms of dimension (100 × 100 × 150 mm) were adopted in this experimentation. In order to conform to our research plan based on the crack width control, two models of crack simulations were tried; the first model was similar to Marsavina's model [23]; different plate sheets of thickness of 0.05 mm, 0.1 mm, and 0.2 mm were inserted into half depth of the concrete section; duration time was 4 hours. The second model: plate sheet of thickness 0.05 mm was inserted into the steel bars and duration times were 3 h, 4 h, and 5 h before they were removed, respectively. The initial crack widths were tested 2 days later. During the measurement it was observed that the average crack width gotten from the second method with the same plate sheet and different duration times gives approximately the desired widths of cracks and 4 different classes of crack widths including 0 mm. The result shows that the largest width (around 200 microns) of crack was obtained after 5 h of plate sheet insertion. The crack lengths for two models were the same equal to 100 mm (size of the block) and the depths of cracks which were equal to concrete cover were 45 mm, 43 mm, and 41 mm for 10 mm, 14 mm, and 18 mm diameters of steel bars, respectively. The details of specimens and tested groups are given in Tables 2, 3, and 4.

30 specimens of bond between concrete and steel bars were designed and cast. The 30 bond specimens were divided into three sets on the basis of the diameter of steel bars. Each set of specimens was also divided into four groups based on the width of initial cracks and exposing environments. Four groups of initial cracks width were designed as 0 microns, 80 microns, 150 microns, and 210 microns. Two environments of wet-dry cycles and atmosphere were designed. Each group

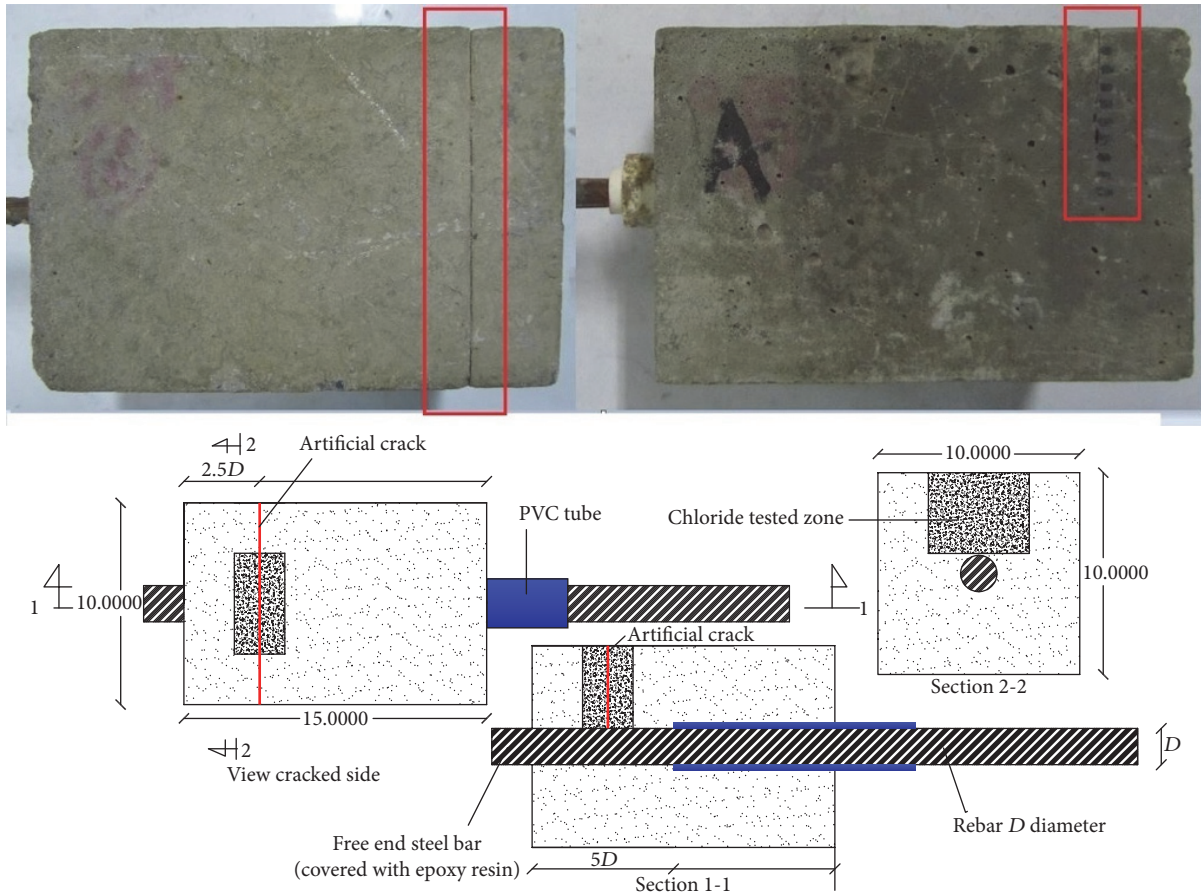


FIGURE 1: Detail of bond specimen for pull-out test crack design and sample design.

TABLE 2: Detailed information of bond specimens with 10 mm diameter bars.

	COD10RE	C0D10WD	C80D10WD	C150D10WD	C210D10WD
Number of specimens	2	2	2	2	2
Design width of crack	0	0	80	150	210
Seawater	No	Yes	Yes	Yes	Yes
Plate sheet insertion time (hours)	0	0	3	4	5

TABLE 3: Detailed information of bond specimens with 14 mm diameter bars.

	COD14RE	C0D14WD	C80D14WD	C150D14WD	C210D14CW
Number of specimens	2	2	2	2	2
Design width of crack	0	0	80	150	210
Seawater	No	Yes	Yes	Yes	Yes
Plate sheet insertion time (hours)	0	0	3	4	5

TABLE 4: Detailed information of bond specimens with 18 mm diameter bars.

	COD18RE	C0D18WD	C80D18WD	C150D18WD	C210D18CW
Number of specimens	2	2	2	2	2
Design width of crack	0	0	80	150	210
Seawater	No	Yes	Yes	Yes	Yes
Plate sheet insertion time (hours)	0	0	3	4	5

TABLE 5: Crack width evolution of specimens with different bar diameters (80 microns).

	C80D10WD2		C80D14WD1		C80D18WD2	
	Point 1	Point 2	Point 1	Point 2	Point 1	Point 2
0	80	80	80	80	70	50
30	50	50	50	50	70	50
60	0	50	30	30	50	0
90	0	20	0	20	50	0

TABLE 6: Crack width evolution of specimens with different bar diameters (150 microns).

Wet-dry cycles	C150D10WD2		C150D14WD2		C150D18WD2	
	Point 1	Point 2	Point 1	Point 2	Point 1	Point 2
0	100	110	140	110	150	150
30	100	110	140	110	130	140
60	100	110	130	100	130	130
90	100	100	130	100	130	130

contained 2 bond specimens. They were exposed in two types of environment, that is, wet-dry cycles of seawater or atmosphere. The seawater was artificially made of 3% NaCl and 0.34% MgSO₄. One of wet-dry cycles includes 8 hours of seawater immersion and 16 hours of atmosphere environment. After 90 cycles of wet-dry and 10 days of atmosphere environment, totally 100 days, the pull-out test was performed.

Tables 2, 3, and 4 give the detailed information of bond specimens sets (five groups), where the specimens are named following this rule. For example, for C0D10RE, C0D14RE, or C0D14WD, the number following C (C0, C80, C160, and C210) was the designed maximum width of initial crack in microns. The number following D (D10, D14, and D18) was the diameter of reinforcement bars. The last two words were the environment of specimen exposing (RE: reference environment (atmosphere), WD: wet-dry cycles of seawater).

2.3. Testing Procedures. All bond specimens were demolded after 24 h of casting and were cured under standard temperature and moisture conditions. At 28 days, except for the six reference specimens (in atmosphere), the remaining 24 bond specimens were exposed to wet-dry cycles environment. After every 30 wet-dry cycles, the crack widths of specimens were measured. Each cycle of wet-dry includes immersion in seawater for 8 h and in atmosphere for 16 h. The alternating rounds of immersion in seawater and in atmosphere environment were repeated till 90 cycles and 10 days of atmospheric environment. The standard pull-out test was conducted on all bond specimens. The pull-out forces, relative slip displacement, and bond strength of every specimen were measured.

After pull-out testing, sample of plate concrete at crack was drilled on the specimen, that is, the chloride tested zone shown in Figure 1. The samples were then subdivided into 5 pieces along the depth of the sample and chloride content was tested on that depth of 25 * 50 * 8 mm³ as shown in Figure 2.



FIGURE 2: Concrete drilled slice (2.5 cm/5 cm/8 mm).

3. Experiment Phenomenon and Results

In this part, four main variables such as the crack evolution, the chloride content, ultimate tensile forces, and ultimate bond strength function with different diameter bars of 10 mm, 14 mm, and 18 mm were experimentally investigated.

3.1. Evolution of Initial Crack on Bond Specimens. After cracks were made on bond specimens, two points on each crack were selected and fixed to measure the crack width during the wet-dry cycles. The values of the two points on each crack width were measured after 0, 30, 60, and 90 wet-dry cycles. Tables 5, 6, and 7 give tested values of crack widths during the wet-dry cycles. All cracks here are artificially made by insertion of plate sheet at the earlier age of the concrete casting.

As shown in Table 5, testing results of two points on the same crack of bond specimens with bar diameters of 10 mm or 14 mm present reduction of crack width after 30 days of wet-dry cycles when the width was smaller than 80 microns. At the same moment, the testing results of specimens showed that crack width of the 18 mm diameter remained the same. The tested points of the crack width on the specimens with bar diameters of 10 mm or 14 mm decreased quickly as cycle number of wet-dry increased. At the same time the crack width of specimens with 18 mm diameter decreased slowly from initial crack width of 70 microns and 50 microns to

TABLE 7: Crack width evolution of specimens with different bar diameters (210 microns).

	C210D10WD1		C210D14WD2		C210D18WD2	
	Point 1	Point 2	Point 1	Point 2	Point 1	Point 2
0	210	230	210	210	210	210
30	230	240	230	230	240	240
60	230	260	240	230	240	260
90	240	260	240	240	260	270

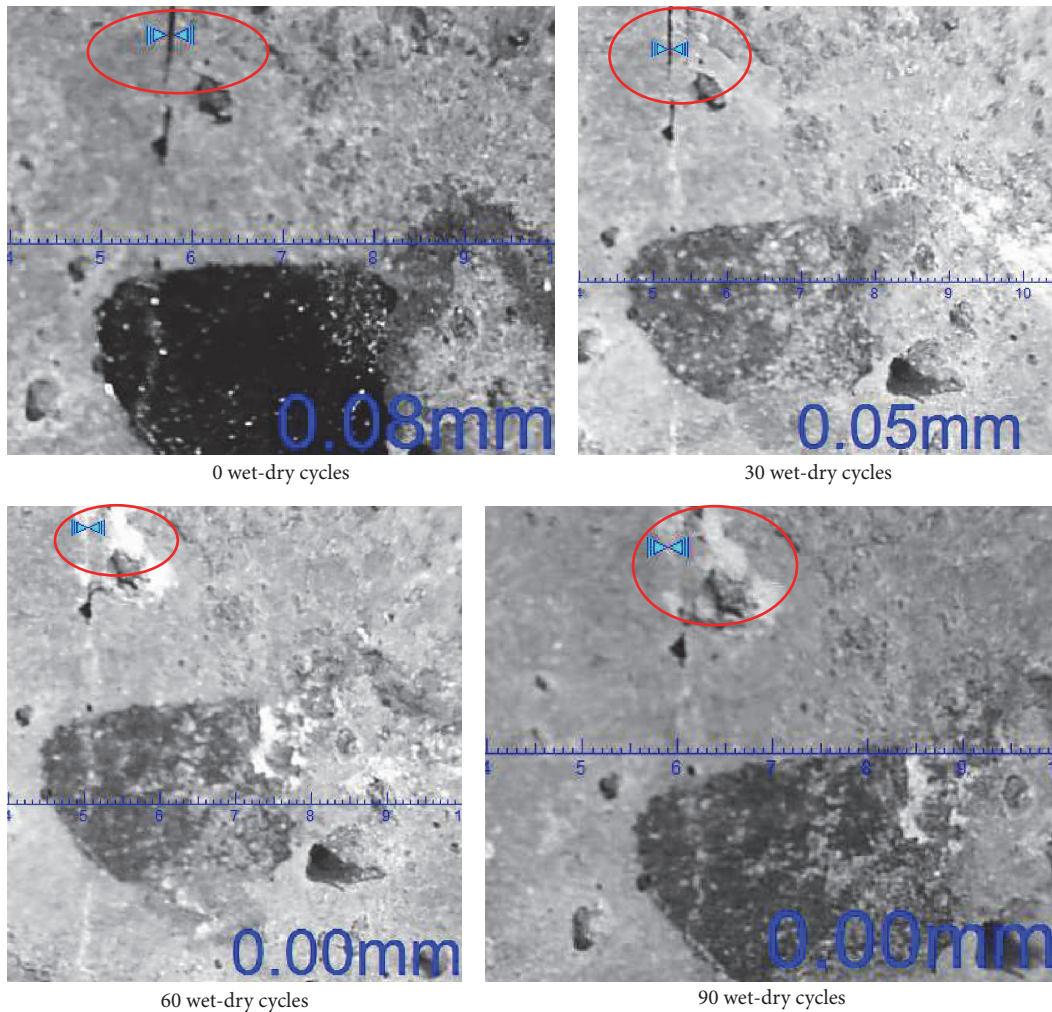


FIGURE 3: Detail of crack evolution on C80D10WD2 point 1 with maximum crack width of 80 microns.

50 microns and 0 microns, respectively, after 90 days of wet-dry cycles. Picture in Figure 3 gives a crack width decreasing illustration case of maximum crack width of 80 microns on 10 mm diameter bars point 1. Small bar diameter creates an environment which makes microcracks around 80 microns decrease quickly.

When the initial crack widths were in the range of 100–150 microns, as shown in Table 6, test results of two points on each crack remained nearly the same during all environment exposure; this indicates that crack width changed a little when initial crack widths are in the range of 100–150 microns. Detail

of crack evolution on C150D10WD point 2 with maximum crack width of 150 microns was shown in Figure 4.

Using the same procedure, the crack widths of 2 points on each crack were measured for the specimen when the initial crack widths were in the range of 210–230 microns. The specimens were chosen randomly and the testing result was shown in Table 7 and Figures 5 and 6.

To have more clear view on the evolution of initial crack widths, the testing results of all points 1 of the specimens were shown in Figure 5. As shown in Figure 5, the testing results of all points increased gradually as the cycle number of wet-dry

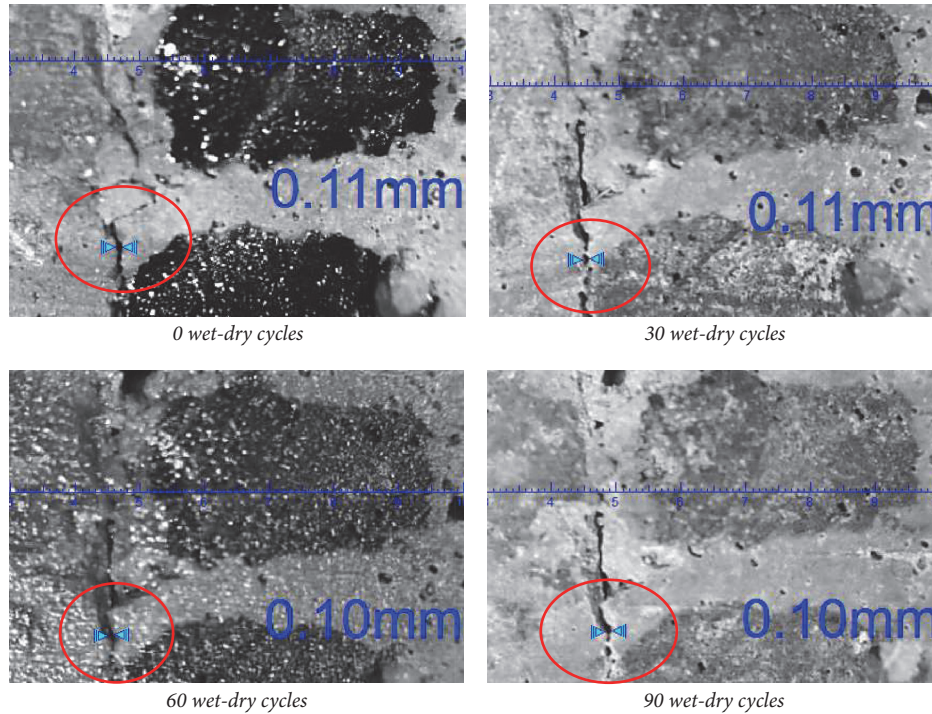


FIGURE 4: Crack evolution of C150D10WD point 2.

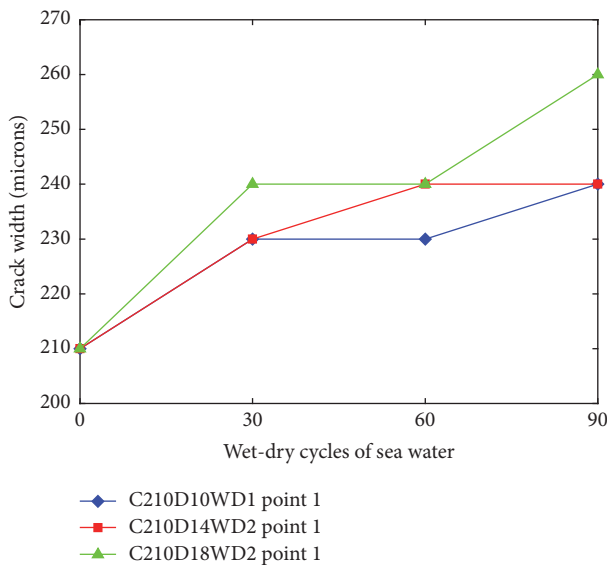


FIGURE 5: Relation between crack width and wet-dry cycles.

increased. The crack width of specimens with bar diameter of 18 mm increased more quickly from 210 microns to 260 microns. The large bar diameter hence impacted obviously on the evolution of crack width when the initial crack widths were in the range of 210–230 microns during the wet-dry cycles.

The experimental phenomenon of bond specimens with four classes of initial crack width of 0 microns, 80 microns, 150 microns, and 210 microns and three sizes of bar diameters

of 10 mm, 14 mm, and 18 mm has shown that when initial crack widths are around 80 microns all cracks tend to decrease. Nevertheless cracks on specimens with smaller diameter bars decreased faster than those with bigger diameters. When the cracks widths were in the range of 100–150 microns, the crack widths tend to stabilize or decrease a little; that is, their initial crack width was 100–150 microns and 100–130 microns after 90 wet-dry cycles. When the initial crack widths were in the range of 210–230 microns, all initial crack widths increased as the cycle number of wet-dry increased. Evolution of crack width showed that the speed of crack growth is directly proportional to the bar diameter and it is faster for larger diameters.

3.2. *Ultimate Bond Strength.* The ultimate pull-out forces were gotten by pull-out test and ultimate bond strength based on the embedment length and reinforcing bar diameter [6, 21] using the formula

$$F_b = \frac{P_u}{\pi DL}, \tag{1}$$

where F_b is the bond strength MPa; P_u is the ultimate pull-out force; D is the diameter of reinforced bar; and L is the embedment length which was assumed to be equal to 5 times the diameter.

The averages value of pull-out forces and bond strength of all specimens were listed in Table 8. The result listed in Table 8 shows an interdependency between the bar diameter and bond strength, where the average bond strength of specimens decreased as the diameter increased; however there is no

TABLE 8: Pull-out forces and bond strength of all specimens.

Crack width	Bar diameter 10 mm			Bar diameter 14 mm			Bar diameter 18 mm		
	Specimen name	Pull-out force kN	Bond strength MPa	Specimen name	Pull-out force kN	Bond strength MPa	Specimen name	Pull-out force kN	Bond strength MPa
0	COD10RE	19.18	9.95	COD14RE	41.05	10.86	COD18RE	65.46	10.48
0	COD10WD	23.12	11.99	COD14WD	42.32	11.20	COD18WD	63.87	10.22
80	C80D10WD	17.99	9.33	C80D14WD	33.68	8.91	C80D18WD	50.52	8.08
150	C150D10WD	23.08	11.96	C150D14WD	43.60	11.53	C150D18WD	64.68	10.35
210	C210D10WD	19.85	10.29	C210D14WD	48.22	12.76	C210D18WD	65.66	10.51

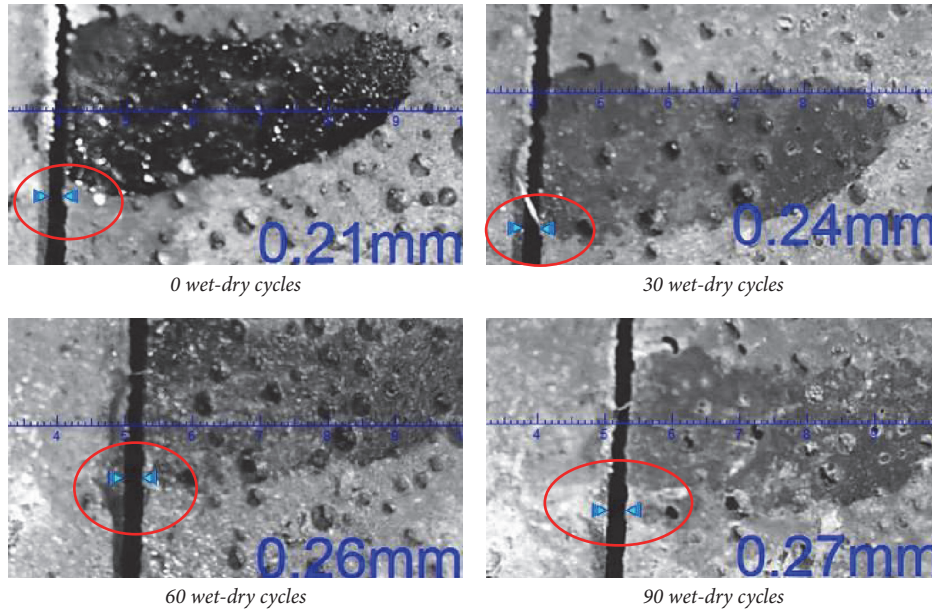


FIGURE 6: Detail of crack evolution on C210D18WD2 point 2 with maximum crack width of 210 microns.

clear tendency of bond strengths for different widths of initial cracks.

For all specimens under wet-dry cycles of seawater and with different crack width, the pull-out forces showed no clear tendency, as shown in Figure 7. The bond strength of specimen with the same crack width but different bar diameters has shown a decreasing tendency when the bar diameter increased. Discontinuities are one of the most harmful types of damage to the durability of concrete structures [3]. It implies that when we made a microcrack less than 80 microns at the earlier age, the concrete crack might be closed and disappeared.

Figure 8 gives curves of pull-out force and relative slip-page displacement from pull-out test for the specimens without initial cracks. As shown in Figure 8 and listed in Table 8, the combined effects of crack widths and bar diameters on the bond strength have shown no clear tendency; the ductility of specimens however decreased as the diameter increased.

3.3. Chloride Diffusion in Cracked Concrete. As it was previously mentioned, samples of concrete were drilled from the specimens and subdivided along the depth of sample into 5 pieces of slices and the thickness of each slice was about 8 mm. The slice was smashed by pulverization and chloride content was tested. The test and analysed results of chloride contents for different bar diameter were listed in Tables 9, 10, and 11. The chloride contents and its incremental percentage of chloride content for the specimens with 10 mm bar diameter were listed in Table 9, where incremental percentage was the results compared with the chloride content of reference specimen. As listed in Table 9, the chloride content decreased as the depth of concrete increased. At the same depth, the chloride content increased as the width of initial cracks increased. As listed in Table 9, the incremental percentage of chloride content decreased quickly as the depth of concrete

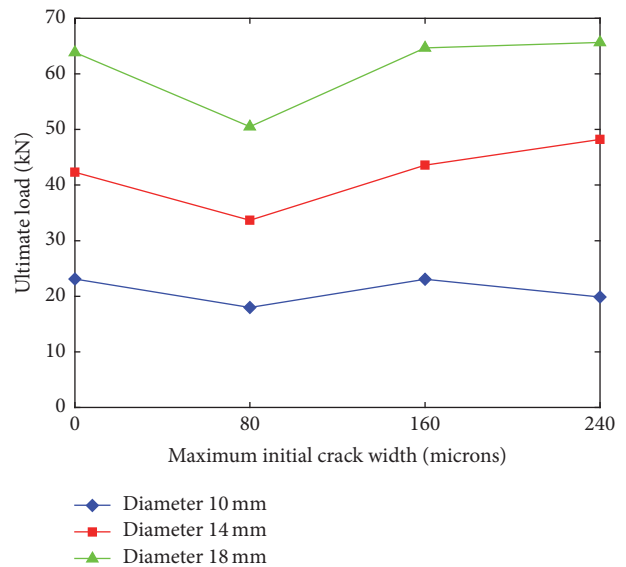


FIGURE 7: Relationship of initial crack width and ultimate pull-out force.

increased when the widths of initial cracks were less than 80 microns; the incremental percentage of chloride content however decreased slowly as the depth increased when the width of initial cracks was larger than 100 microns. As listed in Tables 10 and 11, the chloride content decreased as the depth of concrete increased and the chloride content increased as the width of initial cracks increased, in accordance with the same change rules for incremental percentage of chloride content.

The chloride content of specimens with different bar diameters and different width of initial cracks was shown in Figure 9. The chloride penetration in specimens was impacted by width of initial crack and bar diameters.

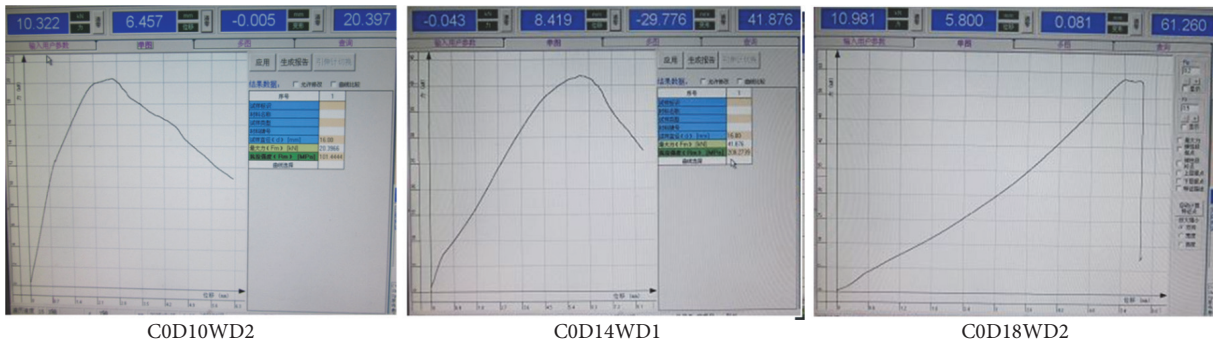


FIGURE 8: Curves of pull-out force-relative slippage displacement of C0D10WD2, C0D14WD1, and C0D18WD2.

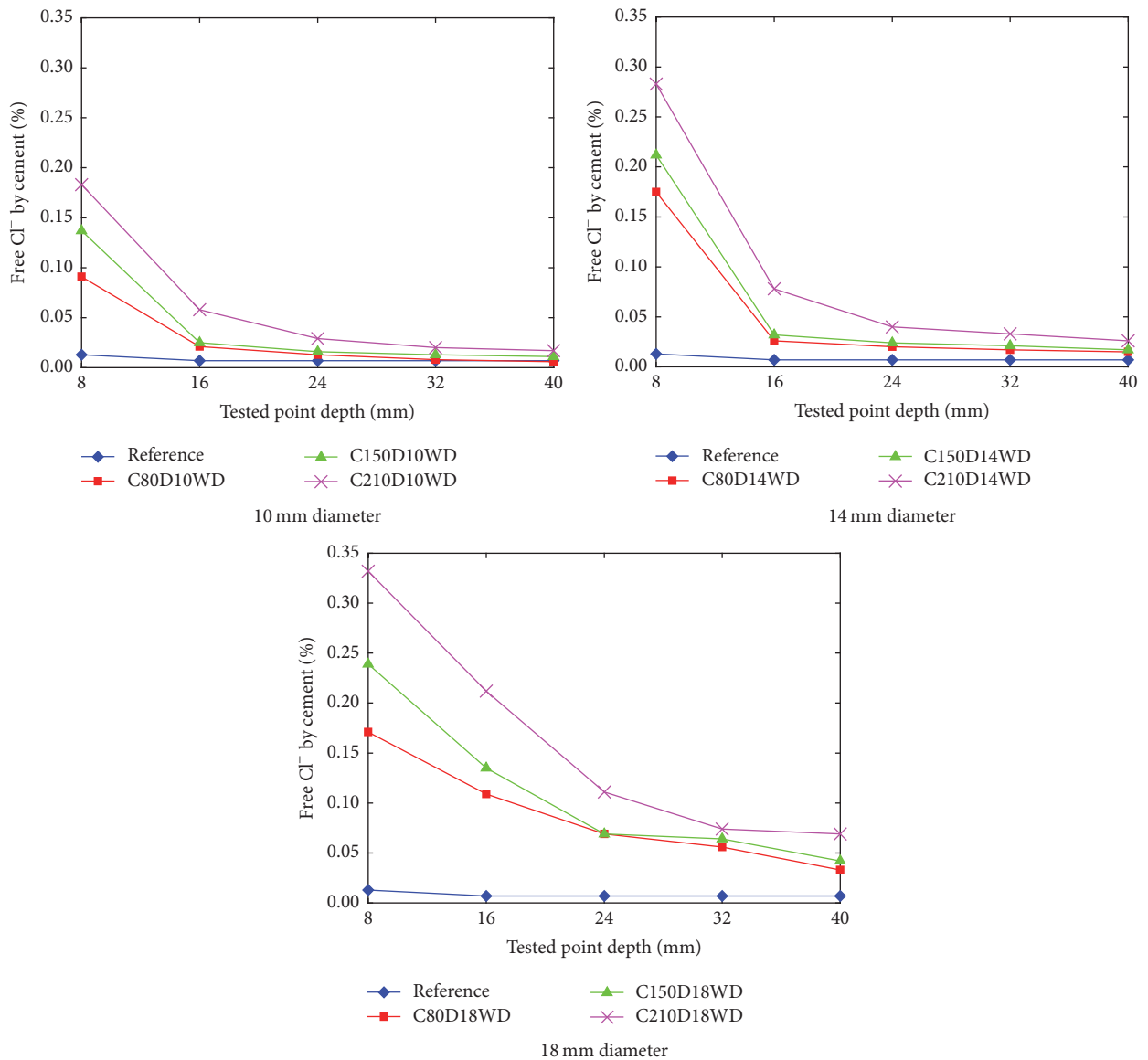


FIGURE 9: Chloride content of specimens with different bar diameters and different width of initial cracks.

TABLE 9: Chloride content and incremental percentage for specimens with 10 mm bars diameter.

Depth	Reference	Free (cl ⁻) by cement (%)			Percentage of intercracks		
		C80D10WD	C150D10WD	C210D10WD	50–80	100–110	210–230
8	0.013	0.091	0.137	0.183	86%	91%	92%
16	0.007	0.021	0.025	0.058	67%	72%	88%
24	0.007	0.013	0.016	0.029	46%	56%	76%
32	0.007	0.008	0.013	0.020	8%	46%	65%
40	0.007	0.006	0.011	0.017	–9%	36%	56%

TABLE 10: Chloride content and incremental percentage for specimens with 14 mm bars diameter.

Depth	Reference	Free (cl ⁻) by cement (%)			Percentage of intercracks		
		C80D14WD	C150D14WD	C210D14WD	50–80	110–150	210–230
8	0.013	0.175	0.212	0.283	93%	94%	95%
16	0.007	0.026	0.032	0.078	73%	78%	91%
24	0.007	0.020	0.024	0.040	65%	71%	83%
32	0.007	0.017	0.021	0.033	59%	67%	78%
40	0.007	0.015	0.017	0.026	53%	59%	73%

TABLE 11: Chloride content and incremental percentage for specimens with 18 mm bars diameter.

Depth	Reference	Free (cl ⁻) by cement (%)			Percentage of intercracks		
		C80D18WD2	C150D18WD2	C210D18WD2	50–80	100–110	210–230
8	0.013	0.171	0.239	0.332	92%	95%	96%
16	0.007	0.109	0.135	0.212	94%	95%	97%
24	0.007	0.069	0.069	0.111	90%	90%	94%
32	0.007	0.056	0.064	0.074	87%	89%	91%
40	0.007	0.033	0.042	0.069	79%	83%	90%

As shown in Figure 9, for the specimens with the same bar diameter, the chloride content decreased as the depth of concrete increased, and the chloride content increased as the width of initial crack increased. At the depth of 40 mm, the chloride contents were nearly the same when the crack width was less than 80 microns and with 10 mm diameter. The chloride content equally increased quickly when the bar diameter increased from 10 mm to 18 mm and width of initial crack increased. This means that the penetration of chloride ion on bond specimens was significantly impacted by the interaction of bar diameters and width of initial cracks.

4. Conclusion

This paper presents an experimental study on the impact of the combined actions of wet-dry cycles, initial cracks, and different bar diameters on the cracks evolution, chloride penetration, and the bond strength of reinforced concrete specimens. The following conclusions can be drawn from the results of the current study:

- (1) When the bond specimen is with small diameter of steel bars and with crack width less than 80 microns,

after 90 days of wet-dry cycles of seawater, the cracks vanished rapidly compared to those with bigger diameter bars.

- (2) When cracks width were in the range of 100–150 microns, after 90 days of wet-dry cycles of seawater, the width of cracks decreased slightly; however the cracks width increased if the crack widths were larger than 200 microns.
- (3) After 90 days of wet-dry cycles of seawater, the chloride content decreased along the depth of concrete, and the chloride content increased as the widths of initial cracks or bars diameter increased.
- (4) The combined effects of crack widths and bar diameters on the bond strength have shown no clear tendency in the current study; however the ductility of bond specimens decreased as the diameter increased.

Conflicts of Interest

The authors declare that there are no conflicts of interest regarding the publication of this paper.

Acknowledgments

This work is part of the projects financially supported by the Chinese National Natural Science Foundation (NSFC) Grant no. 51578031 and by the open topics of State Key Laboratory of Subtropical Architecture Science (SKLSAS) in South China University of Technology (2016ZA03). The authors gratefully acknowledge the financial support received from the NSFC and SKLSAS.

References

- [1] W. Xue, L. Zhang, Y. Xiong, J. Chen, and W. Jin, "Accelerating tests for the performance deterioration of concrete exposed to chloride media," *Procedia Engineering*, vol. 27, pp. 1635–1643, 2012.
- [2] C. Q. Li and R. E. Melchers, "Time-dependent risk assessment of structural deterioration caused by reinforcement corrosion," *ACI Structural Journal*, vol. 102, no. 5, pp. 754–762, 2005.
- [3] L. Basheer, J. Kropp, and D. J. Cleland, "Assessment of the durability of concrete from its permeation properties: a review," *Construction and Building Materials*, vol. 15, no. 2-3, pp. 93–103, 2001.
- [4] M. Chemrouk and T. Tahenni, "Étude des flèches et des ouvertures de fissures des poutres en béton arme contenant des fibres d'acier," in *Proceedings of the 1st International Conference on Sustainable Built Environment Infrastructures in Developing Countries ENSET (SBEIDCO '09)*, p. 1, Oran, Algeria, 2009.
- [5] G. Malumbela, P. Moyo, and M. Alexander, "Behaviour of RC beams corroded under sustained service loads," *Construction and Building Materials*, vol. 23, no. 11, pp. 3346–3351, 2009.
- [6] Z. Z. Rijal, A. B. Abd Rahman, R. N. Mohamed, I. S. Ibrahim, and S. Z. Sooria, "Comparison of bond stresses of deformed steel bars embedded in two different concrete mixes," in *Proceedings of the 9th Asia Pacific Structural Engineering & Construction Conference (APSEC '15) and 8th Asean Civil Engineering Conference (ACEC '15)*, pp. 131–136, Kuala Lumpur, Malaysia, November 2015.
- [7] X. He and D. Peng, "Experimental study on crack resistance property of fresh polypropylene fiber concrete," in *Proceedings of the International Conference on Multimedia Technology (ICMT '11)*, pp. 1064–1069, IEEE, Hangzhou, China, July 2011.
- [8] C. Q. Li, "Initiation of chloride-induced reinforcement corrosion in concrete structural members—experimentation," *ACI Structural Journal*, vol. 98, no. 4, pp. 502–510, 2001.
- [9] C. Q. Li, "Initiation of chloride-induced reinforcement corrosion in concrete structural members—prediction," *ACI Structural Journal*, vol. 99, no. 2, pp. 133–141, 2002.
- [10] C. Q. Li and R. E. Melchers, "Time-dependent reliability analysis of corrosion-induced concrete cracking," *ACI Structural Journal*, vol. 102, no. 4, pp. 543–549, 2005.
- [11] Z. X. Chen Jinping, *The Study on the Durability of the Concrete Structure*, IEEE, Piscataway, NJ, USA, 2010.
- [12] L. Schueremans, D. Van Gemert, and S. Giessler, "Chloride penetration in RC-structures in marine environment—long term assessment of a preventive hydrophobic treatment," *Construction and Building Materials*, vol. 21, no. 6, pp. 1238–1249, 2007.
- [13] J. Pommersheim and J. Clifton, "Prediction of concrete service-life," *Materials and Structures*, vol. 18, no. 1, pp. 21–30, 1985.
- [14] N. Verma and A. K. Misra, "Bond characteristics of reinforced TMT bars in self compacting concrete and normal cement concrete," *Alexandria Engineering Journal*, vol. 54, no. 4, pp. 1155–1159, 2015.
- [15] F. M. De Almeida Filho and A. L. H. D. C. El Debs, "Numerical approach of the bond stress behavior of steel bars embedded in self-compacting concrete (SCC) and in ordinary concrete in pullout models," *Science and Engineering Journal*, vol. 23, no. 2, pp. 57–66, 2014.
- [16] M. R. Kabir and M. M. Islam, "Bond stress behavior between concrete and steel rebar: critical investigation of pull-out test via Finite Element Modeling," *International Journal of Civil And Structural Engineering*, vol. 5, no. 1, pp. 80–90, 2014.
- [17] M. N. S. Hadi, "Bond of high strength concrete with high strength reinforcing steel," *Magazine of Concrete Research*, vol. 56, no. 9, pp. 545–557, 2004.
- [18] F. Yan, Z. Lin, and M. Yang, "Bond mechanism and bond strength of GFRP bars to concrete: a review," *Composites Part B: Engineering*, vol. 98, pp. 56–69, 2016.
- [19] A. M. Diab, H. E. Elyamany, M. A. Hussein, and H. M. Al Ashy, "Bond behavior and assessment of design ultimate bond stress of normal and high strength concrete," *Alexandria Engineering Journal*, vol. 53, no. 2, pp. 355–371, 2014.
- [20] X. Fu and D. D. L. Chung, "Improving the bond strength between steel rebar and concrete by ozone treatment of rebar and polymer addition to concrete," *Cement and Concrete Research*, vol. 27, no. 5, pp. 643–648, 1997.
- [21] A. Foroughi-Asl, S. Dilmaghani, and H. Famili, "Bond strength of reinforcement steel in self-compacting concrete," *International Journal of Civil Engineering*, vol. 6, no. 1, pp. 24–33, 2008.
- [22] Y. Shi and X. Li, "Analysis of ductility of composite steel-concrete structure based on computer simulation technology," in *Proceedings of the 7th International Conference on Measuring Technology and Mechatronics Automation (ICMTMA '15)*, pp. 141–144, June 2015.
- [23] L. Marsavina, K. Audenaert, G. De Schutter, N. Faur, and D. Marsavina, "Experimental and numerical determination of the chloride penetration in cracked concrete," *Construction and Building Materials*, vol. 23, no. 1, pp. 264–274, 2009.

Research Article

Experimental Studies on Punching Shear and Impact Resistance of Steel Fibre Reinforced Slag Based Geopolymer Concrete

Srinivasan Karunanithi

SCALE, VIT University, Vellore, Tamil Nadu, India

Correspondence should be addressed to Srinivasan Karunanithi; srinivasan.k@vit.ac.in

Received 3 February 2017; Accepted 12 March 2017; Published 22 March 2017

Academic Editor: Peng Zhang

Copyright © 2017 Srinivasan Karunanithi. This is an open access article distributed under the Creative Commons Attribution License, which permits unrestricted use, distribution, and reproduction in any medium, provided the original work is properly cited.

The study was focused on slag based geopolymer concrete with the addition of steel fibre. The slag based geopolymer concrete was under shear load and sudden impact load to determine its response. The punching shear represents the load dissipation of the material and the energy absorption capacity of the geopolymer concrete to impact load. The various percentage of steel fibre in the slag based geopolymer concrete was 0.5%, 1.0%, and 1.5%. Overall the dosage 0.5% of steel fibre reinforced slag based geopolymer shows better results with a punching shear of 224 kN and 1.0% of steel fibre incorporated geopolymer concrete had the better energy absorption capacity with 3774.40 N·m for first crack toughness and 4123.88 N·m for ultimate failure toughness.

1. Introduction

The paper investigates the flexural behaviour of shallow reinforced concrete beams strengthened with high strength steel cord and carbon fibre reinforced geopolymers, cured at room temperature. The flexural behaviour was assessed by means of four-point bending test. Two beam specimens for each system (i.e., steel cord and carbon fibre reinforcement) and one unstrengthened control beam were casted and tested by Menna et al. [1]. The passivating capacity of synthetic specimens with three various fly ash mortars treated with three activators and the stability of the passive state under the effect of 0%, 0.2%, 0.4%, and 2% chloride accompaniments relative to the binder material, in an environment of seemingly constant humidity, and in humidity cycles were analysed.

The development with time of corrosion potential (E_{corr}) and polarisation resistance (R_p) was calculated. Polarisation curves and time constants (s) were also measured for specimens using little period galvanostatic pulses [2]. The predicted and the experimental pullout curves were determined for all the circumstances for firing and testing temperatures. The friction coefficient effects, the fibre Young's modulus, and concrete rupture strength and the testing temperature on the pullout performances were showing high

performance [3]. The addition of ceramic fibre to plain concrete has considerably increased its properties, dynamic strength, critical strain, and energy absorption [4].

Multiwalled Carbon Nanotubes (MWCNTs) fibres in the concrete studied in the range 0.1 to 0.5% by weight and fibres are poorly dispersed and strictly agglomerated in 1% of concrete weight. MWCNT improves Young's modulus, flexural strength, and flexural toughness by as much as 160%, 109%, and 275%, respectively. It also boosted the fracture energy and increased the electrical conductivity by 194% [5]. Addition of carbon fibres in geopolymer concrete improves its electrical conductivity and the electrical resistance of concrete analysed through AC-impedance spectroscopy [6]. Impact strength and compressive strength were determined for the concrete added with carbon fibre from 0% to 1% by weight of concrete. The 0.5% of carbon fibre was the optimum dosage that performed well in mechanical properties compared to the other ratios [7].

The spherical shape of fly ash can increase the extrudability of geopolymer mixture, followed by the denser and compact microstructure of the final geopolymeric boards with low percentage of fly ash. However, when excess fly ash was added, the enhancement of the microstructure caused by fly ash cannot reward the reduction of geopolymer because of the low pozzolanic reactivity of fly ash in situation of

high percentage of binder. So, the microstructure of fly ash-geopolymer boards was loosely packed [8]. Nazari et al. studied the flexural strength of unreinforced and reinforced condition with Boroaluminosilicate as binder. They achieved high flexural strength of 9.5 ± 0.4 for unreinforced still high strength and 11.8 ± 0.9 for the reinforced condition. The high strength of the reinforced condition is due to bond between steel fibres and geopolymer in the presence in Boroaluminosilicate binder. Further it is found that spherical shape of fly ash has an influence on concrete and increases the extrudability of geopolymer mixture. It results in dense and compact microstructure of concrete matrix [9].

A torsional behaviour of steel fibre reinforced concrete (SFRC) beam samples was studied by using the current analytical models and the suggested approaches. The linear strain distribution across the effective thickness of shear-flow zone, which has been normally expected in the analysis of reinforced concrete or SFRC torsional members, is also evidently detected through the torsional tests on the SFRC beams and well assessed by the suggested models. The COV (coefficient of variation) values were 9.1% and 10.4%, respectively. First modelling provided the maximum accuracy in estimating their ultimate torsional strengths, and second modelling shows the better simulation results on their torsional behaviour [10].

The stress-strain curves of concrete under the various impact loads. The results show the effect of the strain rate and the impact resistance of concrete [11]. The addition of ceramic fibre for 0.1% and 0.2% in concrete performed the considerable increase in the dynamic strength and elastic modulus of concrete [12]. The various types of fibres were used in concrete with different percentage like cellulose (0.15%), polypropylene (0.15%), and steel fibre (0.50%). The significant impact strength was attained by the concrete with steel fibre [13]. The fibre addition of 2.4% in concrete has increased the postcrack energy of 2.98 J. The improvement in the flexural and impact resistance of the concrete was due to the discontinuous fibre distribution. Around 38.5% of strength increase was observed for fibre concrete compared to reference concrete [14].

The 65% strain rate and energy absorption of concrete were improved when the BFRGC (Basalt Fibre Reinforced Geopolymeric Concrete) was used in concrete. 0.3% of optimum volume of fibre in concrete shows the improvement of 8.9% of specific energy absorption for geopolymer concrete [15].

2. Materials and Experimental Methods

2.1. Slag. The Ground Granulated Blast Furnace Slag was used as binder of geopolymer concrete production. It is an industrial by-product that was supplied by Ferrosilicon manufacturing firm and the various properties of the slag were shown in Table 1 conforming to BS 6699-1992 (British Standard) [16].

2.2. Fine Aggregate. Fine aggregate (river sand) used in the study was passing through 4.75 mm IS sieve, conforming to

TABLE 1: Physical and chemical properties of slag.

Observation	Slag
Colour	White
% passing through 45-micron sieve (wet sieving)	91.35
Specific gravity	2.86
Blaine's fineness (m^2/kg)	415
SiO ₂	37.3
Al ₂ O ₃	11.48
Fe ₂ O ₃	0.23
CaO	42.47
MgO	7.32
SO ₃	1.2
Moisture content	10–13%

TABLE 2: Sieve analysis of river sand.

Serial number	Sieve size (mm)	Cumulative% of river sand
1	4.75	96.60
2	2.36	95.70
3	1.18	69.60
4	0.6	19.70
5	0.3	5.20
6	0.15	1.30
7	0.075	0.10
8	Pan	—

grading zone-II of IS 383-1997 [17]. The specific gravity of the fine aggregate was 2.65. The grain size of river sand is shown in Table 2.

2.3. Coarse Aggregate. Gravel pieces which passed 12.5 mm sieve size, retained on 10 mm sieve, were used as coarse aggregate for concrete production, conforming to IS 383-1997 [17]. The specific gravity of the coarse aggregate was 2.73.

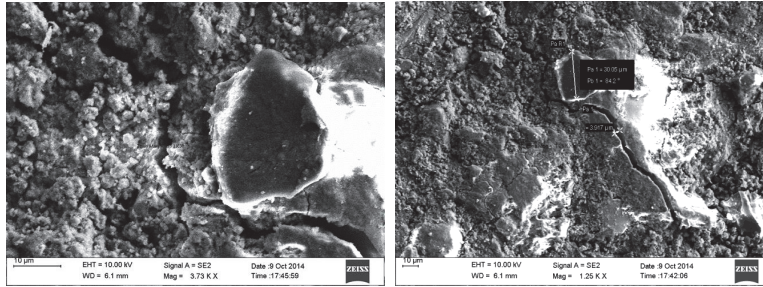
2.4. Alkali Activators and Chemical Admixtures. The alkali activator used in the study was sodium hydroxide solution prepared for 12 molarity concentration. The accelerator like calcium nitrate 1% and sodium sulfate of 10% of the weight of slag is also used in the concrete. For the improvement of workability, the high range water reducer was used as well as accelerator based superplasticizer (CERA-ACCL) at 1.5% by weight of slag.

2.5. Fibre Reinforcement. Glued steel fibres of 35 mm length and 0.5 mm diameter with an aspect ratio of 70 were added in geopolymer concrete at dosages of 0.5%, 1.0%, and 1.5%. The effects of steel fibre for different dosage of reinforcements were investigated in slag based geopolymer concrete in the slab-column junction setup. The properties of steel fibre are given in Table 3.

2.6. Curing Regime. An accelerated curing using hot air oven and steam curing was provided for the fresh geopolymer mixes. The specimens were cured in hot air oven curing at

TABLE 3: Properties of glued steel fibres (SF).

Fibre type	Length (l) (mm)	Diameter (d) (mm)	l/d ratio	Failure strain (%)	Tensile strength (MPa)	Relative density (kN/m^3)
SF	35	0.5	70	3.2	1721	7.65

FIGURE 1: Scanning electron microscope image of slag in 10 μm magnification.

100°C for 6-hour duration and a steam chamber curing at 75°C for 6-hour duration was used for curing the specimens. Later, the geopolymer specimens were remoulded and kept in ordinary room temperature ($37^\circ\text{C} \pm 2^\circ\text{C}$) and specimens are tested.

3. Experimental Methods

3.1. SEM and EDX Analysis. The scanning electron microscope (SEM) images were taken for the slag based geopolymer samples with alkali activators and accelerators. The concrete mix GC2 consists of Binder to Total Aggregate ratio (B/TA) of 0.22 and Fine Aggregate to Coarse Aggregate ratio (FA/CA) of 0.6 with Sodium Hydroxide (12 M). The test samples were prepared as powder and sample was kept stub for sputter coating machine in which the gold coating was applied. The gold coating helped for the conductivity between the samples and stubs in getting the image in the scanning electron microscope.

The SEM images, shown in Figures 1 and 2, have the same pattern of an image in the $2\ \mu\text{m}$ magnification. From the SEM image, the constituents which present in concrete are well agglomerated. The kind of agglomeration load is due to the presence of minerals such as Magnesium (Mg), Sodium (Na), calcium (Ca), and silica (Si) (Bastidas et al.) in the binder. Further the agglomeration is due to the dissolution of sodium ions with silica and alumina atoms form crystals. The formation of minerals and ions represents the three-dimensional alumina-silicate gel. The microstructure shows the formation of calcium, silicate, and alumina which forms the microcrystal. The key reason of formation of crystalline structure in the sample is because of the presence of calcium and silica in the slag. The formation of crystal makes ample addition to the density of binder. The SEM images for the various particle size are shown in Figures 1 and 2. These SEM images show the microstructures of the test samples with range of particle sizes. The particle size found in the samples is varying from $1.361\ \mu\text{m}$ to $6.102\ \mu\text{m}$. The resistance towards bearing the pressure and energy absorption of the geopolymer was amply improved by the increase in density

TABLE 4: Presence of elements in EDX analysis.

Element	Weight (%)	Atomic (%)	Compound (%)	Formula
C	1.74	3.19	6.36	CO_2
Na	9.46	9.09	12.75	Na_2O
Mg	2.67	2.43	4.43	MgO
Al	5.19	4.25	9.82	Al_2O_3
Si	12.38	9.73	26.48	SiO_2
S	0.79	0.54	1.96	SO_3
K	1.55	0.88	1.87	K_2O
Ca	25.97	14.31	36.34	CaO
O	40.25	55.57	—	—
Total	100	—	—	—

by the microcrystal structure formation. The density of gel formation was cumulative improving the structure of mortar in the geopolymer concrete.

The Energy-Dispersive X-ray spectroscopy (EDX) analysis was also carried out on the hardened slag based geopolymer paste samples and is shown in Figure 3. The EDX shows the presence of the elements and its percentage present in each sample; the presence of various elements and its percentage are shown in Table 4. The presence of CaSiO_3 was confirmed and the atomic weight of the major minerals is as follows: Calcium (Ca) = 14.31 and silica (Si) = 9.73 and the remaining are contents in the Oxide (O) = 55.57. This was taken from the test samples that are used for the SEM analysis.

The EDX results of samples show the presence of high percentage of calcium (Ca), Silicate (SiO_2), and oxides. So the result represents the presence of Wollastonite (CaSiO_3). Each test sample showed the same range of atomic weight and it contains the Magnesium, Sodium, Aluminum, Potassium, and sulfate in the minor quantity. The presence of the Sodium and sulfate in the samples was due to the alkali activators and accelerators.

3.2. Punching Shear Test. The specimen was prepared as the junction of column and slab. The curing regime for

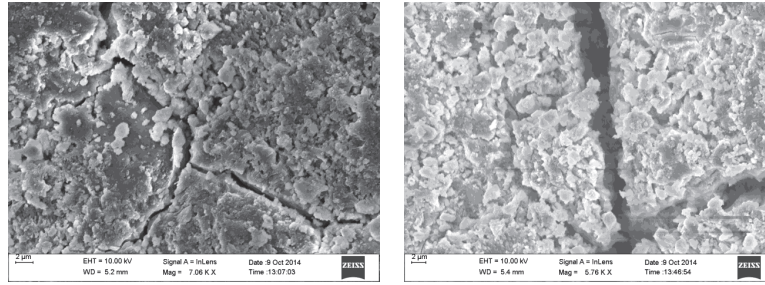


FIGURE 2: Scanning electron microscope image of slag in $2\ \mu\text{m}$ magnification.

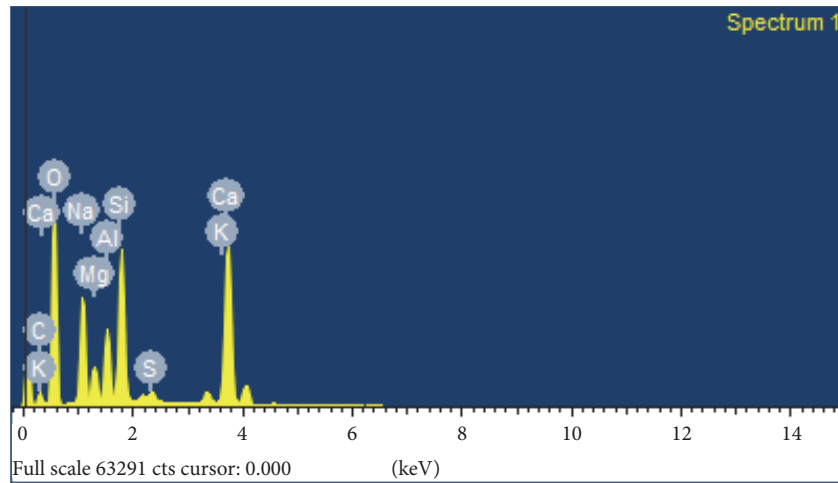


FIGURE 3: Measurement of the elements present in the sample by EDX analysis.

the slag based steel fibre reinforced geopolymer concrete specimens will be in hot air oven at a temperature of 100°C for 6 hours and in the accelerated curing called steam chamber curing for 75°C for 6 hours. This type of curing will provide the heat air with the moisture. The moisture air will not lead to the surface micro crack in the concrete. The specimen (Figure 4) was kept under the compressive load that applied on the column head of the specimen. The mid and edge (periphery) deflection were recorded till the ultimate load.

$$\text{Shear Stress } (\tau_c) = \frac{P_p}{U_1 \times d}, \quad (1)$$

where P_p is ultimate slab loading capacity (kN), U_1 is length of the perimeter at a distance “ $2d$ ” from the loaded area, d is effective depth of slab ($0.75D$), and D is overall depth of slab.

3.3. Impact Test. The size of the test specimen was 400 mm in diameter and 40 mm thick. The load of 4.75 kg was dropped from the height of 0.5 m on the centre of the specimen. The number of blows was recorded for obtaining the first crack and ultimate failure. The first crack in the specimen occurred from the bottom which denotes the failure of concrete and the rest of the load till ultimate failure load was taken by the

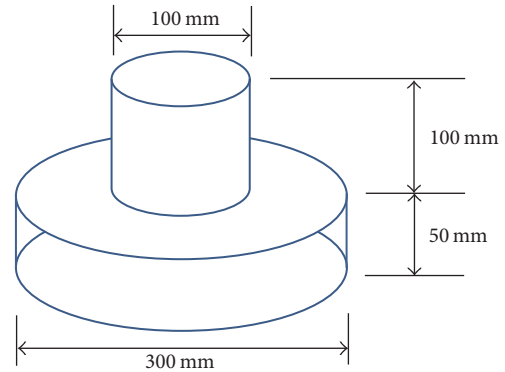


FIGURE 4: Specimen dimension.

fibre present in the specimen and the test setup is shown in Figure 5.

$$\text{Impact strength} = (9.81 \times \text{load}) \times \text{height} \times \text{number of blows.} \quad (2)$$

4. Discussion

4.1. Punching Shear Test. In the slag based geopolymer concrete, the addition of sodium hydroxide solution as the

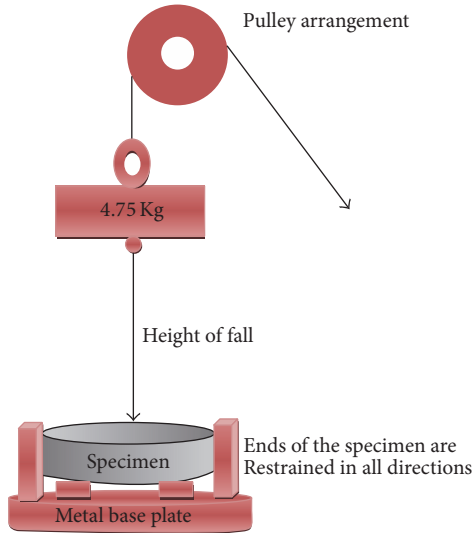


FIGURE 5: Setup of impact strength test for slag based geopolymer concrete.

alkali activator is enough for the geopolymerization reaction process for binding of concrete. The slag is having the enough amounts of silica and alumina in it. When the sodium hydroxide is mixed with binder the silica and alumina atoms present in the slag will dissolve by the hydrogen ions present in the solution. The chemical reaction taking place is called the polycondensation reaction leading to the 3-dimensional inorganic polymeric chain structure called Wollastonite. Wollastonite is also otherwise known as $CaSiO_3$. The reaction is immediate which mixed with the slag. The inorganic polymeric chain will develop and get strong bind only with the heat environment. The physical representation of the polymerization reaction was identified by the change in colour of the slag paste from white to dark green. The physical change of chemical reaction is taking place in the slag which we can see very easily. After the polymerization chain reaction reaches its saturation level there will be gradual change of colour from dark green to dusty white.

The punching shear test was conducted on hardened slag based fibre reinforced geopolymer concrete specimen after curing. The specimen was kept over the hollow metallic ring like the slab resting on the ring and the load was applied on the column which is on the centre of the slab specimen as shown in Figure 4. The test was conducted in the digital compression machine of 2000 kN capacity operated at a loading rate of 2.5 kN/sec. The test specimen has a column head of size 100 mm in diameter and 100 mm height and circular slab of size 300 mm in diameter and 50 mm thickness; both slab and column are casted monolith.

The punching shear strength of the slag based geopolymer concrete reinforced with steel fibre was carried out and the dosage of steel fibre in slag based geopolymer concrete is shown in Table 5. The concrete mixtures GC2 (B/TA = 0.22, FA/CA = 0.6) and GC5 (B/TA = 0.30, FA/CA = 0.44) and steel fibre were reinforced in plain concrete for various percentages of 0.5, 1.0, and 1.5 (GCF21, GCF22, GCF23, GCF51, GCF52, and GCF53) and were tested. The specimens were prepared

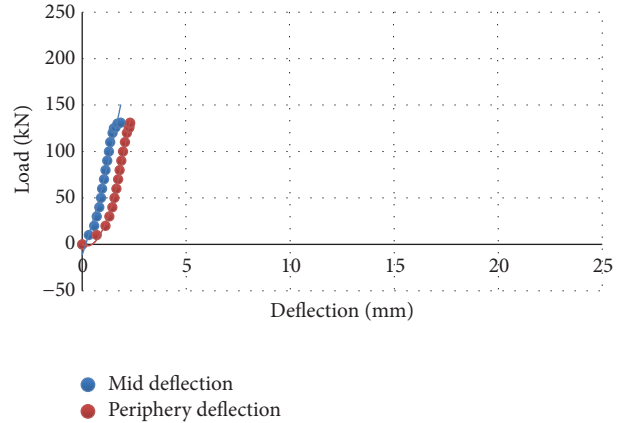


FIGURE 6: Punching shear values for control mix concrete (GC2).

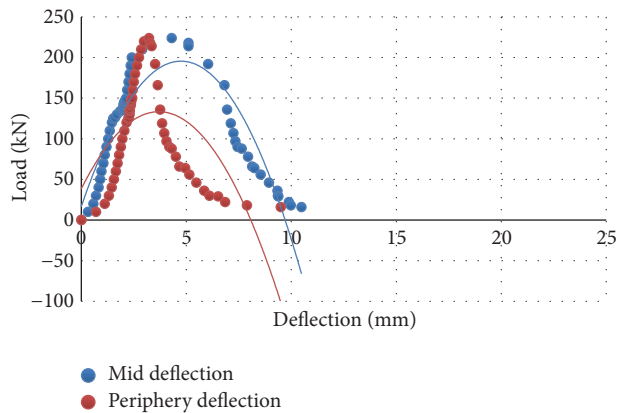


FIGURE 7: Punching shear values for 0.5% of steel fibre (GCF21).

as the slab-column junction for the size of column head of 100 mm × 100 mm diameter and slab thickness of 50 mm × 300 mm diameter. The samples were prepared for the control mixture and three various percentages of steel fibre.

The specimens were kept under the compressive load applied on the column head. The two dial gauges were used, and one was kept on the middle of the slab and another was kept at the edge periphery of the slab. When the load is applied on the column head, the sudden failure takes place in the slab. The ultimate load of the slab is shown in Table 6. The ultimate load for the control mix specimen (GC2) was 131.0 kN. In steel fibre reinforced concrete specimens, the ultimate load was increased to 1.75 times approximately less or more than the control concrete (without fibre). The concrete with 1.5% of steel fibre has attained the ultimate slab load of 234.0 kN. The shear mechanism was taking place in between column and slab when the load was applied on the column head. The shear stress was increased to double the times when compared with control mix (0% steel fibre) and steel fibre reinforced mix (1.5% steel fibre). The control mix attained 5.2 N/mm^2 and 1.5% of steel fibre reinforced concrete attained 12.3 N/mm^2 , shown in Table 6 and Figures 6–9. The steel fibre acts as a crack bridge to reduce the crack and the concrete was behaving as a ductile material in the shear face of the specimen which is slab-column junction. The sudden

TABLE 5: Dosage of steel fibre in slag based geopolymer concrete.

Mix ID	Slag	FA (kg/m ³)	CA	SF	Water (lit/m ³)	NaOH (kg)	B/TA	FA/CA	AC/B	Ca NO ₃ %	Na ₂ SO ₄
GC2	425	720	1200	0	127.5	40.13	0.22	0.6	0.3	1.00	10
GCF21	425	720	1200	12	127.5	40.13	0.22	0.6	0.3	1.00	10
GCF22	425	720	1200	24	127.5	40.13	0.22	0.6	0.3	1.00	10
GCF23	425	720	1200	36	127.5	40.13	0.22	0.6	0.3	1.00	10
GC5	530	530	1200	0	159	50.04	0.30	0.44	0.3	1.00	10
GCF51	530	530	1200	12	159	50.04	0.30	0.44	0.3	1.00	10
GCF52	530	530	1200	24	159	50.04	0.30	0.44	0.3	1.00	10
GCF53	530	530	1200	36	159	50.04	0.30	0.44	0.3	1.00	10

Note. GC: geopolymer concrete; GCF: geopolymer concrete with fibre; FA: fine aggregate; CA: coarse aggregate; SF: steel fibre; B/TA: binder to total aggregate; FA/CA: fine aggregate to coarse aggregate; AC/B: accelerator to binder.

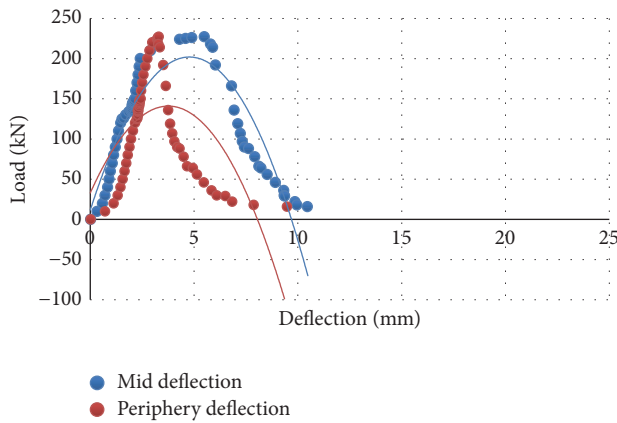


FIGURE 8: Punching shear values for 1.0% of steel fibre (GCF22).

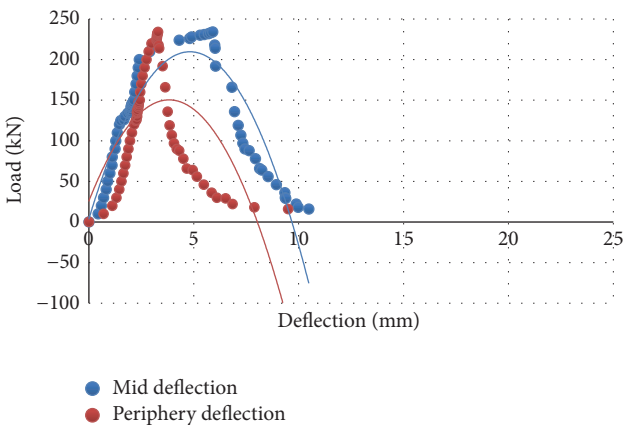


FIGURE 9: Punching shear values for 1.5% of steel fibre (GCF23).

failure was restricted to gradual failure when the steel fibre was reinforced in concrete.

4.2. Impact Test. The slag based steel fibre reinforced geopolymer concrete circular slabs are casted for the size of 50 mm thick and diameter of 400 mm. The specimens are well cured and kept for the testing of impact strength. The circular slab specimen rested on the base plate which has the four

TABLE 6: Shear stress for various percentage of steel fibre and its ultimate load capacity.

Mix ID	Steel fibre (%)	Shear stress (τ_c) (N/mm ²)	Ultimate slab loading (P_p) (kN)
GC2	0.0	5.2	131
GCF21	0.5	11.8	224
GCF22	1.0	11.9	227
GCF23	1.5	12.3	234
GC5	0.0	4.5	115
GCF51	0.5	9.7	184
GCF52	1.0	10.1	192
GCF53	1.5	10.5	200

supports on the four sides. The slab was well tightened with the base plate by the side screws. The 4.75 kg weight is tied with the rope which is dropped from 0.5 m height which is the fall of height at the middle point of the slag based steel fibre reinforced geopolymer concrete slab by using the pulley arrangement. The number blows were counted till the specimen fails [13].

- (i) First crack toughness was measured by seeing the crack on the slag and it occurs from the bottom of the slab. It means the failure of the concrete system. For without fibre first crack is the ultimate load.
- (ii) Ultimate failure toughness is the entire collapse of the fibre reinforced geopolymer concrete after several blows.
- (iii) Postpeak toughness is defined as ratio of ultimate failure toughness by first crack toughness.
- (iv) Increase in toughness is defined as an increase in value of steel fibre reinforced geopolymer concrete to the control geopolymer concrete.

The performance of the steel fibre in the slag based geopolymer concrete was also evaluated. The concrete mix GC2 (B/TA = 0.22 and FA/CA = 0.6) was tested with three various percentages of steel fibres like 0.5, 1.0, and 1.5 (GC21, GC22, and GC23). The test specimens were cast in the circular shape of diameter of 400 mm and thickness of 40 mm. The setup

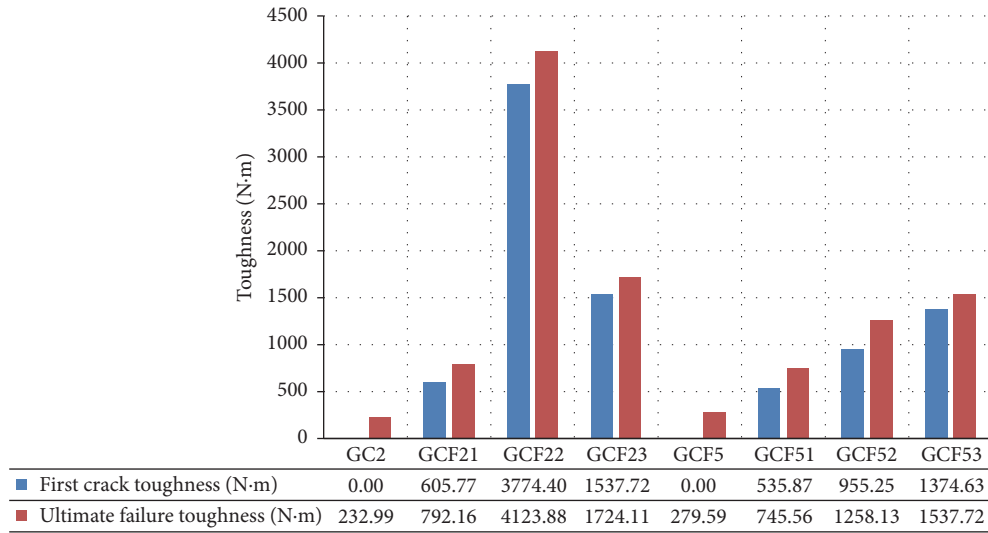


FIGURE 10: Impact toughness strength test for slag based geopolymer concrete with various percentage of steel fibre (Mix—GC2, GCF21, GCF22, and GCF23).

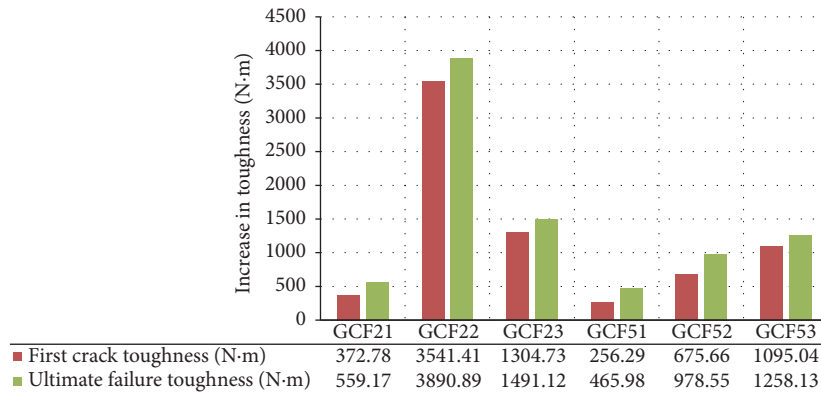


FIGURE 11: Increase in toughness of fibre reinforced geopolymer concrete to its reference concrete (GCF21, GCF22, and GCF23).

was arranged for the test, and the samples were clamped in the baseplate and load of 4.75 kg was dropped from the height of 0.5 m on the centre of the specimen (Figure 5). The numbers of blows were recorded when first crack formed in specimen as well as for ultimate failure of specimen. The first crack in specimen clearly indicates that ultimate failure load was reached by concrete and the rest of the impact load was absorbed by the specimen till its failure was taken by steel fibres in concrete [13]. In the controlled mix (GC2, without fibres), the impact load was applied on the specimen which absorbed the energy. The first crack was formed after the several impact loads on the specimen and the first crack started from the soffit of the slab. The first crack toughness was the same as ultimate failure toughness of 232.9 N·m. But in the fibre reinforced concrete samples when the first crack was formed, the number of blows was counted (Table 6), and toughness was calculated in Table 7.

The first crack toughness and ultimate failure toughness were calculated for all the remaining three mixtures and are shown in Figures 10–12. After several blows on the same sample, it was able to withstand the load till the fibre failure

and losing the intactness between the concrete matrixes. The higher fibre content also affected the energy absorption of the concrete that can be seen in the mix GCF23 (1.5% of steel fibres reinforced concrete).

The postpeak toughness was also done by first crack toughness-ultimate failure toughness of the steel fibre reinforced concrete specimens as shown in Figure 12.

$$\text{Impact strength} = (9.81 * \text{load}) * \text{height} * \text{number of blows.} \quad (3)$$

5. Conclusions

The experiments were carried out in the steel fibre reinforced slag based geopolymer concrete for finding out the mechanical properties and performance of slag and steel fibres. The presence of Wollastonite in concrete was persistently observed in SEM and EDX analysis. The performance of the steel fibre in the slag based geopolymer concrete was also evaluated by conducting tests like punching shear and

TABLE 7: Total number of blows for various percentage of steel fibre in concrete.

Mix ID	GCF2 (reference)	GCF21	GCF22	GCF23
Steel fibre (%)	0.0	0.5	1.0	1.5
Number of blows for initial crack formation	10	26	162	66
Number of blows for ultimate failure	—	34	177	74

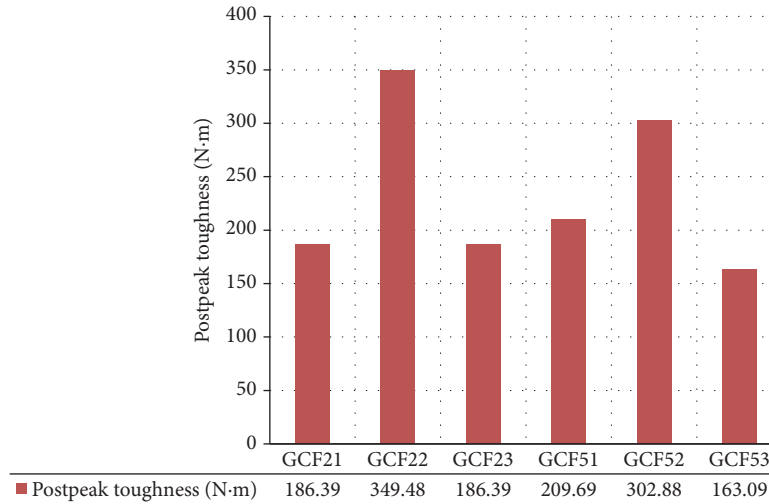


FIGURE 12: Postpeak toughness of each percentage of fibre reinforced geopolymer concrete (GCF21, GCF22, and GCF23).

impact test. From the observations the concrete mix ratio of GCF22 (binder to total aggregate ratio of 0.22 and fine to coarse aggregate ratio of 0.6 with 1.0% of steel fibre) was showing the better performance; in punching shear the stress was 11.9 N/mm^2 and in impact test the energy absorption of mixture GCF22 shows 3541.41 N-m in increase in toughness of first crack and 349.48 N-m in postpeak toughness. So it is observed that 1.0% of steel fibre is optimised and mixture GCF22 is suggested to be better in shear and energy absorption.

Conflicts of Interest

The author declares that there are no conflicts of interest regarding the publication of this paper.

References

- [1] C. Menna, D. Asprone, C. Ferone et al., "Use of geopolymers for composite external reinforcement of RC members," *Composites Part B: Engineering*, vol. 45, no. 1, pp. 1667–1676, 2013.
- [2] D. M. Bastidas, A. Fernández-Jiménez, A. Palomo, and J. A. González, "A study on the passive state stability of steel embedded in activated fly ash mortars," *Corrosion Science*, vol. 50, no. 4, pp. 1058–1065, 2008.
- [3] E. Cailleux, T. Cutard, and G. Bernhart, "Pullout of steel fibres from a refractory castable: experiment and modelling," *Mechanics of Materials*, vol. 37, no. 4, pp. 427–445, 2005.
- [4] H. Su, J. Xu, and W. Ren, "Mechanical properties of ceramic fiber-reinforced concrete under quasi-static and dynamic compression," *Materials and Design*, vol. 57, pp. 426–434, 2014.
- [5] M. Saafi, K. Andrew, P. L. Tang et al., "Multifunctional properties of carbon nanotube/fly ash geopolymeric nanocomposites," *Construction and Building Materials*, vol. 49, pp. 46–55, 2013.
- [6] S. Vaidya and E. N. Allouche, "Strain sensing of carbon fiber reinforced geopolymer concrete," *Materials and Structures*, vol. 44, no. 8, pp. 1467–1475, 2011.
- [7] T. Alomayri and I. M. Low, "Synthesis and characterization of mechanical properties in cotton fibre-reinforced geopolymer composites," *Journal of Asian Ceramic Societies*, vol. 1, no. 1, pp. 30–34, 2013.
- [8] Z. Yunsheng, S. Wei, and L. Zongjin, "Impact behavior and microstructural characteristics of PVA fiber reinforced fly ash-geopolymer boards prepared by extrusion technique," *Journal of Materials Science*, vol. 41, no. 10, pp. 2787–2794, 2006.
- [9] A. Nazari, A. Maghsoudpour, and J. G. Sanjayan, "Flexural strength of plain and fibre-reinforced boroaluminosilicate geopolymer," *Construction and Building Materials*, vol. 76, pp. 207–213, 2015.
- [10] H. Ju, K. S. Kim, D. H. Lee, J.-H. Hwang, S.-H. Choi, and Y.-H. Oh, "Torsional responses of steel fiber-reinforced concrete members," *Composite Structures*, vol. 129, pp. 143–156, 2015.
- [11] F. Liu, G. Chen, L. Li, and Y. Guo, "Study of impact performance of rubber reinforced concrete," *Construction and Building Materials*, vol. 36, pp. 604–616, 2012.
- [12] H. Su and J. Xu, "Dynamic compressive behavior of ceramic fiber reinforced concrete under impact load," *Construction and Building Materials*, vol. 45, pp. 306–313, 2013.
- [13] T. Rahmani, B. Kiani, M. Shekarchi, and A. Safari, "Statistical and experimental analysis on the behavior of fiber reinforced concretes subjected to drop weight test," *Construction and Building Materials*, vol. 37, pp. 360–369, 2012.
- [14] W. H. Kwan, M. Ramli, and C. B. Cheah, "Flexural strength and impact resistance study of fibre reinforced concrete in simulated

aggressive environment,” *Construction and Building Materials*, vol. 63, pp. 62–71, 2014.

- [15] W. Li and J. Xu, “Mechanical properties of basalt fiber reinforced geopolymeric concrete under impact loading,” *Materials Science and Engineering A*, vol. 505, no. 1-2, pp. 178–186, 2009.
- [16] British Standard, “Specification for Ground granulated blast furnace slag for use with Portland cement,” BS 6699-1992, British Standard, London, UK, 1992.
- [17] IS, “Indian standard specification for coarse and fine aggregates from natural sources for concrete,” IS 383-1970, Bureau of Indian Standards, New Delhi, India, 1997.

Research Article

Effect of Modified Rubber Particles Mixing Amount on Properties of Cement Mortar

Gang Xue and Mei-ling Cao

Architecture and Civil Engineering, Inner Mongolia University of Science and Technology, Baotou 014010, China

Correspondence should be addressed to Mei-ling Cao; caomeiling_2015@126.com

Received 1 December 2016; Accepted 4 January 2017; Published 29 January 2017

Academic Editor: Peng Zhang

Copyright © 2017 Gang Xue and Mei-ling Cao. This is an open access article distributed under the Creative Commons Attribution License, which permits unrestricted use, distribution, and reproduction in any medium, provided the original work is properly cited.

The crumb rubber cement mortar is prepared by the crumb rubber aggregates in 60 mesh which are modified by 1% polyvinyl alcohol (PVA) solution. Some mechanical properties of cement mortar with different crumb rubber aggregate amounts are researched including compressive strength, flexural strength, the ratio of compressive strength to flexural strength, impact resistance, and dry contraction percentage. In our tests, we consider six kinds of the rubber contents, 0%, 7.5%, 15%, 19%, 22.5%, and 30%, respectively. The optimal mixing amount of crumb rubber is determined by measuring three indices, the ratio of compressive strength to flexural strength, impact resistance, and dry contraction percentage. It is shown by test that the ratio of compressive strength to flexural strength is the smallest when the mixing amount of rubber is 19%; meanwhile high impact resistance and rational drying shrinkage are observed. The optimal mixing amount of the rubber particles is 19% determined by this test.

1. Introduction

With the rapid development of the automobile industry in recent years, there is a large increase of waste tires. The world has more than one billion tires every year. About 21% of these waste tires have been recycled into civil engineering applications, to be used as modifiers or additive in asphalt paving mixtures and portland cement concrete (PCC) mixtures [1]. Potential uses of rubber modified cement mortar have also been reported. Now, mortar is widely applied to decoration engineering, such as ground surface and wall surface. Water retention and cohesiveness of traditional mortar are poor. Before the mortar hardened, the water evaporation rate of its surface is faster than the rate of internal bleeding, producing shrinkage stress in mortar. When shrinkage stress is greater than tensile strength, it will produce shrinkage cracking. In addition, after exposure in low humidity air for a long-term, cracks may be produced in surface mortar and as time goes by, the cracks deepen and widen gradually, and will seriously weaken concrete bonding property. In the 1970s, people began to study polymer mortar in order to improve the cracking resistance of traditional mortar. It is shown that

the polymer mortar cannot meet the operating requirements due to its weaknesses, such as high costs, poor bond behavior, and poor durability. There are many methods for improving the toughness of cement concrete, and among them, adding rubber particles in concrete has attracted the attention of many scholars and become a research hot topic.

Tests by Segre and Joekes [2] showed that the bond force between rubber particles and cement-based materials will improve after modification by NaOH [3]. The flexural strength, compressive strength and fracture energy of the modified rubber particles mortar will improve. The experimental study by Benazzouk et al. [4] found that when the mixing amount changes between 15% and 35%, the flexural strength has increased to varying degrees, while the compressive strength has decreased. The failure mode presents plastic instead of brittle when the mixing amount is more than 10%. Sangson et al. [5] reported that the concrete mixed with rubber particles coming from waste tire makes the compressive strength and the elastic modulus slightly decreased, but at the meantime the curvature ductility increased by 90%. Adding rubber particles into cement mortar is rarely reported, but it can be predicted that adding appropriate

TABLE 1: The chemical composition of cement.

The chemical composition	SO ₃	MgO	Na ₂ O	K ₂ O	Cl ⁻	f-CaO	Loss on ignition
Content (%)	2.37	2.25	0.11	0.76	0.012	0.78	1.66

TABLE 2: The physical properties of cement.

The standard consistency water quantity (%)	Density (g/cm ³)	Loss on ignition (%)	Content of SO ₃ (%)	Stability (boiling method)	Setting time	
					Initial setting	Final setting
28.4	2.89	2.26	2.37	Eligible	2 h 07 min	3 h 23 min

amounts of rubber particles can improve toughness, sound absorption and insulation, and impact resistance of cement-based materials [6].

By antitheses test, research is done on the influence of modified rubber particle mixing amount [7–9] on the flexural strength, compressive strength, the ratio of compressive to flexural strength, impact resistance, and dry contractibility of cement mortar.

2. The Composition of Raw Material

2.1. Cement. The P.O42.5 ordinary portland cement is used in the test; the chemical composition of cement is shown in Tables 1 and 2.

2.2. Sand. The bulk density is 1592 kg/m³, the mud content is 8.9%, and the fineness modulus is 2.2.

2.3. Rubber Particle. The size of regenerated rubber particle is 60 mesh, and the bulk density is 290.1 kg/m³.

2.4. Mix Design. Quantity ratio of cement and sand is 1:2.8, with consistency varied 7~8 cm. Rubber particles float upward in the cement mortar when consistency is too large. There is the problem of nonuniform mixing of rubber particles in the cement mortar when consistency is too small. Therefore, the viscosity of the mortar should be adjusted in the process of adding rubber; rubber aggregates are divided by adding several times. Crumb rubber aggregates in 60 mesh were modified by 1% polyvinyl alcohol (PVA) solution and used for preparing crumb cement mortar.

3. The Test Method

The compressive strength test, flexural strength test, impact resistance test, and drying shrinkage test were carried out in this paper. Three indices which are the ratio of compressive strength to flexural strength, impact resistance, and dry contraction percentage are used to determine the appropriate mixing amount of crumb rubber.

3.1. The Test of Compressive Strength and Flexural Strength. The specimens of crumb rubber aggregate cement mortar were 100 mm × 100 mm × 100 mm for cube compressive strength. According to the “Method of testing cements—Determination of strength” (GB/T17671-1999) specification’s making and measuring are to measure its compressive

strength. The compressive strength of the mortar is in accordance with the polymer cement mortar specification of the “Technical specification for plastering mortar” (JGJ/T220-2010). The specimens of prism flexural strength were 40 mm × 40 mm × 160 mm, and their flexural strength is determined. The specimens were cured in standard curing for 28 days. The ratio of compression strength to flexural strength cement mortar with different dosage of 60-mesh rubber particles was obtained.

3.2. The Test of Impact Resistance. Make crumb rubber cement mortar according to previously determined mix proportion, smear mortar on polystyrene board with size of 600 mm × 250 mm × 50 mm and apparent density of (18.0 ± 0.2), and the alkali resistance network cloth is pressed into the mortar. The surface mortar thickness is 3.0 mm, and the alkali resistance network cloth is located 1.0 mm away from the surface mortar. Test procedures are as follows:

- (1) Make surface mortar layer upward, putting it on the impact resilience tester horizontally and clinging to the basement.
- (2) Let a steel ball whose nominal diameter is 50.8 mm impact test specimens in free fall from where the gravitational potential energy is 3.0 J. Impacting five times at each level, interval among the impact points and the distance between the impact point and the edge of the pitch should be not less than 100 mm. The annular crack around the impact point on the sample surface is regarded as the occurrence of impact damage. Specimen can be judged as no impact damage when the number of impact damage points in five tests is less than two and can be judged as impact damage when the number of impact damage points in five tests is not less than two.
- (3) If specimen is not damaged, for the 3.0 J potential energy of the gravitational impact, test will be done on the sample while the impact gravitational potential energy is increased by 1.0 J until the sample is damaged. If the potential energy of the gravitational impact is more than 7.0 J, the nominal diameter of 63.5 mm steel ball will be used.
- (4) If specimen is damaged for the gravitational impact of 3.0 J potential energy, test will be done on the sample until the sample is damaged, while the gravitational potential energy is decreased by 1.0 J.

3.3. *The Test of Dry Shrinking Performance.* Put well-mixed crumb rubber mortar into 40 mm × 40 mm × 160 mm prism-shaped test mould. The shrinkage head made of copper is fixed in the hole of two end surfaces of test mould, which is higher than the end of the test mould 8 ± 1 mm. Templates are removed when it has been cured under standard conditions for 7 days. The initial length of specimen is measured along the predetermined direction after being preset for 4 hours. Place the mortar specimens indoors with temperature of $20 \pm 2^\circ\text{C}$ and relative humidity of $(60 \pm 5)\%$, and measure the length of the specimen at 7 days, 14 days, 21 days, 28 days, 56 days, and 90 days, respectively, by which the natural drying shrinkage value of the mortar is calculated according to

$$\varepsilon = \frac{(L_0 - L_t)}{(L + L_d)} \quad (1)$$

In the formula, ε is natural drying shrinkage of specimens corresponding to the number of days; L_0 the original length of specimen cast mode for 24 hours when stripping (mm); L_t the measured length of specimens in t days (mm); L the standard length of specimens, 160 mm; and L_d the sum of the length of the two shrinkage heads, 20 ± 2 mm.

4. Discussion of Results

Different conclusions were drawn about the rubber's influence on concrete strength. Some results show [10] that rubber concrete flexural strength present the trend of increasing after reducing first with the increase of mixing amount of rubber particles, and other literature reports [11–13] that the flexural strength of cement concrete is always presents the tendency of decreasing with the increase of mixing amount of rubber particles. Research results all indicate that rubber particles can increase the toughness and deformation performance of cement concrete.

4.1. The Ratio of Compressive Strength to Flexural Strength.

From Figure 1, it can be seen that the mortar compressive strength decreases when the percentage of crumb rubber increases. When the percentage of the rubber particles reaches 20%, the compressive strength of mortar is about half the strength of the reference mortar sample. The test results about crumb rubber aggregate reducing mortar strength conforms to the related literature at home and abroad [14]. The main reasons leading to the decrease of the compressive strength of crumb mortar can be summarized as follows [2, 15]:

- (1) Rubber particles are inert organic polymer material with no hydration activity, while cement materials are inorganic. Interfacial adhesion between rubber particles and cement materials is weak, resulting in strength reduction of mortar.
- (2) The elastic moduli of rubber particles and cement materials differ greatly, and rubber particles cannot achieve the role of the skeleton. When rubber particle content is increased to a certain extent, it will cause

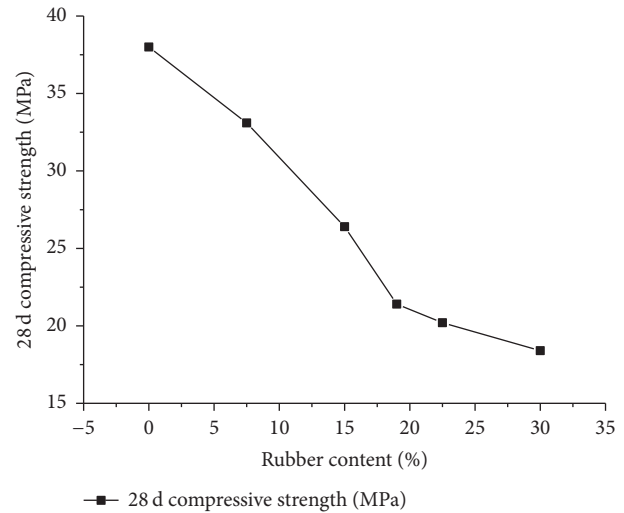


FIGURE 1: 28 d compressive strength of cement mortar with different amount of 60-mesh rubber particles.

internal structural discontinuity. The deformation between rubber particles and surrounding cement-based materials is inconsistent under the exterior load, resulting in strength reduction of the rubber cement mortar.

- (3) There are some pores with different sizes in cement mortar. Smaller mixing amount of rubber granules may fill the pore and improve the density of mortar which result in the increase of compressive strength. When the mixing amount exceeds the maximum of the pore, compressive strength will be weakened [8].

As depicted in Figure 2, the flexural capacity of mortar decreases with the increase of rubber aggregate content for the similar reason to the decrease of compressive strength. While, the plaster mortar is not a load-bearing structure, so the compressive strength and flexural strength may not be as major considerations for mortar performance. According to the strength consequences of the tests, the ratio of compressive strength to flexural strength of the rubber particles cement mortar can be calculated, which is an index of the detection of cracking mortar, and the smaller ratio of compressive strength to flexural strength is, the better mortar toughness could be indicated. Toughness is an ability of energy absorption by which the materials or structures deform plastically and fracture against the exterior load until failure. Material toughness is not only related to capacity, but also to deformability. Figure 3 shows the extent decreasing of the ratio of compressive strength to flexural strength, with the rubber mixing amount of 15% to 19%. When the rubber content is higher than 19%, in contrast, it has an upward tendency. It shows that the toughness of cement mortar is greatly improved by the addition to rubber particles. Rubber particles are elastomers which play the role of microelastic bodies in the cement mortar, helpful to absorb the strain energy and improve the deformability and toughness of cement mortar. The rubber particle shows great ability of

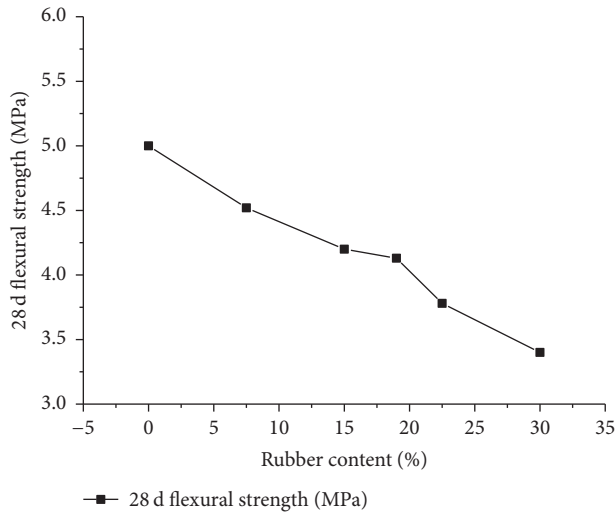


FIGURE 2: 28 d flexural strength of cement mortar with different amount of 60-mesh rubber particles.

deformation to accumulate large amount of strain energy when subjected to external loads for the reason of low elastic modulus. Mortar mixed with rubber particles can better maintain intact form and produce no sound of splitting, showing better elastic deformation capability during the test of compressive strength, as shown in Figure 4. While the cracks in the reference mortar base expanded and broadened rapidly after their appearance, brittle damage in the specimen occurred and sound can be heard when broken; failure feature is shown in Figure 5. In the flexural strength tests, reference mortar ruptured quickly and completely, as shown in Figure 6. while mortar mixed with rubber particles did not completely broken but partially bonded together when damaged, as shown in Figure 7. Researchers at home and abroad conducted many experimental studies for concrete or mortar mixed with fiber, and many achievements have been put into use in practical engineering fields [16]. In contrast, the research of concrete or mortar mixed rubber particles still in the experimental stage and failure mechanism of the concrete or mortar mixed with rubber particles are similar with those of the fiber concrete or mortar.

4.2. The Impact Resistance and Dry Shrinking Performance

4.2.1. The Impact Resistance. The impact resistance is an ability to resist material crack development and brittle fracture under external impact, which is an embodiment of its crack resistance. Researches at home and abroad show that the impact resistance of cement mortar improved with rubber particles added [17]. The impact resistances of 60-mesh rubber particles under different mixing amounts of cement mortar are shown in Figure 8. When the mixing amount of rubber particles is low, the improvement on impact resistance is not obvious because of the limited energy absorption of the mortar and the brittle failure mode. With the increase amount of rubber particles, impact resistance is enhanced gradually. Rubber particles in the cement mortar deform

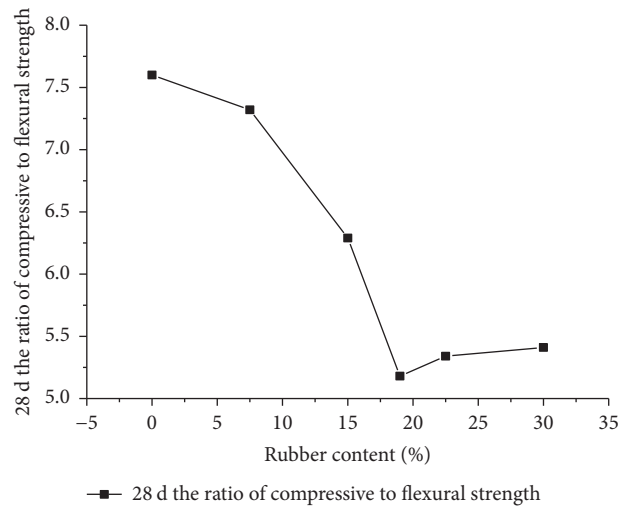


FIGURE 3: 28 d the ratio of compressive to flexural strength with different amount of 60-mesh rubber particles.



FIGURE 4: Mortar mixed with rubber particles compressive failure mode.



FIGURE 5: Reference mortar compressive failure mode.

elastically under external loads, which is not easy to produce brittle failure. It is to improve the impact resistance of mortar which is feasible in the mortar mixed with waste tire rubber particles.

4.2.2. The Dry Shrinking Performance. After the termination of maintenance, the gel pores and capillaries of the internal crumb rubber mortar block lost absorbed water in dry air, producing irreversible drying shrinkage. The drying shrinkage mechanism of cement mortar (concrete) mixed with rubber particles is more complex [18]. There are some main illustrations about it.

(1) *Capillary Tension Theory.* At low temperatures, meniscus is formed when the water surface in capillary declines, forming capillary pressure under tension of water. When the water

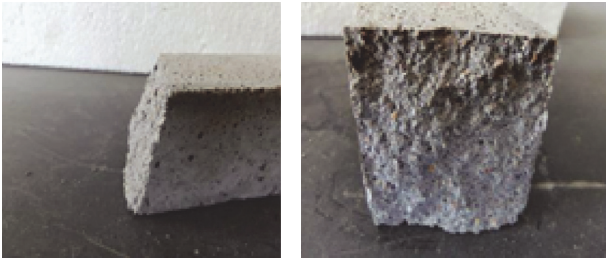


FIGURE 6: Reference mortar flexural failure mode.



FIGURE 7: Mortar mixed with rubber particles flexural failure mode.

inside the capillary evaporates, mortar is in compression state, forming drying shrinkage.

(2) *Disjoining Pressure Theory.* Water absorbs on the surface of C-S-H and produces disjoining pressure at any temperature. If environmental temperature is low and the disjoining pressure is smaller than Van Der Waals force, the micromaterial will aggregate and cause contraction in volume.

Drying shrinkage deformation of cement mortar mixed with different amounts of 60-mesh rubber particles is shown in Figure 9. Drying shrinkage of mortar changed little when the mixing amount of rubber particles is less [19]. The rubber particle is elastomer with small elastic modulus, whose constraint force is relatively small compared with the shrinkage stress of the cement paste [6].

Drying shrinkage of mortar improved significantly with the increment of the mixing amount of rubber particles. Rubber particles are hydrophobic substances, and a layer of water film can easily be formed on the surface of rubber particles when mixed with cement mortar. One part of the surface water is consumed in the course of cement hydration, and the rest free water evaporates in dry environment after maintenance terminated. When the mix amount of rubber particle is increased, the amount of evaporated free water is enlarged accordingly and drying shrinkage became more severer.

5. Conclusions

The surface layer is not a load-bearing part; on the premise of meeting the basic strength requirements, toughness can be considered as the main performance index of mortar. Though rubber particles reduce the compressive strength and the flexural strength of surface mortar, but the ratio of compressive strength to flexural strength is decreased, and

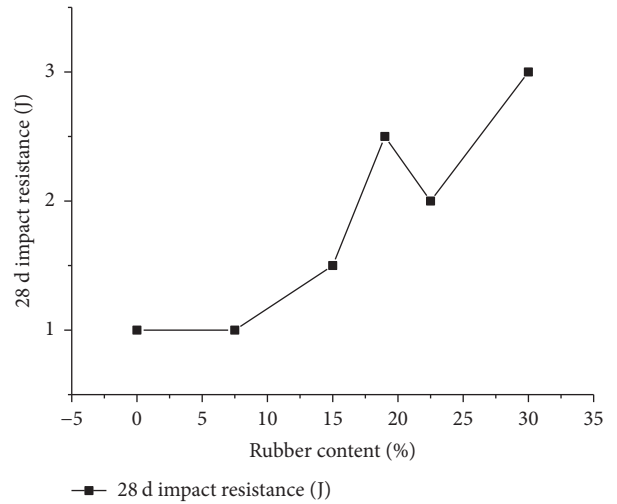


FIGURE 8: 28 d the impact resistance of cement mortar with different amount of 60-mesh rubber particles.

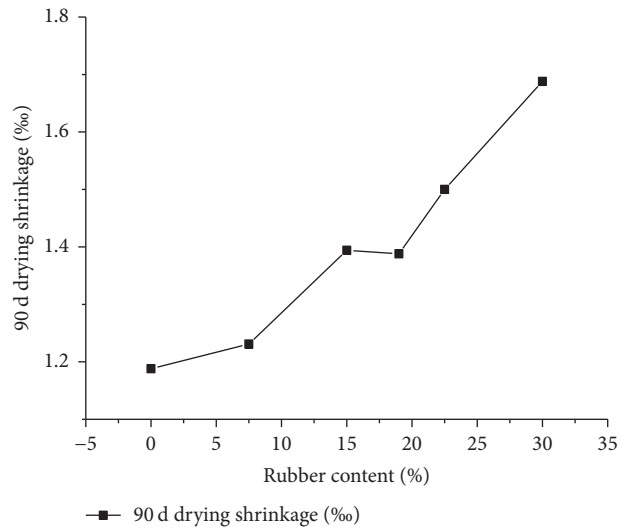


FIGURE 9: 90 d the drying shrinkage of cement with amount of 60-mesh rubber particles mortar.

this indicates the mortar toughness is improved. Cement mortar mixed with crumb rubber can be used for the surface engineering, which may solve the problem that the crack resistance is poor in traditional surface mortar. According to the tests, the ratio of compressive strength to flexural strength is the smallest when the mixing amount of rubber is 19%; meanwhile impact resistance is high at this moment and drying shrinkage is rational, so the appropriate mixing amount of rubber particles determined by this test is 19%.

Competing Interests

The authors (Gang Xue and Mei-ling Cao) declare that there is no conflict of interests regarding the publication of this article.

References

- [1] US Environmental Protection Agency, Scrap tires—basic information, July 2011.
- [2] N. Segre and I. Joekes, “Use of tire rubber particles as addition to cement paste,” *Cement and Concrete Research*, vol. 30, no. 9, pp. 1421–1425, 2000.
- [3] N. Segre, P. J. M. Monteiro, and G. Sposito, “Surface characterization of recycled tire rubber to be used in cement paste matrix,” *Journal of Colloid and Interface Science*, vol. 248, no. 2, pp. 521–523, 2002.
- [4] A. Benazzouk, K. Mezreb, G. Doyen, A. Goullieux, and M. Quéneudec, “Effect of rubber aggregates on the physico-mechanical behaviour of cement-rubber composites-influence of the alveolar texture of rubber aggregates,” *Cement and Concrete Composites*, vol. 25, no. 7, pp. 711–720, 2003.
- [5] K. Sangson, L. Hajirasouliha, and K. Pilakoutas, “Strength and deformability of waste tyre rubber-filled reinforced concrete columns,” *Construction and Building Materials*, vol. 25, no. 1, pp. 218–226, 2011.
- [6] A. Turatsinze, S. Bonnet, and J.-L. Granju, “Potential of rubber aggregates to modify properties of cement based-mortars: improvement in cracking shrinkage resistance,” *Construction and Building Materials*, vol. 21, no. 1, pp. 176–181, 2007.
- [7] B. Huang, X. Shu, and J. Cao, “A two-staged surface treatment to improve properties of rubber modified cement composites,” *Construction and Building Materials*, vol. 40, pp. 270–274, 2013.
- [8] A. Turatsinze, S. Bonnet, and J.-L. Granju, “Mechanical characterisation of cement-based mortar incorporating rubber aggregates from recycled worn tyres,” *Building and Environment*, vol. 40, no. 2, pp. 221–226, 2005.
- [9] Y. Akkaya, C. Ouyang, and S. P. Shah, “Effect of supplementary cementitious materials on shrinkage and crack development in concrete,” *Cement and Concrete Composites*, vol. 29, no. 2, pp. 117–123, 2007.
- [10] A. R. Khaloo, M. Dehestani, and P. Rahmatabadi, “Mechanical properties of concrete containing a high volume of tire-rubber particles,” *Waste Management*, vol. 28, no. 12, pp. 2472–2482, 2008.
- [11] N. Ganesan, J. Bharati Raj, and A. P. Shashikala, “Flexural fatigue behavior of self compacting rubberized concrete,” *Construction and Building Materials*, vol. 44, pp. 7–14, 2013.
- [12] H. Su, J. Yang, T.-C. Ling, G. S. Ghataora, and S. Dirar, “Properties of concrete prepared with waste tyre rubber particles of uniform and varying sizes,” *Journal of Cleaner Production*, vol. 91, pp. 288–296, 2015.
- [13] J. Lv, T. Zhou, Q. Du, and H. Wu, “Effects of rubber particles on mechanical properties of lightweight aggregate concrete,” *Construction and Building Materials*, vol. 91, pp. 145–149, 2015.
- [14] X. Shu and B. Huang, “Recycling of waste tire rubber in asphalt and portland cement concrete: an overview,” *Construction and Building Materials*, vol. 67, pp. 217–224, 2013.
- [15] H. Zhu, N. Thong-On, and X. Zhang, “Adding crumb rubber into exterior wall materials,” *Waste Management and Research*, vol. 20, no. 5, pp. 407–413, 2002.
- [16] J.-H. Xie, Y.-C. Guo, L.-S. Liu, and Z.-H. Xie, “Compressive and flexural behaviours of a new steel-fibre-reinforced recycled aggregate concrete with crumb rubber,” *Construction and Building Materials*, vol. 79, pp. 263–272, 2015.
- [17] D. Sufen and H. Zhide, “Waste tire rubber particles in outer wall external thermal insulation mortar in the heating area in the application,” *Concrete and Cement Products*, no. 5, pp. 48–52, 2011.
- [18] Z. Xiling and Y. Ailing, “Study on mortar elastic modulus of slag cementitious materials,” *Journal of Silicate*, vol. 30, no. 4, pp. 950–954, 2011.
- [19] Y.-M. Zhang, S.-X. Chen, B. Chen, and W. Sun, “Dry shrinkage, frost resistance and permeability of rubber included concrete,” *Key Engineering Materials*, vol. 302-303, pp. 120–124, 2006.